Astronomy Reports, Vol. 46, No. 2, 2002, pp. 110–118. Translated from Astronomicheskiĭ Zhurnal, Vol. 79, No. 2, 2002, pp. 127–136.

Interferometric Observations of 4C 21.53 and PSR 1937+214 at Decameter Wavelengths

A. V. Megn, S. Ya. Braude, S. L. Rashkovskiĭ, N. K. Sharykin, V. A. Shepelev, G. A. Inyutin, R. V. Vashchishin, A. I. Brazhenko, and V. G. Bulatsen

Radio Astronomy Institute, National Academy of Sciences of Ukraine, Kharkov, Ukraine

Received January 25, 2001

Abstract—Preliminary resuts of interferometric observations of 4C 21.53 and PSR 1937+214 at 25 and 20 MHz are presented. The observations were obtained using the URAN-1 and URAN-2 interferometers, with baselines of 42.4 and 152.3 km. In addition to the pulsar radiation, which provides about 70% of the total flux of the object, radio emission from extended components with dimensions of several tens arcseconds has been detected for the first time. The angular size of the pulsar is 3″ at 25 MHz and 4.″8 at 20 MHz. The pulsar's low-frequency spectrum deviates appreciably from the power law derived at higher frequencies. © *2002 MAIK "Nauka/Interperiodica"*.

1. INTRODUCTION

The unusual properties of the radio source 4C 21.53 have attracted the attention of a number of astronomers. This object, which lies close to the Galactic plane ($l = 57.^\circ54$, $b = -0.^\circ28$), displays typical strong scintillation on inhomogeneities in the interplanetary plasma [1]. This indicates that an appreciable fraction of its total flux density is associated with very compact structures.

In 1982, the very rapid pulsar PSR 1937+214 with a period of 1.557 ms [2] was discovered in 4C 21.53, providing the scintillating component. Subsequently, a large number of studies were undertaken [2–10], primarily at centimeter and decimeter wavelengths, and more rarely at meter wavelengths. These observations using radio interferometry, supersynthesis and aperture synthesis techniques, and narrow-beam radio telescopes yielded intensity measurements at various frequencies, the source's radio spectrum, and radio images of 4C 21.53 and other surrounding regions of emission. Much attention has been spent on elucidating the physical nature of the radio source 4C 21.53W, which is located closest to PSR 1937+214, as well as the other components of 4C 21.53W and their possible relation to the pulsar. It became clear that 4C 21.53W consists of three objects: the western component 4C 21.53W; the eastern component 4C 21.53E, separated from 4C 21.53W by approximately 13.′5 in right ascension and 3.′3 in declination; and the pulsar PSR 1937+214, which is located ∼25″ to the west and ∼ 2.′2 to the south of the center of 4C 21.53W. 4C 21.53E is an extragalactic object consisting of two compact features separated by 0.″8 and does not have any physical connection to the pulsar [3]. The physical nature of the western component 4C 21.53W, which resembles an extended radio nebulosity roughly 100″ × 40″ in size at 1.48 GHz [3], and its relationship to the pulsar have been extensively discussed in the literature. It has been suggested that this radio emission might represent a supernova remnant or HII region [2, 3–5, 7, 8].

Indirect evidence in favor of the first (nonthermal) hypothesis is provided by other cases of observed associations between supernova remnants and pulsars, as, for example, in the case of the Crab Nebula, which is associated with a millisecond pulsar—the rapidly rotating neutron star formed during the supernova explosion. However, in contrast to the Crab pulsar and nebula, PSR 1937+214 is located at the southern edge of 4C 21.53W, rather than at the center of the nebulosity; in some radio maps, such as those at 10.7 GHz, the pulsar is even located beyond 4C 21.53W [4]. Of course, this could be due to a southward drift of the pulsar since the explosion, over a time of about 10^5–10^6 yr. In addition, no appreciable linear polarization has been observed, as would be characteristic of the radio emission of a supernova remnant.

Evidence in favor of the second (thermal) hypothesis suggesting that 4C 21.53W is a region of ionized hydrogen is provided by the detection of weak hydrogen recombination lines in this nebula. Unfortunately, the spectral index of this object at centimeter and decimeter wavelengths α ($S \propto \nu^{-\alpha}$, S is the flux

1063-7729/02/4602-0110$22.00

density and ν is the observing frequency) takes on values from 0.26 [3] to 0.03 [4], making it impossible to distinguish between the two hypotheses on this basis, since either an extended supernova remnant or an HII region could have such a spectrum at these frequencies.

Mantovani *et al.* [4] even suggested that the southern part of 4C 21.53W is a plerion supernova remnant supplied by PSR 1937+214, while the northern part is an HII region. Decisive evidence supporting one or the other of these hypotheses could be obtained from spectral measurements at very high frequencies, in the infrared, where the intensity of a supernova should be much weaker than that of an HII region [4]. The infrared measurements of [10] showed the presence of intense emission in this region, providing some confirmation of the thermal nature of 4C 21.53W. The distance to the HII region in this case is estimated to be about 10.7 kpc, while the distance to PSR 1937+214 is about 5 kpc [5, 7].

Nevertheless, the possible presence of a supernova remnant in the region of the pulsar cannot be completely excluded: Sieber and Seiradakis [5] detected a weak plateau of emission 19′ in radius at $\lambda = 11$ cm and 16′ in radius at $\lambda = 6$ cm around PSR 1937+214 and 4C 21.53W. Some regions of this emission are linearly polarized up to 50%, and its spectral index is 0.45. In addition, a linear polarization of 10% was detected in the southern part of the nebulosity [4]. Thus, we cannot rule out the presence of a weak supernova remnant around PSR 1937+214, whose radiation has been below the sensitivities of most observations.

In this connection, it is of considerable interest to obtain new interferometric observations of PSR 1937+214 and 4C 21.53 at decameter wavelengths. Earlier observations in this range using the UTR-2 radio telescope yielded the spectrum of 4C 21.53 from 10 to 25 MHz [11] and the source's radio structure at 20 and 25 MHz, based on interplanetary-scintillation measurements [12]. After these earlier observations, it remained to elucidate whether all the radiation detected in [11] was from the pulsar, or whether there was a significant contribution from other regions. In addition, it is of interest to more accurately determine the angular size of PSR 1937+214 at decameter wavelengths. The current paper addresses these questions.

2. INSTRUMENTS, MEASUREMENT TECHNIQUE, AND DATA REDUCTION

The first interferometric observations of 4C 21.53 and PSR 1937+214 at decameter wavelengths were carried out on the URAN-1 and URAN-2 interferometers, which are oriented nearly east–west and have baselines of $D = 42.3$ km and 152.3 km. Interference fringes were formed by multiplying the signals of the north–south antenna of the UTR-2 radio telescope [13] and the URAN-1 and URAN-2 antennas [14, 15]. The observing method, described in [16], enabled us to take into account the effect of Faraday rotation, which is very important at these wavelengths.

The spatial frequencies of the radio-brightness distributions of 4C 21.53W and PSR 1937+214 in the U–V plane measured by the URAN interferometers are given by the expressions

$$U_1 = \frac{42276.7}{\lambda}\cos(T_0 - 2\overset{\circ}{.}2), \qquad (1)$$
$$V_1 = \frac{15494.5}{\lambda}\sin(T_0 - 2\overset{\circ}{.}2) - \frac{1305.8}{\lambda}$$

for URAN-1 and

$$U_2 = \frac{152292.6}{\lambda}\cos(T_0 + 0\overset{\circ}{.}38), \qquad (2)$$
$$V_2 = \frac{55815.4}{\lambda}\sin(T_0 + 0\overset{\circ}{.}38) + \frac{800.2}{\lambda}$$

for URAN-2. Here, T_0 is the hour angle relative to the culmination time in degrees and λ is the wavelength in meters.

The observations were conducted simultaneously at 25 and 20 MHz during nighttime and morning in the period from April 17–26, 1999. Since it is not possible to measure the phase of the visibility function at these frequencies using the URAN interferometers, we determined only the amplitude of the observed visibility function γ_o for hour angles from -160^m to $+120^m$. The method used to record and reduce the data is described in [17].

The absence of phase information and insufficient coverage of the U–V plane prevented the use of standard image-reconstruction methods. Therefore, we derived the parameters of model radio-brightness distributions for sets of components with Gaussian flux-density distributions[1] for which the calculated visibility function $\gamma_c(T_0)$ was in best agreement with the observed visibility function $\hat{\gamma}_o(T_0)$. The quantity $\gamma_c(T_0)$ was determined by the relation

$$\gamma_c(T_0) = \left|\sum_1^n \frac{S_i}{S_0}\gamma_i(T_0)e^{i\varphi_i(T_0)}\right|, \qquad (3)$$

where

$$\gamma_i(T_0) = \exp\left\{-[1.88U_j\,(T_0)\,\Delta\theta_{\alpha_i}]^2\right\} \qquad (4)$$
$$\times \exp\left\{-[1.88V_j(T_0)\Delta\theta_{\delta_i}]^2\right\}$$

and

$$\varphi_i(T_0) = \frac{2\pi D_j}{\lambda}\,[\Delta\alpha_i\cos(T_0) \qquad (5)$$

[1] Here, we present the angular sizes of Gaussian radio components at the half-maximum level.

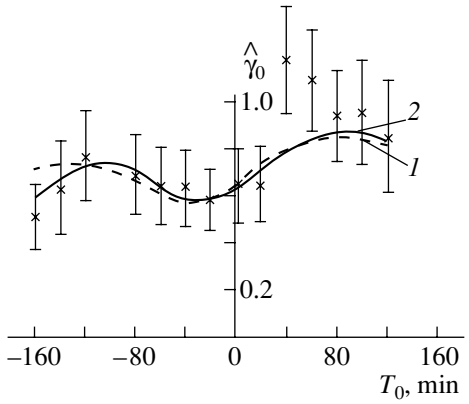

Fig. 1. Measurements of the amplitude of the visibility function $\hat{\gamma}_0$ of 4C 21.53 and PSR 1937+214 for various hour angles T_0 at 25 MHz using the URAN-1 interferometer. The x's with bars show the mean-weighted observed values with their rms deviations $\pm\sigma_\gamma$. The dashed curve *1* shows the calculated dependence $\gamma_c(T_0)$ for the best-fit two-component model. The solid curve *2* shows the calculated dependence $\gamma_c(T_0)$ for the best-fit three-component model.

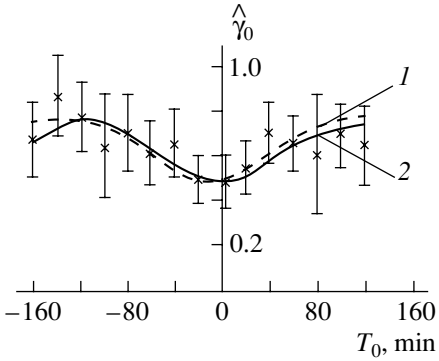

Fig. 2. Same as Fig. 1 for 20 MHz.

$$+ \Delta\delta_i \sin(\delta_0)\sin(T_0)]\,.$$

Here, $\varphi_i(T_0)$ is the phase of the visibility function corresponding to component i relative to component *1*; $\gamma_i(T_0)$ is the amplitude of this visibility function; n is the number of components in the model radio-brightness distribution; δ_0 is the mean declination of this distribution; $\Delta\alpha_i = \alpha_i - \alpha_1$, $\Delta\delta_i = \delta_i - \delta_1$, α_i, δ_i, $\Delta\theta_{\alpha_i}$, $\Delta\theta_{\delta_i}$, and S_i are the right ascension, declination, angular dimensions, and flux density of model component i; $S_0 = \Sigma S_i$; and $U_j(T_0)$ and $V_j(T_0)$ are the spatial frequencies of the jth URAN-1 and URAN-2 interferometers ($j = 1, 2$), given by (1) and (2).

We used a χ^2 criterion as a measure of the agreement between the calculated model and observed visibility functions [18]:

$$\chi^2 = \sum_{i=1}^{N} \frac{[\hat{\gamma}_{oi}(T_0) - \gamma_{ci}(T_0)]^2}{\sigma^2_{\gamma_i}(T_0)}, \qquad (6)$$

where N is the number of independent measurements of the mean-weighted amplitude of the visibility function $\hat{\gamma}_{oi}$ at various hour angles. We took the best model to be that corresponding to the minimum $\chi^2_{\min}$ for which there was a sufficiently high probability of exceeding this value $W_k(\chi^2 > \chi^2_{\min})$, where

$$k = N - 1 - p. \qquad (7)$$

Here, k is the number of degrees of freedom for the given model and p is the number of parameters determined by the model radio-brightness distribution.

3. RESULTS

Figures 1 and 2 show the results of our URAN-1 observations in the form of the mean-weighted values of the observed visibility function $\hat{\gamma}_0$ at various hour angles T_0 at 25 MHz (Fig. 1) and 20 MHz (Fig. 2). The analogous data for the URAN-2 observations are presented in Fig. 3, for both 25 MHz ($\times$) and 20 MHz ($\circ$). The vertical lines show the rms deviations, taking into account both the random scatter in the measurements and systematic errors.

According to the results of [3], 4C 21.53E and 4C 21.53W should not be detected at decameter wavelengths, since their flux densities are below the sensitivity of our instruments, and we should have recorded emission only from PSR 1937+214. However, we can see in Figs. 1–3 that our measurements are inconsistent with the detection of a single compact or extended component. In the case of a single compact component, such as the pulsar, the URAN-1 measurements of the visibility function would have been nearly equal to unity and would not have shown oscillations in the hour-angle dependence $\hat{\gamma}_0(T_0)$. We would likewise not obtain the observed dependence $\hat{\gamma}_0(T_0)$ in the case of a single extended component; in addition, the URAN-2 signal would have been appreciably weaker than the URAN-2 signal in this case, which was not observed.

The oscillations in $\hat{\gamma}_0(T_0)$ for the URAN-1 observations testify that the interferometer is detecting the contributions of two or more components. At the same time, there is essentially no hour-angle dependence $\hat{\gamma}_0(T_0)$ for either frequency in Fig. 3, suggesting that the expended components are nearly completely resolved out so that essentially only the single compact component is detected.

For this reason, we first considered a simple two-component model. The dashed curves in Figs. 1 and 2 show the calculated dependences $\hat{\gamma}_c(T_0)$ for

Table 1. Parameters of the best-fit two-component model for 4C 21.53 and PSR 1937+214

Component	$\Delta\alpha_i$	$\Delta\delta_i$	$\Delta\theta_{\alpha_i}$	$\Delta\theta_{\delta_i}$	S_i/S_0
Compact	0″	0″	$3'' \pm 0.6''$	$3'' \pm 0.6''$	0.704 ± 0.02
			(5 ± 0.8)	(5 ± 0.8)	0.704 ± 0.02
Extended	40 ± 2	137 ± 19	21 ± 3	170 ± 26	0.296 ± 0.02

Note: The values in parantheses correspond to 20 MHz.

Table 2. Parameters of the best-fit three-component model for 4C 21.53 and PSR 1937+214

Component	$\Delta\alpha_i$	$\Delta\delta_i$	$\Delta\theta_{\alpha_i}$	$\Delta\theta_{\delta_i}$	S_i/S_0
Compact	0″	0″	$3'' \pm 0.8''$	$3'' \pm 0.8''$	0.704 ± 0.08
			(4.8 ± 1)	(4.8 ± 1)	
First extended	35 ± 2	185 ± 14	20 ± 3	20 ± 3	0.183 ± 0.04
Second extended	45 ± 5	40 ± 19	14 ± 6	14 ± 6	0.113 ± 0.04

Note: The values in parantheses correspond to 20 MHz.

Table 3. Flux density from 4C 21.53 and PSR 1937+214 and from individual components for the two best-fit models

Frequency, MHz	S_0, Jy	Two-component model		Three-component model		
		compact component	extended component	compact component	first extended component	second extended component
		S, Jy				
20	225 ± 29	158 ± 21	67 ± 10	158 ± 27	41 ± 10	26 ± 10
25	172 ± 23	121 ± 16	51 ± 7.5	121 ± 21	32 ± 8	19 ± 7

the best-fit model consisting of one compact and one extended component, determined from the χ^2 criterion. We searched for the best-fit model jointly taking into account the data for the two interferometers at the two frequencies, assuming that the coordinates of all component centers, the dimensions of extended components, and the component flux ratios were the same at the two frequencies. Table 1 presents the parameters for the corresponding model radio-brightness distribution and their errors. Note that, in this case, the ratio $\gamma_{\max}/\gamma_{\min} = 1.52$ and 1.57 at 25 and 20 MHz, respectively.

It follows that, apart from individual measurements at 25 MHz at $T_0 = 40$ and 60 min, which have large errors, even the simple two-component model $\gamma_c(T_0)$ agrees with the observations reasonably well. This is reflected by the comparatively small value of $\chi^2_{\min}$ for these dependences at the two frequencies. For both interferometers at both 20 and 25 MHz, $\chi^2_{\min}$ is between two and five, with the probability of exceeding these values usually being no lower than 0.7. The lowest probability for exceeding $\chi^2_{\min}$, equal to 0.63, is obtained at 25 MHz for the URAN-1 interferometer, where the measurements have the lowest accuracy.

In the two-component model, URAN-2 can detect only the compact component, since the extended component is completely resolved if it has the dimensions indicated in Table 1. The flux density from this extended component received by the URAN-2 interferometer is $\gamma_{e2}S_e$, which, according to (2) and (4), is 0.13 Jy at 25 MHz and 1.5 Jy at 20 MHz, while the sensitivity of the instrument (for a signal-to-noise ratio of unity) is about 10 Jy. Therefore, the ratio $\gamma_{\max}/\gamma_{\min}$ in Fig. 3 is essentially equal to unity.

Thus, the decameter flux density of 4C 21.53 is contributed by at least two components: 70% is from a compact and 30% from an extended component. Table 1 shows that the center of the extended component is displaced from the center of the compact component by 142.″7 in position angle 16.°3, in reasonable agreement with the relative separation of the centers of PSR 1937+214 and 4C 21.53W presented in [5], 134.″4 in position angle 10.°8. In addition, the compact component is partially resolved

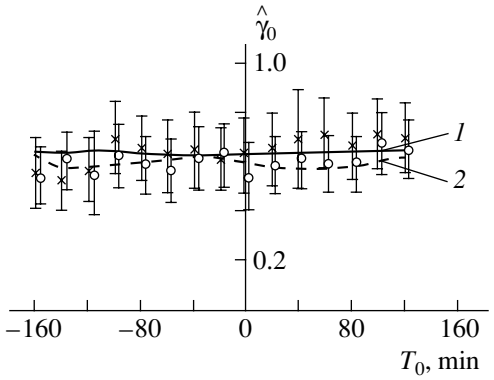

Fig. 3. Measurements of the amplitude of the visibility function $\hat{\gamma}_0$ of 4C 21.53 and PSR 1937+214 for various hour angles T_0 at 25 MHz and 20 MHz using the URAN-2 interferometer. The x's and circles with bars show the mean-weighted observed values with their rms deviations $\pm\sigma_\gamma$. The solid curve *1* shows the calculated dependence $\gamma_c(T_0)$ for the best-fit three-component model at 25 MHz. The dashed curve *2* shows the same calculated dependence for 20 MHz.

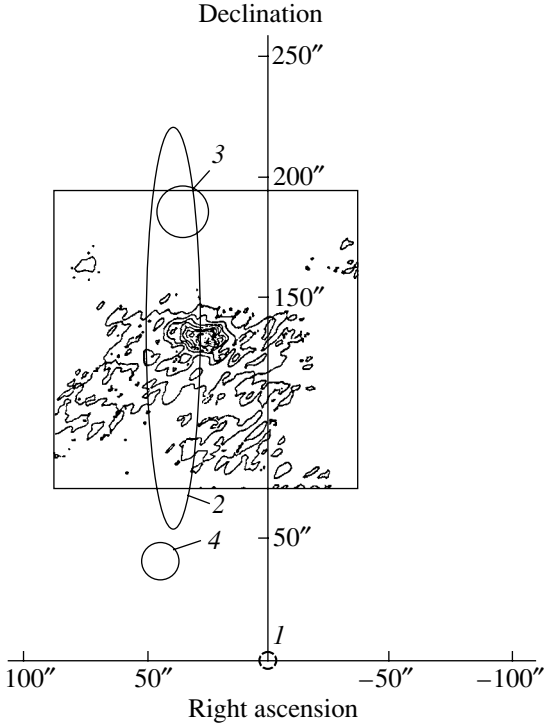

Fig. 4. Model radio-brightness distribution for 4C 21.53 and PSR 1937+214 superposed on a radio image of the HII region 4C 21.53W obtained using the VLA at 1480 MHz. *1* shows pulsar PSR 1937+214 at 25 and 20 MHz; *2*, the extended component in the two-component model; and *3* and *4*, the two extended components in the three-component model.

by URAN-2, indicating its angular size is 3″ at 25 MHz and 5″ at 20 NHz. We will show below that these sizes of the compact component at decameter wavelengths are in good agreement with the measured angular size of PSR 1937+214 at higher frequencies [9]. This suggests that our compact component of 4C 21.53 corresponds to the pulsar PSR 1937+214, while the extended component is associated with 4C 21.53W. However, the size of the extended component does not agree exactly with the size of 4C 21.53W presented in [3] derived from VLA observations at 1480 MHz, which indicate this component to have dimensions of roughly 100″ × 40″ in right ascension and declination, respectively.

Although the $\chi^2_{\min}$ values for the two-component model for the radio-brightness distribution are fairly small when the probability of exceeding them is high, the very large extent of the extended component in declination appears somewhat doubtful from a physical point of view and suggests the presence of several somewhat smaller extended components spread out in declination. For this reason, we derived another optimal (based on the χ^2 criterion) three-component model for the radio-brightness distribution, consisting of one compact and two extended components. The calculated dependences $\gamma_c(T_0)$ for this best-fit model are presented in Figs. 1 and 2 by the solid curves *2*, and the corresponding model parameters are given in Table 2.

Table 3 presents the total flux density S_0 from 4C 21.53 and PSR 1937+214 together with the flux densities of the individual components in the two models.

The dependences $\gamma_c(T_0)$ for URAN-1 for the three-component model are fairly similar to those for the two-component model. In particular, the ratios $\gamma_{max}/\gamma_{min}$ at 25 and 20 MHz are virtually the same for the interferometer URAN-1 for the three-component and two-component models. For both interferometers at both frequencies, the value of $\chi^2_{\min}$ is slightly lower for the three-component model (1.5 compared to 3.0); however the probability of exceeding these values remains essentially unchanged due to the larger number of parameters for the three-component model. For this reason, and also due to the comparatively large scatter of the data in Figs. 1–3, it was not meaningful to try to find solutions for more complex model radio-brightness distributions. This could be attempted if we had substantially more accurate measurements, increasing the χ^2 values for the two-component and three-component models; we could then determine the parameters of these models more accurately by re-minimizing χ^2 and possibly investigate more complex models as well.

Tables 1 and 2 show that the relative flux densities and angular sizes of the compact components in the two models are nearly the same. Only the dimensions

Table 4. Measurements of scintillation of 4C 21.53 at decameter wavelengths

Frequency, MHz	S_0, Jy	$\Delta\theta_e$, arcsec	S_e/S_0
20	250 ± 50	$2.0^{+0.7}_{-1.2}$	0.85 ± 0.15
25	160 ± 25	$1.5^{+0.5}_{-1.0}$	$0.93^{+0.07}_{-0.2}$

of the extended component have changed appreciably. The single component very elongated in declination has been replaced by two comparatively small extended components widely separated in declination and with approximately the same right ascensions. The first, stronger, extended component is at the northern end and the second at the southern edge of the extended component for the two-component model. Figure 4 shows schematics of the models whose parameters are presented in Tables 1 and 2 superposed on a radio image of 4C 21.53W obtained from VLA observations at 1480 MHz [3]. Here, *1* is pulsar PSR 1937+214, *2* the extended component from Table 1, and *3* and *4* the extended components from Table 2. The northern component from Table 2 is near the center of 4C 21.53W, while the southern component is near the pulsar. We suggest that this model corresponds better with our physical understanding of the structure of 4C 21.53W at decameter wavelengths.

The calculated dependences $\gamma_c(T_0)$ for the three-component model for URAN-2 are presented in Fig. 3 by the solid (25 MHz) and dashed (20 MHz) curves. In contrast to the analogous dependences for the two-component model, where $\gamma_c(T_0)$ is essentially constant, the three-component model gives rise to slight variations in γ_c with T_0, associated with the incomplete resolution of the second extended component by the URAN-2 interferometer. At 25 and 20 MHz, $\gamma_{max}/\gamma_{min} = 1.05$ and 1.07, respectively. The URAN-2 correlated flux densities at 25 and 20 MHz from the first extended component are 0.15 and 1.43 Jy and from the second extended component are 1.41 and 4.75 Jy—no more than 1% and 3% of the flux densities of the pulsar at 25 and 20 MHz.

It is of interest to compare these new data with the results of earlier estimates of the characteristics of the pulsar derived from interplanetary-scintillation measurements, presented in Table 4 [12]. The data in this table show a large amount of scatter, due to the known limitations of scintillation measurements. Nevertheless, our interferometric measurements of the pulsar dimensions are, on average, a factor of 2–2.5 higher than the values in Table 4, while the relative flux is lower, especially at 25 MHz.

4. SPECTRAL MEASUREMENTS

The radio-brightness distribution is related to the spectral characteristics of the emission $S(\nu)$. Figure 5 shows the radio spectrum of 4C 21.53W and PSR 1937+214. The circles and triangles show measurements of $S(\nu)$ for 4C 21.53W from 24 500 MHz to 408 MHz and for PSR 1937+214 from 1415 MHz to 25.6 MHz taken from [3, 5, 6]. At low frequencies ($\nu \leq 25$ MHz), the x's show the data of [11], and the diamonds show our 25 and 20 MHz measurements from the current paper. Figure 5 shows that the spectrum of 4C 21.53W is nearly flat from 5000 to 608.5 MHz, with only a slight increase in $S(\nu)$ with decreasing frequency (curve *1* with $\alpha_1 \approx 0.04$). At higher frequencies, $S(\nu)$ falls rapidly with increasing frequency, but, at the lowest frequencies at which measurements of 4C 21.53W have been made, 430 and 408 MHz, we can already note a significant growth in the flux density with decreasing frequency, with the spectral index becoming appreciably greater than 0.04.

The spectrum of the pulsar (curve *2*) is a power law with spectral index $\alpha_2 \approx 2.44$ at $\nu > 73.8$ MHz and $\alpha_3 \approx 1.74$ at lower frequencies; the total spectrum for the object is presented for frequencies below 73.8 MHz. In Fig. 5, the squares show the interferometric measurements of the flux density of the pulsar, and the circled x's, the flux densities for the two extended components in the three-component model based on our URAN observations. If we connect the data for the extended components with the lowest-frequency measurements of 4C 21.53W by power-law dependences (dot–dashed lines *4*, *5*), the spectral index for the first (northern) component is $\alpha_4 \approx 1.08$, while that for the second (southern) component is $\alpha_5 \approx 0.95$. In the two-component model, assuming the single extended component should be identified with 4C 21.53W yields a spectral index of 1.24.

As noted earlier in [11], the spectrum of the total radio emission at frequencies $\nu < 50$ MHz is a power law (linear in $\log S$–$\log \nu$ coordinates). However, taking into account only the radio emission of PSR 1937+214 at decameter wavelengths, strictly speaking, we already observe a curved spectrum, representing a slower growth in the flux density with decreasing frequency. An approximate spectrum for the pulsar at $\nu < 73.8$ MHz is given by the dashed line *3*. Radio interferometric observations with corresponding resolution at 25 MHz $< \nu <$ 73.8 MHz are needed to more accurately determine the spectrum of the pulsar.

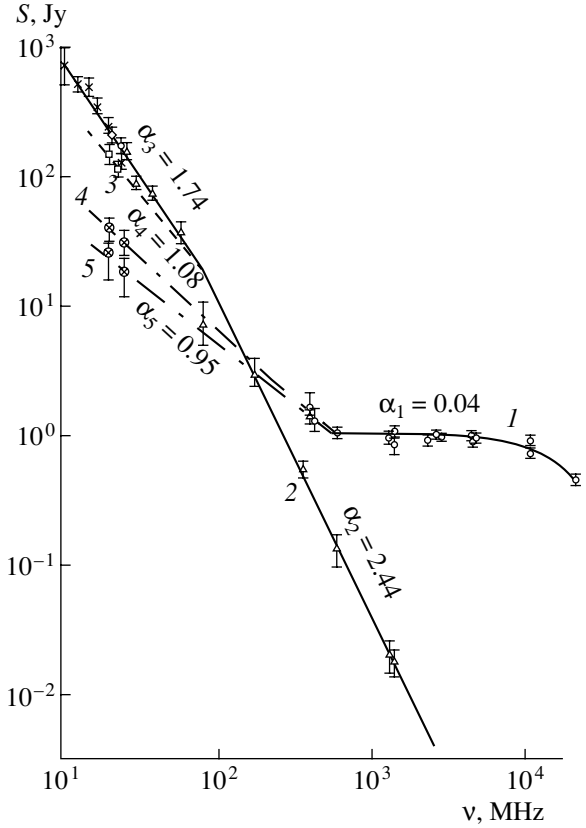

Fig. 5. Spectrum of 4C 21.53W and PSR 1937+214 from 10 to 2450 MHz. The circles show data from [5]; the triangles, data from [3, 5, 6]; the x's, data from [11]; the diamonds and squares, data from the current study for the total flux density and the flux density of PSR 1937+214, respectively; and the circled x's, the flux densities for the extended components for the three-component model for the radio-brightness distribution. The solid curve *1* is the spectrum of 4C 21.53W; the solid curve *2*, the spectrum of PSR 1937+214 at $\nu > 73.8$ MHz; and the total spectrum of the radio source at $\nu < 73.8$ MHz; the dashed curve *3*, the expected spectrum of the pulsar at low frequencies; and the dashed curves *4* and *5*, the inferred spectra of the extended components for our three-component model for the radio-brightness distribution.

5. CONCLUSION

The main conclusion that can be drawn based on our analysis of these new measurements is that, in contrast to earlier suggestions that all observed radiation at decameter wavelengths was due to the pulsar [3, 6, 11], in fact, the decameter emission of 4C 21.53 includes contributions from both the pulsar PSR 1937+214 (which provides about 70% of the total flux density) and one or more extended components located near 4C 21.53W and the pulsar. This is probably the case at meter wavelengths as well ($\nu <$ 100 MHz), where the pulsar emission is received as a continuous signal, since Fig. 5 (lines *4*, *5*) shows that the expected emission of the extended components at these frequencies is sufficient for their detection.

The second important result of this work is our measurement of the angular dimensions of PSR 1937+214. For our most trustworthy, three-component model for the radio-brightness distribution of 4C 21.53, the pulsar's size is 3″ at 25 MHz and 4″.8 at 20 MHz. The angular size of the pulsar presented in [9] was 15 milliarcseconds at 326 MHz. A power-law frequency dependence is usually expected for the angular size of a very compact source such as a pulsar, due to scattering of the radiation in the interstellar and interplanetary plasma: $\Delta\theta \sim \nu^{-\zeta}$. Data obtained at 326 and 25 MHz, and also at 326 and 20 MHz, indicate that the spectral index is equal to $\zeta = 2.06$. Based on our measurements of $\Delta\theta$ at 25 and 20 MHz, $\zeta = 2.1$; however this value is very uncertain due to the relatively small frequency difference.

According to [9], the values of ζ for a number of pulsars fall in the range $2 < \zeta < 2.18$, in good agrement with our data. This provides further confirmation that the compact object in the radio source 4C 21.53 is, indeed, the pulsar PSR 1937+214[2].

We cannot draw such firm conclusions about the nature of the extended components providing about 30% of the total emission at 25 and 20 MHz, since our models with one and two extended components are virtually indistinguishable from the point of view of a statistical χ^2 criterion. Note that extrapolating the emission of all radio sources observed near PSR 1937+214 at shorter radio wavelengths to decameter wavelengths assuming their spectral indices α to be constant does not yield the flux density in Table 3. For example, the extrapolated flux density of the nearest source 4C 21.53E at frequencies $\nu < 30$ MHz is < 2–3 Jy, with its intensity falling with further decrease in frequency [3]. The remaining sources near the pulsar have very small flux densities at shorter radio wavelengths and modest spectral indices so that there is no reason to expect their intensities at decameter wavelengths to be as large as several tens of Jy [5, 7].

It is possible that the extended regions providing 30% of the total flux density at decameter wavelengths are not associated with the radio sources surrounding 4C 21.53W observed at frequencies $\nu >$ 365 MHz. In this connection, we will briefly consider various possible explanations for the physical nature

[2]Note that, in the case of pulsar sizes derived from scintillation measurements [12], comparison with measurements at 326 MHz yield $\zeta = 1.75$ and 1.79 for 20 and 25 MHz, respectively.

of the extended components detected at decameter wavelengths.

First, we cannot completely rule out the possibility that these regions of emission are associated with 4C 21.53W. In our two-component model, the extended component coincides with an appreciable part of 4C 21.53W, and the two extended components in our three-component model are located in the immediate vicinity of 4C 21.53W. Furthermore, as noted above, the coordinates of the extended component in the former model relative to PSR 1937+214 are in good agreement with data obtained at higher radio frequencies. Further evidence supporting this identification is provided by the spectral dependences *4* and *5* for the extended components from 20 to 430 MHz in Fig. 5, which indicate spectral indices close to unity, together with the substantial increase in the spectral index of 4C 21.53W from 0.04 to $\simeq 1$ at frequencies $\nu < 608.5$ MHz [5].

A second possibiliity is that the radio emission of the extended components is associated with the large, weak halo of emission around the pulsar with a radius of about 19′ detected at 2700 MHz using the 100-m Effelsberg telescope [5], which may be the sought-for supernova remnant associated with PSR 1937+214. In this case, we expect the spectral indices of these components to be somewhat smaller than in the first hypothesis. The flux density of this halo at 2700 MHz is about 0.6 Jy; assuming its emission to be synchrotron radiation and calculating a power-law spectral index based on this measurement and our own lower-frequency measurements yields $\alpha \approx 0.95$ for our two-component model and $\alpha \approx 0.85$ for the first (northern) component and $\alpha \approx 0.75$ for the second (southern) component in our three-component model. In both cases, the decrease in the flux density of the extended components with increasing frequency is not so rapid that we would not be able to detect their emission at meter wavelengths, at least at relatively long meter wavelengths (Fig. 5, dependences *4*, *5*).

If the emission of the extended component(s) is not associated with 4C 21.53W or a halo surrounding PSR 1937+214 that has not yet been detected at meter or shorter radio wavelengths, this implies that its emission must have a rather steep spectral index. If the sensitivity of the observations of 4C 21.53W at 1480 MHz [3] was one to two orders of magnitude below the received flux density (about 1 Jy), the spectral index of the extended component(s) must no smaller than 1.5–2. Naturally, the probability of detecting this emission at meter and shorter radio wavelengths is substantially lower than in the previous cases. However, in spite of this large inferred spectral index, we cannot consider this possibility to be unlikely, since intense, steep-spectrum extended components surrounding a number of quasars and radio galaxies have already been detected at decameter wavelengths. For example, a halo with a size $\Delta\theta = 45''$ and spectal index $\alpha = 1.56$ [19] was detected around the quasar 3C 154; a halo with $\Delta\theta = 25''$ and $\alpha = 1.4$, around the quasar 3C 196 [20]; a halo with $\Delta\theta = 20''$ and $\alpha = 1.1$, around the quasar 3C 254 [21]; and a halo with $< 60''$ and $\alpha \approx 1.1$, around the radio galaxy Perseus A (3C 84A) [22].

Finally, another possible explanation for the extended component(s) detected near PSR 1937+214 at decameter wavelengths is that this object is located quite near the Galactic plane. If there are appreciable irregularities in the distribution of the radio emission of the Galactic background, these could in principle be detected by radio interferometers. Our estimates for URAN-1 indicate that the detection of the extended components would require a jump in the temperature of the Galactic radio background by thousands of Kelvin over an area of no more than several arcminutes. Observations at decameter and meter wavelengths (see, for example, [23–26]) do not show any such jumps in temperature in the region near 4C 21.53W and PSR 1937+214. Of course, these observations had rather poor angular resolution, with a $0.^\circ5 \times 21^\circ$ beam at 12.6 to 25 MHz [23], a $16.^\circ5 \times 16.^\circ5$ beam at 10 MHz [24], and a $7.^\circ5$ beam at 38 MHz [25]. Similar oservations have been carried out with higher resolution only at relatively short meter wavelengths and at higher frequencies, with resolution 20′ at 178 MHz [26] and 16′ at 610.5 MHz [27].

A conclusive test of this last possibility requires measurements of the Galactic background at decameter and long meter wavelengths with a narrow beam in both dimensions, with resolution better than several arcminutes. However, no instruments capable of providing such measurements are currently available. Therefore, more accurate estimation of the coordinates and dimensions of the regions of emission responsible for the extended components detected at decameter wavelengths and determination of their physical nature requires interferometric observations with corresponding resolution at meter wavelengths, as well as more accurate interferometric measurements at decameter wavelengths. Such observations may become possible during solar-activity minimum.

6. ACKNOWLEDGMENTS

This work was supported by grants INTAS 97-1964 and INTAS CNES-1450.

REFERENCES

1. J. J. Rickard and W. M. Cronyn, Astrophys. J. **228**, 755 (1979).
2. D. C. Backer, S. R. Kulkarni, C. Heiles, *et al.*, Nature **300**, 615 (1982).
3. W. C. Erickson, Astrophys. J. Lett. **264**, L13 (1983).
4. F. Mantovani, N. Panaqia, and P. Tomasi, Astron. Astrophys. **123**, 347 (1983).
5. W. Sieber and J. H. Seiradakis, Astron. Astrophys. **130**, 257 (1984).
6. W. C. Erickson and M. J. Mahoney, Astrophys. J. Lett. **299**, L29 (1985).
7. J. L. Caswell and T. L. Landecker, Astron. J. **90**, 488 (1985).
8. N. Duric and P. C. Greqory, Astron. J. **95**, 1149 (1988).
9. C. R. Gwinn, N. Bartel, and J. M. Cordes, Astrophys. J. **410**, 673 (1993).
10. A. J. Norton, M. J. Coe, S. J. Unqer, *et al.*, Mon. Not. R. Astron. Soc. **260**, 883 (1993).
11. S. Ya. Braude, S. M. Zakharenko, and K. P. Sokolov, Astron. Zh. **62**, 34 (1985) [Sov. Astron. **29**, 20 (1985)].
12. V. P. Bovkun and I. N. Zhuk, Astron. Zh. **61**, 1108 (1984) [Sov. Astron. **28**, 648 (1984)].
13. A. V. Megn, L. G. Sodin, N. K. Sharykin, *et al.*, in *Antennas,* Ed. by A. A. Pistol'kors (Svyaz', Moscow, 1978), No. 26, p. 15.
14. A. V. Megn, S. Ya. Braude, S. L. Rashkovsky, *et al.*, Turk. J. Phys. **18** (9), 813 (1994).
15. A. V. Megn, S. Ya. Braude, S. L. Rashkovskiĭ, *et al.*, Radiofiz. Radioastron. **2** (4), 385 (1997).
16. V. P. Bovkun and A. V. Megn, Izv. Vyssh. Uchebn. Zaved., Radiofiz. **26** (11), 1357 (1983).
17. A. V. Megn, S. Ya. Braude, S. L. Rashkovskiĭ, *et al.*, Astron. Zh. **78** (2), 106 (2001) [Astron. Rep. **45**, 86 (2001)].
18. D. Himmelblau, *Process Analysis by Statistical Methods* (McGraw-Hill, New York, 1970; Mir, Moscow, 1973), p. 957.
19. A. V. Megn, S. Ya. Braude, S. L. Rashkovskiĭ, *et al.*, Astron. Zh. **75**, 818 (1998) [Astron. Rep. **42**, 722 (1998)].
20. A. V. Megn, S. Ya. Braude, S. L. Rashkovskiĭ, *et al.*, Pis'ma Astron. Zh. **22**, 428 (1996) [Astron. Lett. **22**, 385 (1996)].
21. A. V. Megn, S. Ya. Braude, S. L. Rashkovskiĭ, *et al.*, Kinematika Fiz. Nebesnykh Tel **12** (6), 3 (1996).
22. A. V. Megn, S. Ya. Braude, S. L. Rashkovski, *et al.*, Astrophys. Space Sci. **102**, 155 (1984).
23. I. N. Zhuk, Izv. Vyssh. Uchebn. Zaved., Radiofiz. **16** (5), 754 (1973).
24. A. V. Antonov, Izv. Vyssh. Uchebn. Zaved., Radiofiz. **16** (5), 759 (1973).
25. J. Milogradov-Turin and F. G. Smith, Mon. Not. R. Astron. Soc. **161**, 269 (1973).
26. J. L. Caswell, J. H. Crowther, and D. J. Holden, Mem. R. Astron. Soc. **72**, 1 (1967).
27. H. Wendker, Astron. J. **73** (7), 644 (1968).

Translated by D. Gabuzda

Astronomy Reports, Vol. 46, No. 2, 2002, pp. 119–126. Translated from Astronomicheskiĭ Zhurnal, Vol. 79, No. 2, 2002, pp. 137–144.

The Third Body in the Eclipsing System RR Lyn

Kh. F. Khaliullin and A. I. Khaliullina

Sternberg Astronomical Institute, Universitetskiĭ pr. 13, Moscow, 119899 Russia

Received June 21, 2001

Abstract—Based on 70 years of published photoelectric observations, we have detected quasi-periodic cophased oscillations of the times of the primary and secondary minima of RR Lyn, one of the brightest and nearest eclipsing binaries in the northern sky ($V = 5^m.54$; $r = 74$ pc). Approximating these oscillations using the light equation yields estimates of the orbital parameters of the third body in the system and imposes constraints on its mass, M_3. In the most probable case when the orbits of the eclipsing and triple systems are coplanar, $M_3 = 0.10 \pm 0.02 M_\odot$, and the semimajor axis of the orbit $A_3 = 17.4 \pm 3.5$ AU, with a substantial eccentricity, $e_3 = 0.96 \pm 0.02$. We have carried out a detailed study of the apsidal rotation of this eclipsing and now multiple system, which was suggested by Koch as a test of general relativity as far back as 1973. Our high-precision $WBVR$ photoelectric photometry ($\sigma_{\rm obs} \cong 0^m.0032$) has removed some contradictions. At the same time, the proximity of the longitude of periastron ω to 180°; the close correlation between the jointly estimated values of ω, e and the limb-darkening coefficients for the component disks, u_1 and u_2; and microfluctuations in the brightnesses of the stars prevent determination of the rate of rotation of the elliptical orbit in the system, even using the most accurate measurements.

1. INTRODUCTION

In our previous study [1], we presented high-precision ($\sigma_{\rm obs} \cong 0^m.003$) $WBVR$ photoelectric measurements of RR Lyn carried out at the Tien Shan and Crimean Observatories of the Sternberg Astronomical Institute. The resulting light curves yielded photometric and absolute orbital elements, which could be used to construct a self-consistent geometrical and physical model of this unique eclipsing system, and to confirm the evolutionary status determined in 1995 by Lyubimkov and Rachkovskaya [2, 3]. Table 1 presents the parameters of the system presented in [1] and used below.

Due to its appreciable eccentricity ($e = 0.078$), the orbit of RR Lyn should rotate in space with an apsidal period of about 28 000 yrs, as a result of the effects of general relativity and the tidal and rotational deformation of the components (see Section 2). Lavrov and Lavrova [4] reported the detection of apsidal rotation of RR Lyn with a period of 2000 yrs. However, this period is more than an order of magnitude smaller than that expected theoretically. One of the main goals of our work was to resolve this problem.

In Section 2, we consider the question of apsidal rotation in RR Lyn. It is not possible to derive both ω and its rate of variation $\dot{\omega}$ from the available observations with sufficient accuracy, due to the proximity of the longitude of periastron ω of the eclipsing system to 180°. Therefore, we expect this problem to remain unsolved for quite some time to come.

At the same time, we find that secular variations of the light curve of RR Lyn are primarily associated with the light equation at times of both primary and secondary minima, rather than with apsidal rotation. We present the solution of this equation in Section 3, and have used it to estimate the parameters of a third, unseen object in the system.

2. ROTATION OF THE LINE OF APSIDES

Since our main goal was to study apsidal motion in the system, we first estimated the expected velocity of this motion. The period of apsidal rotation due to both tidal and rotational deformation of the components $U_{\rm cl}$ can be derived from the simple relation [5]

$$\frac{P}{U_{\rm cl}} = C_1 k_{2,1} + C_2 k_{2,2}, \qquad (1)$$

where P is the anomalistic orbital period, $k_{2,i}$ are the known second-order parameters of the apsidal rotation, and C_i are constants that depend on the observed geometrical and physical characteristics of the binary:

$$C_i = \left(\frac{R_i}{a}\right)^5 \left\{ \frac{m_{3-i}}{m_i} 15 f(e) + \left(\frac{w_{r,i}}{w_k}\right)^2 \left(1 + \frac{m_{3-i}}{m_i}\right) g(e) \right\}, \qquad (2)$$

1063-7729/02/4602-0119$22.00

Table 1. Physical and geometrical parameters of the eclipsing RR Lyn

Parameter	Primary	Secondary
Mass M, $M_\odot$	1.89 ± 0.07	1.49 ± 0.05
Radius R, $R_\odot$	2.57 ± 0.04	1.58 ± 0.04
Luminosity L, $L_\odot$	21.04 ± 1.47	5.31 ± 0.32
Effective temperature T_e, K	7570 ± 120	6980 ± 100
Spectral type from $WBVR$ photometry Sp	A6 IV	F0 V
Relative radius r	0.0878 ± 0.0005	0.0541 ± 0.0011
Semimajor orbital axis a, $R_\odot$	29.23 ± 0.34	
Orbital inclination i, deg	87.45 ± 0.11	
Orbital eccentricity e	0.0782 ± 0.0009	
Longitude of periastron ω, deg	185 ± 5	
Distance to the system, pc	73.5 ± 2.8	
Age of the system t, 10^9 yr	1.08 ± 0.15	

where

$$f(e) = (1 + \frac{3}{2}e^2 + \frac{1}{8}e^4)\frac{1}{(1-e^2)^5}, \qquad (3)$$

$$g(e) = (1-e^2)^{-2}. \qquad (4)$$

Here, R_i, m_i, and $w_{r,i}$ are the radius, mass, and angular velocity of axial rotation of component i, a the semimajor axis of the relative orbit, e the eccentricity, and w_k the average angular velocity of the orbital rotation. The indices of the constants C_i and the other parameters, as well as the second indices of the parameter $k_{2,i}$, denote values for the primary ($i = 1$) or secondary ($i = 2$) component.

The relativistic rotation of the line of apsides is determined by the formula [6]

$$\frac{P}{U_{\rm rel}} = 6.37 \times 10^{-6}\frac{M_1 + M_2}{a(1-e^2)}, \qquad (5)$$

where the masses of the components and the semimajor axis of the relative orbit are given in solar units. This rotation has the same direction as the classical rotation due to tidal and rotational deformation of the components. Therefore, the resulting theoretical period of apsidal rotation $U_{\rm th}$ can be derived from the relation

$$\frac{P}{U_{\rm th}} = \frac{P}{U_{\rm cl}} + \frac{P}{U_{\rm rel}}. \qquad (6)$$

Substituting the physical and geometrical parameters of the system from Table 1 into (1)–(6), we obtain

$$U_{\rm th} = 28\,100 \pm 1400 \text{ yr}.$$

In this case,

$$\dot\omega_{\rm rel} = \frac{360^\circ}{U_{\rm rel}} = 0.^\circ0098(4)\ \text{yr}^{-1},$$

$$\dot\omega_{\rm cl} = \frac{360^\circ}{U_{\rm cl}} = 0.^\circ0030(2)\ \text{yr}^{-1},$$

$$\dot\omega_{\rm th} = \dot\omega_{\rm rel} + \dot\omega_{\rm cl} = 0.^\circ0128(5)\ \text{yr}^{-1}.$$

Here and below, the rms errors in units of the last decimal place are given in parentheses. The apsidal rotation constants $k_{2,i}$ in (1) were taken from [7] in accordance with the known masses M_i and gravitational accelerations g_i of the components from Table 1. We can see that the relativistic portion of the periastron motion constitutes 76%. Therefore, as far back as in 1973 [8], it was proposed that RR Lyn could provide a crucial test of the theory of general relativity. Orbital rotations with roughly the same (and even lower) velocities were previously detected in the eclipsing systems DI Her [9], EK Cep [10], V 1143 Cyg [11], V 541 Cyg [12], and others. Therefore, we expected to be able to detect the apsidal rotation velocity $\dot\omega_{\rm obs}$ in RR Lyn as well, since the first photoelectric observations of this system were carried out as long ago as the early 1920s [13].

The rotation of an elliptical orbit in an eclipsing system is usually revealed by a cyclic shift of the secondary minimum at relative phase $0.^p5$ with a period U equal to one complete revolution of the orbit in space.

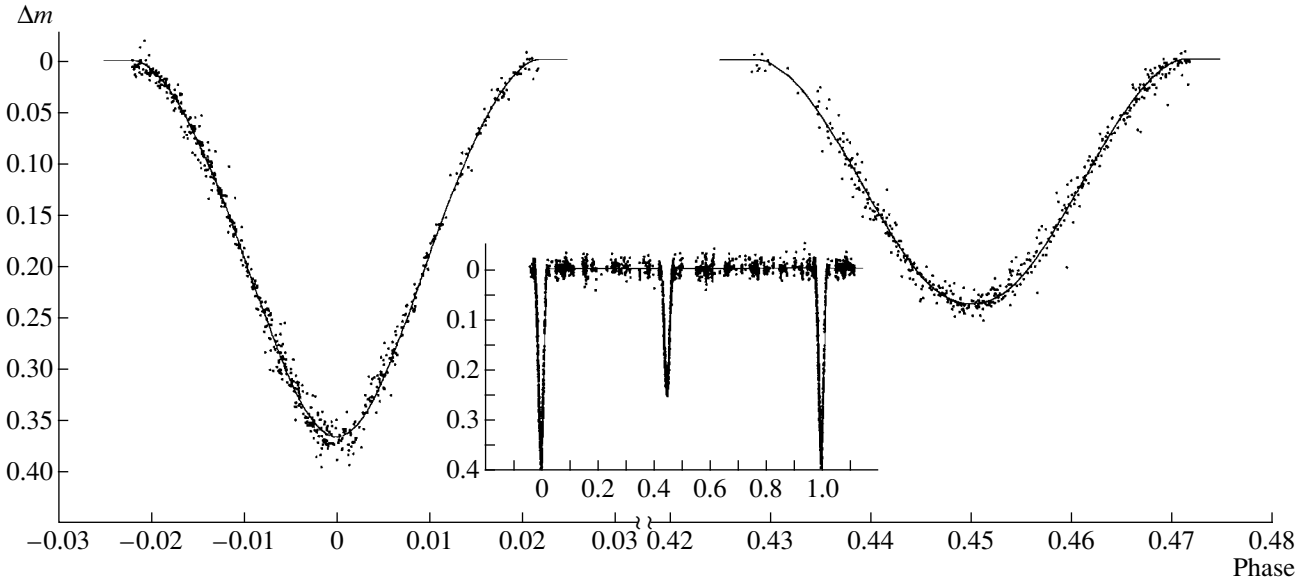

Fig. 1. Master photoelectric light curve of RR Lyn in the $\lambda_{avg} \simeq 4500$ Å band compiled from observations made by various authors. The solid curve represents the standard curve used to determine the times of minima.

However, when U is several tens of thousand years, as in the case of RR Lyn, only the difference between the periods for the primary (P_I) and secondary (P_{II}) minima is detectable [14]:

$$\Delta P = \frac{P_I - P_{II}}{P} = 4e\frac{P}{U} \times \left(\sin\omega - e^2\frac{1+3\sqrt{1-e^2}}{(1+\sqrt{1-e^2})^3}\sin 3\omega\right). \quad (7)$$

Assuming that the anomalistic orbital period P and eccentricity e are constant, we can use this formula to determine U from the observed ΔP and ω.

To derive ΔP from the observations, we first collected all published photoelectric times of minima for RR Lyn. These measurements had low accuracy, apparently due to both random and systematic errors, as well as the different techniques used by different authors. Therefore, we decided to reanalyze all published photoelectric observations of the system using a single method, our iterative differential-correction technique [15], which yields the times of both minima of the light curve of an eclipsing system with an eccentric orbit together with the other photometric elements. The procedure used to determine the times of minima in our iteration technique is similar to the method of Hertzsprung [16]. We used the best theoretical light curve (LC_0) for the given spectral band as a standard curve, relative to which residuals are minimized. This is especially important, because light curves for systems with elliptical orbits are asymmetric relative to the phases of eclipse maxima. This asymmetry is probably one of the reasons for the large scatter in the times of minima obtained by different authors. When constructing the theoretical light curves LC_0, we fixed the geometrical elements—relative component radii $r_{1,2}$, orbital inclination i, and eccentricity e—for all spectral bands to be those for the most accurate ($\sigma_{obs} \approx 0^m.003$) V light curve for RR Lyn, presented in Table 1. The limb-darkening coefficients $u_{1,2}$ were also fixed in accordance with the known effective temperatures of the components $T_{1,2}$ from Table 1 and the observing band.

Figure 1 presents a master light curve of RR Lyn at $\lambda_{avg} \sim 4500$ Å compiled from various observations [1, 13, 17–20]. W, U, V and R observations are also available [1, 17, 19, 20]. We used all these published datasets, weighted in accordance with their accuracies, to determine the average times of minima presented in Table 2. Unfortunately, the authors of [21–23] did not publish their individual observations; therefore, we present the original times of minima determined in [21–23] in the Table. Table 2 also presents the epochs of observations E_I and E_{II} and the differences between the observed, i.e., tabulated (O), and calculated (C) times of minima. The calculated values are based on the linear ephemerides

$$\begin{aligned}\text{Min I} &= \text{JD}_\odot 2\,444\,988^d.49734(45) \\ &+ 9^d.94\,507\,297(28) \times E_I, \\ \text{Min II} &= \text{JD}_\odot 2\,444\,595^d.17\,303(48) \\ &+ 9^d.94\,507\,328(32) \times E_{II}.\end{aligned} \quad (8)$$

Table 2. Heliocentric times of minima derived from photoelectric observations of RR Lyn

No.	$JD_\odot$	E	$O-C$	Reference
	Min I			
1	2425 615.4934(7)	−1948	$-0^d.00180$	Huffer, 1931 [13]
2	2434 675.4583(5)	−1037	+0.00163	Botsula, 1960 [18]
3	2438 046.8367(3)	−698	+0.00029	Linnell, 1966 [19]
4	2442 104.4254(4)	−290	−0.00078	Lavrov *et al.*, 1988 [20]
5	2444 988.49594(25)	0	−0.00140	Khaliullin *et al.*, 2001 [1]
6	2447 524.4924(3)	255	+0.00145	Isles, 1991 [23]
7	2448 936.69194(26)	397	+0.00063	Catton and Burns, 1993 [22]
	Min II			
1	2425 301.7306(9)	−1940	−0.00027	Huffer, 1931 [13]
2	2434 759.4955(5)	−989	−0.00006	Botsula, 1960 [18]
3	2437 941.9175(6)	−669	−0.00151	Linnell, 1966 [19]
4	2444 595.17240(24)	0	−0.00063	Khaliullin *et al.*, 2001 [1]
5	2447 220.67251(26)	264	+0.00013	Catton *et al.*, 1989 [21]
6	2447 568.75226(26)	299	+0.00232	Catton *et al.*, 1989 [21]

These ephemerides were determined simultaneously with the parameters of the light equation (see Section 3). Therefore, they differ from those obtained in [1], where we took the directly observed times of minima as initial values, and the orbital periods were derived without using the light equation.

We can see that the periods for the primary and secondary minima differ:

$$\Delta P_{\rm obs} = P_I - P_{II} = -0^d.00000031(43).$$

However, we cannot draw any firm conclusions about the rate of the apsidal rotation or the consistency of the observed and theoretical parameters of the apsidal motion in the system based on the difference of these periods. First, the derived $\Delta P_{\rm obs}$ is smaller than its error. Second, we can see from (7) that the relation between ΔP and U includes the function ω, which varies rapidly as $\omega \to 180°$. We already noted the low accuracy of ω due to its proximity to 180° when calculating the photometric elements in [1]. A clear confirmation of this is provided by Fig. 2, which presents relations between σ_{O-C} and ω derived from the most accurate V light curve of RR Lyn from [1], with various restrictions for the limb-darkening coefficients of the component disks u_1 and u_2. Here, σ_{O-C} denotes the standard deviations of the observed from the theoretical light curve optimized for a specified value of ω; i.e., σ_{O-C} was minimized based on variation of the other photometric elements, except for the chosen (fixed) ω.

The $\sigma_{O-C}(\omega)$ relations indicate that the optimum values for ω strongly depend on the restrictions imposed on u_1 and u_2. If we impose only the formal restriction $0 < u_{1,2} < 1$ (curve *1* in Fig. 2), the longitude of periastron ω cannot be derived in the interval from 160° to 200°, even using our most accurate light curve. However, we can impose stricter constraints using the known effective temperatures of the components ($T_1 = 7570$ K, $T_2 = 6980$ K, Table 1): $u_1 = 0.55 \pm 0.05; u_2 = 0.60 \pm 0.05$ for the V band. The three curves in Fig. 2 plotted for $u_1 = 0.50, u_2 = 0.55$ (curve *2*); $u_1 = 0.55, u_2 = 0.60$ (curve *3*); and $u_1 = 0.60, u_2 = 0.65$ (curve *4*) indicate that the interval of reasonable ω values can be considerably narrowed:

$$\omega_{\rm obs} = 188° \pm 5°.$$

The shift of the confidence interval for $\omega_{\rm obs}$ by 3° compared to the results of [1] is due to the stricter theoretical constraints we have used for u_1 and u_2. Figure 2 presents the corresponding critical values for σ_{O-C}. We will not consider here the technique applied to determine the confidence intervals for parameters: certain statistical criteria used for this purpose are described in detail in [24–26]. For the extreme values of ω, σ_{O-C} increases from the minimum value $0^m.00316$ for $\omega = 188°$ to $0.^m00319$, that is, by only 1%. The maximum absolute value of the deviation of the theoretical light curves from the optimum light curve LC_0 for $\omega = 183°$ and 193° is smaller than $0.^m0015$ ($< 1/2\,\sigma_{O-C}$). This is illustrated by Fig. 3a,

which plots the deviations from LC_0 of individual V observations of RR Lyn in Min II from [1] together with the deviations of the theoretical curves for $\omega = 183°$ and 193° from the same optimum curve. We can see that, in this interval, the theoretical curves for different ω values are difficult to distinguish against the background of the measurement errors and brightness microfluctuations. We do not present the corresponding plot for Min I; however, it displays a similar pattern. Figure 3 clearly demonstrates that, even using the most accurate light curve, the uncertainty in the longitude of periastron is no less than 10°.

If we substitute the derived ω_{obs} into (7), the observed and theoretical ΔP have the same sign. However, the magnitude of the function of ω in (7) varies by a factor of a few over the resulting interval for the longitude of periastron. Therefore, we conclude that we will not be able to determine the apsidal period of RR Lyn with in the next few decades, even if the accuracy of ΔP_{obs} is considerably increased due to the large uncertainty in ω. Thus, the problem of determining the apsidal rotation rate in this system will probably remain unsolved at least during the current century.

Here, we note the following. First, further increase in the accuracy of observations will not yield any substantial increase in the accuracy of ω, since the achieved $\sigma_{O-C} = 0^m.0032$ is essentially limited by physical brightness microfluctuations that occur in δ Sct stars [1] rather than by random measurement errors. Second, given the accuracy of other published observations RR Lyn ($\sigma_{obs} \approx 0^m.010$), the interval of reasonable ω values extends from 160° to 200°, even for fixed u_1 and u_2; this is illustrated in Fig. 3b, which is analogous to Fig. 3a but is based on the observations of Botsula [18]. It is clear from Figs. 2 and 3 that, when the measurement accuracy is worse than $0^m.004$, we cannot even determine the quadrant in which ω is located, so that even the direction of the apsidal rotation cannot be found.

3. LIGHT EQUATION IN THE TIMES OF MINIMA AND PARAMETERS OF THE THIRD BODY

In spite of our lack of success in determining the apsidal rotation rate, the revised times of minima for RR Lyn and the substantial increase in their accuracy are useful results. Indeed, they suggest a possible reason for the contradiction between the expected variations in the orbital period [18] and the apparent detection of apsidal rotation with an anomalously short period [4, 20]. Figure 4 presents the deviations of the observed (O) times of minima (Table 2) from those calculated (C) using the linear ephemerides (8).

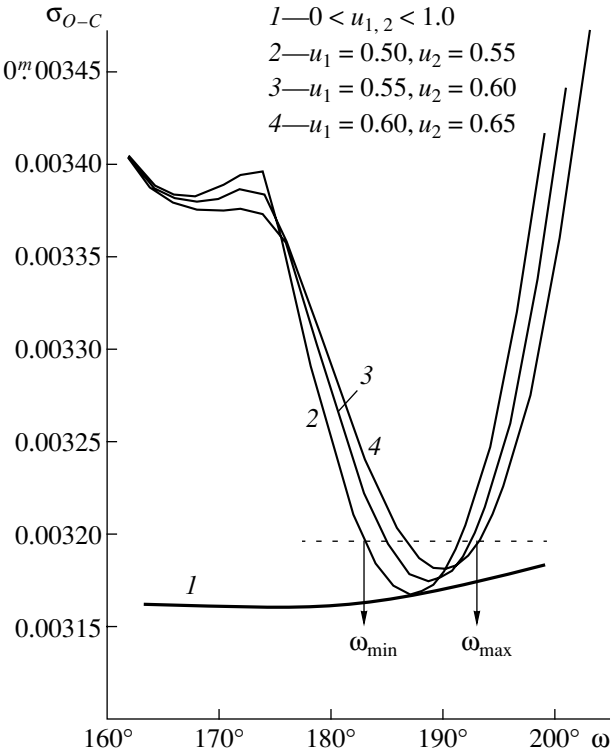

Fig. 2. Relations between σ_{O-C} and the longitude of periastron ω derived from the most accurate V light curve for RR Lyn from [1] for various restrictions on the linear limb-darkening coefficients for the components u_1 and u_2.

We can see that these deviations display a quasi-periodic wave. The $(O-C)$ values for both minima are closely correlated, and their time dependence clearly indicates the presence of a third body in the system. The orbital parameters for such a multiple system are determined from the so-called "light equation" [27]:

$$(O-C) + A = \frac{Z}{c} = \frac{a_3 \sin i_3}{c}(1 - e_3 \cos E)\sin(v + \omega_3), \quad (9)$$

where v and E are the apparent and eccentric anomalies, respectively; c, the velocity of light; a_3, the semi-major axis; i_3, the inclination; e_3, the eccentricity; and ω_3, the longitude of periastron of the eclipsing star's orbit relative to the center of gravity of the triple system. In this equation, the constant A ensures that Z/c is equal to zero when the line of nodes is intersected by the eclipsing binary, i.e., when the distance to the eclipsing binary is equal to the distance to the center of gravity of the triple system. The light equation is solved by minimizing the sum of the squared deviations, yielding the elements of the linear ephemerides (8) and the orbital parameters of the triple system:

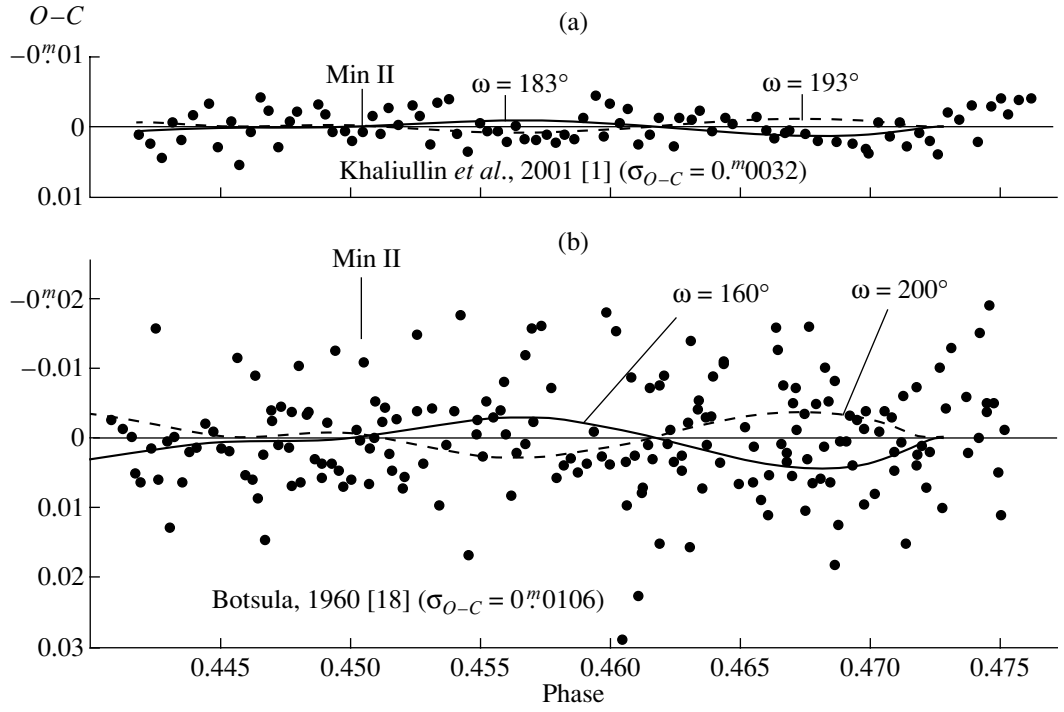

Fig. 3. Deviations of individual measurements of RR Lyn in Min II from the optimum theoretical light curve LC_0 for (a) V observations from [1] and (b) the $\lambda_{avg} = 4500$ Å observations of Botsula [18]. The deviations of theoretical curves from LC_0 corresponding to the boundaries of the ω confidence intervals are also plotted.

$$P_3 = 39.7 \pm 4.2 \text{ yrs},$$
$$a_3 \sin i_3 = (7.3 \pm 1.1) \times 10^{12} \text{ cm} = 0.48 \pm 0.07 \text{ AU},$$
$$e_3 = 0.96 \pm 0.02, \quad \omega_3 = 28^\circ \pm 8^\circ,$$
$$T_3 = \text{JD } 2\,447\,520 \pm 90.$$

Here, P_3 is the period of the orbital rotation of the third body, and T_3 is the time of its periastron passage. The derived parameters can be used to calculate the mass function of the triple system

$$f(M) = \frac{M_3^3 \sin^3 i_3}{(M_1 + M_2 + M_3)^2} \qquad (10)$$
$$= \frac{a_3^3 \sin^3 i_3}{P_3^2} = 7.23 \times 10^{-5} M_\odot.$$

Here, the masses are given in solar masses, a_3 is in astronomical units, and P_3 is in years. Substituting $M_1 + M_2 = 3.38 M_\odot$ (Table 1), we obtain

$$M_3 \sin i_3 = (0.10 \pm 0.02) M_\odot.$$

This value can be used to estimate the semimajor orbital axis of the third body relative to the center of gravity of the entire system:

$$A_3 \sin i_3 = a_3 \sin i_3 \frac{M_1 + M_2}{M_3} = 17.4 \pm 3.5 \text{ AU}.$$

The solid curve in Fig. 4 represents the theoretical curve for the light equation (9) calculated using the above orbital parameters of the triple system. Deviations of the observations from this curve do not exceed $\pm 2\sigma$. At the same time, deviations of the observed times of minima from the linear ephemerides reach $\pm 6\sigma$, as is evident from Table 2.

4. DISCUSSION

The contribution of the star with $M_3 = 0.10 M_\odot$ to the total luminosity of RR Lyn in the optical is negligibly small. It is impossible to detect such a star spectroscopically against the background of the brighter binary components. A third light of this strength is also essentially impossible to detect in the light curve of the eclipsing system. In essence, the only possibility for further study and refinement of the physical parameters for this triple system is provided by measurements of the times of minima and derivation of highly accurate light curves, in order to detect signs of the dynamical effect of the third body on the orbit of the binary. Simulations indicate that the consequences of this effect could be quite varied [28], even possibly including the disappearance of the

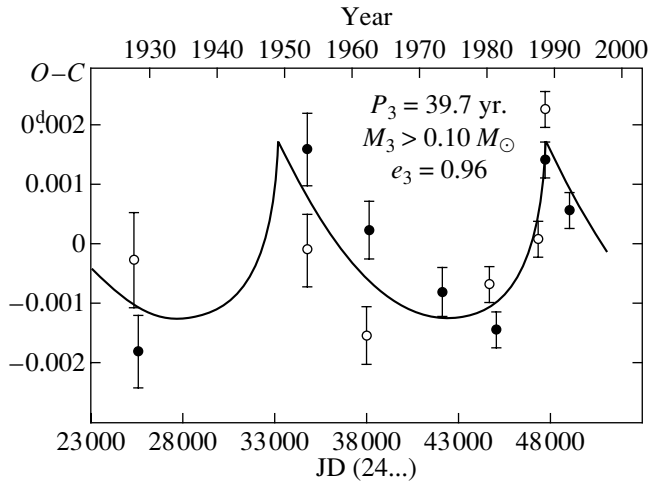

Fig. 4. Time-dependence of the difference between the observed (O) and theoretical (C) times of minima of the eclipsing star RR Lyn. The C values are calculated using the linear ephemerides (8). The filled and hollow circles refer to the primary and secondary minima, respectively. The solid curve presents the theoretical curve for the light equation (9), calculated using the orbital parameters of the triple system obtained here.

eclipses due to variation of the orbital inclination of the eclipsing system [29, 30].

Currently, in addition to the lower limit for the mass M_3, we can also estimate its upper limit. For this purpose, we plotted the relation between σ_{O-C} and L_3^V analogous to that between σ_{O-C} and ω in Fig. 2. This dependence indicated that the contribution of the third body to the visual luminosity of the system is $L_3^V < 0.03$. According to the mass–luminosity relation for main-sequence stars, this imposes the following restriction on the mass of the third body and, accordingly, on the inclination of the orbit of the triple system relative to the plane of the sky:

$$M_3 < 0.9 M_\odot, \quad i_3 > 7^\circ.$$

Using numerical procedures presented in [28], we can calculate possible time variations of the orbital parameters of the eclipsing system (i, e, ω) due to the dynamical interaction of the components. These estimates indicate that such dynamical variations of the light curve should be detectable, and that high-precision photoelectric and spectroscopic measurements aimed at refining the parameters of this unique triple system should be continued.

REFERENCES

1. Kh. F. Khaliullin, A. I. Khaliullina, and A. V. Krylov, Astron. Zh. **78**, 1014 (2001) [Astron. Rep. **45**, 888 (2001)].
2. L. S. Lyubimkov and T. M. Rachkovskaya, Astron. Zh. **72**, 64 (1995) [Astron. Rep. **39**, 56 (1995)].
3. L. S. Lyubimkov and T. M. Rachkovskaya, Astron. Zh. **72**, 72 (1995) [Astron. Rep. **39**, 63 (1995)].
4. M. I. Lavrov and N. V. Lavrova, Astron. Tsirk., No. 1165, 3 (1981).
5. Z. Kopal, *Dynamics of Close Binary Systems* (Reidel, Dordrecht, 1978).
6. T. Levi-Civita, Am. J. Math. **59**, 225 (1937).
7. A. Claret and A. Giménez, Astron. Astrophys., Suppl. Ser. **96**, 255 (1992).
8. R. H. Koch, Astrophys. J. **183**, 275 (1973).
9. D. Ya. Martynov and Kh. Khaliullin, Astrophys. Space Sci. **71**, 147 (1980).
10. Kh. F. Khaliullin, Astron. Zh. **60**, 72 (1983) [Sov. Astron. **27**, 43 (1983)].
11. Kh. F. Khaliullin, Astron. Tsirk., No. 1262, 1 (1983).
12. Kh. F. Khaliullin, Astrophys. J. **299**, 668 (1985).
13. C. M. Huffer, Publ. Waschburn Obs. **15**, 199 (1931).
14. Kh. F. Khaliullin, in *Binary Stars* [in Russian] (Kosmosinform, Moscow, 1997).
15. A. I. Khaliullina and Kh. F. Khaliullin, Astron. Zh. **61**, 393 (1984) [Sov. Astron. **28**, 228 (1984)].
16. E. Hertzsprung, Astron. Nachr. **210**, 17 (1919).
17. N. L. Magalashvili and Ya. I. Kumsishvili, Byull. Akad. Nauk Gruz. SSR, Abastumanskaya Astrofiz. Obs., No. 24, 13 (1959).
18. R. A. Botsula, Byull. Astron. Obs. im. Éngel'garda, No. 35, 43 (1960).
19. A. P. Linnell, Astron. J. **71**, 458 (1966).
20. M. I. Lavrov, N. V. Lavrova, and Yu. F. Shabalov, Tr. Kazan. Gor. Astron. Obs. **51**, 19 (1988).

21. D. B. Catton, R. L. Hawkins, and W. C. Burns, Inf. Bull. Var. Stars, No. 3408 (1989).
22. D. B. Catton and W. C. Burns, Inf. Bull. Var. Stars, No. 3900 (1993).
23. J. Isles, BAAVSS Circ., No. 72, 22 (1991).
24. E. Budding, Astrophys. Space Sci. **22**, 87 (1973).
25. A. V. Goncharskiĭ, A. M. Cherepashchuk, and A. G. Yagola, *Ill-Posed Problems in Astrophysics* [in Russian] (Nauka, Moscow, 1985).
26. A. V. Goncharskiĭ, V. V. Stepanov, and A. M. Cherepashchuk, Astron. Zh. **63**, 725 (1986) [Sov. Astron. **30**, 430 (1986)].
27. D. Ya. Martynov, Izv. AOÉ, No. 25, 5 (1948).
28. Kh. F. Khaliullin, S. A. Khodykin, and A. I. Zakharov, Astrophys. J. **375**, 314 (1991).
29. L. V. Mossakovskaya, Pis'ma Astron. Zh. **19**, 87 (1993) [Astron. Lett. **19**, 35 (1993)].
30. L. Tomasella and U. Munari, Astron. Astrophys. **335**, 561 (1998).

Translated by K. Maslennikov

Astronomy Reports, Vol. 46, No. 2, 2002, pp. 127–138. Translated from Astronomicheskiĭ Zhurnal, Vol. 79, No. 2, 2002, pp. 145–157.

Parameters of UX CVn

V. V. Shimanskiĭ

Kazan State University, ul. Lenina 18, Kazan, 420008 Tatarstan, Russia

Received April 2, 2001

Abstract—We have derived a complete set of parameters for the close binary system UX CVn made up of degenerate objects based on photometric and spectral observations. The total mass of the components is close to one solar mass, so that its further evolution cannot result in a type-I supernova. The spectrum of the binary indicates that the surface temperature of the hot subdwarf may have increased by 2000 K over 40 years. This heating rate is consistent with theoretical estimates for evolutionary tracks of low-luminosity hot subdwarfs. We also determined the abundances for ten elements in the atmosphere of the primary, which are consistent with the hypothesis that the binary is a member of Population II. There are signs of synthesized material ejected onto the surface of the star. © *2002 MAIK "Nauka/Interperiodica".*

1. INTRODUCTION

The evolutionary status of the binary UX CVn remained unknown over the past two latest decades. The nature of the secondary could not be determined from the radiation received from the system: light curves did not include an eclipse phase, and the spectra displayed only lines of the primary, without any emission features. Accordingly, studies of UX CVn [1–4] have considered the primary to be a hot subdwarf of low luminosity and the secondary to be a cool white dwarf. However, Ritter [5] pointed out the internal inconsistency of a model for the system with two evolved stars and a substantial orbital period ($P_{\rm orb} = 0.573703$ days). He classified the binary as a precataclysmic variable containing a late-type main-sequence star. Further reviews of close binaries classified UX CVn in various ways: some concluded that its status was uncertain [6, 7], while others assigned the system to the class of precataclysmic variables [8, 9] or suggested it was a degenerate-object binary [10, 11].

To resolve this uncertainty, Shimanskiĭ *et al.* [12] acquired ten moderate-resolution spectra of the system, which they used to model UX CVn in the framework of both hypotheses about its nature. When the theoretical models and observations at different orbital phases were compared, it became apparent that the spectra did not display the reflection effect associated with the presence of a main-sequence star and that the secondary was a white dwarf. In this way, the evolutionary status of the variable as a degenerate-object binary was finally established.

Searches for degenerate-object binary systems and estimation of their parameters have recently received increasing attention. This is due in part to the evolutionary calculations for an completely detached degenerate-object binary of [9, 13], which indicate that these objects may be the progenitors of type-I supernovae. As a result, a number of studies of the spectra of single white dwarfs have been carried out since the mid-1980s, searching for signs of binarity. In spite of appreciable difficulties, these studies have yielded positive results. The review of Saffer *et al.* [14] generalizes data for 13 detached degenerate-object binaries with periods between 0.15 and 4.8 days. It is extremely difficult to determine the probabilities that specific systems will be transformed into supernovae, since the necessary parameters remain largely unknown. The masses of both components have been estimated only for three degenerate-object binaries, while the mass of the less massive star is known for five systems. Under these conditions, the current evolutionary status of UX CVn enables the following promising studies, which can potentially provide information about the physics of degenerate-object binaries.

(1) Determination of all or most of the parameters of the system, which, in the case of UX CVn, can only be performed via joint analyses of the light curves, radial velocities, and spectra of the primary component, i.e., without applying stellar-evolution theory. The effectiveness of this approach was shown in [15] for the object KPD 0422+5421.

(2) Studies of the chemical composition of the primary via modeling of synthetic spectra. These results are relevant for further developments of the theory of the chemical-element synthesis, since degenerate-object binaries are believed to undergo two common-envelope stages so that they should display signs of inner material ejected onto their surfaces.

1063-7729/02/4602-0127$22.00

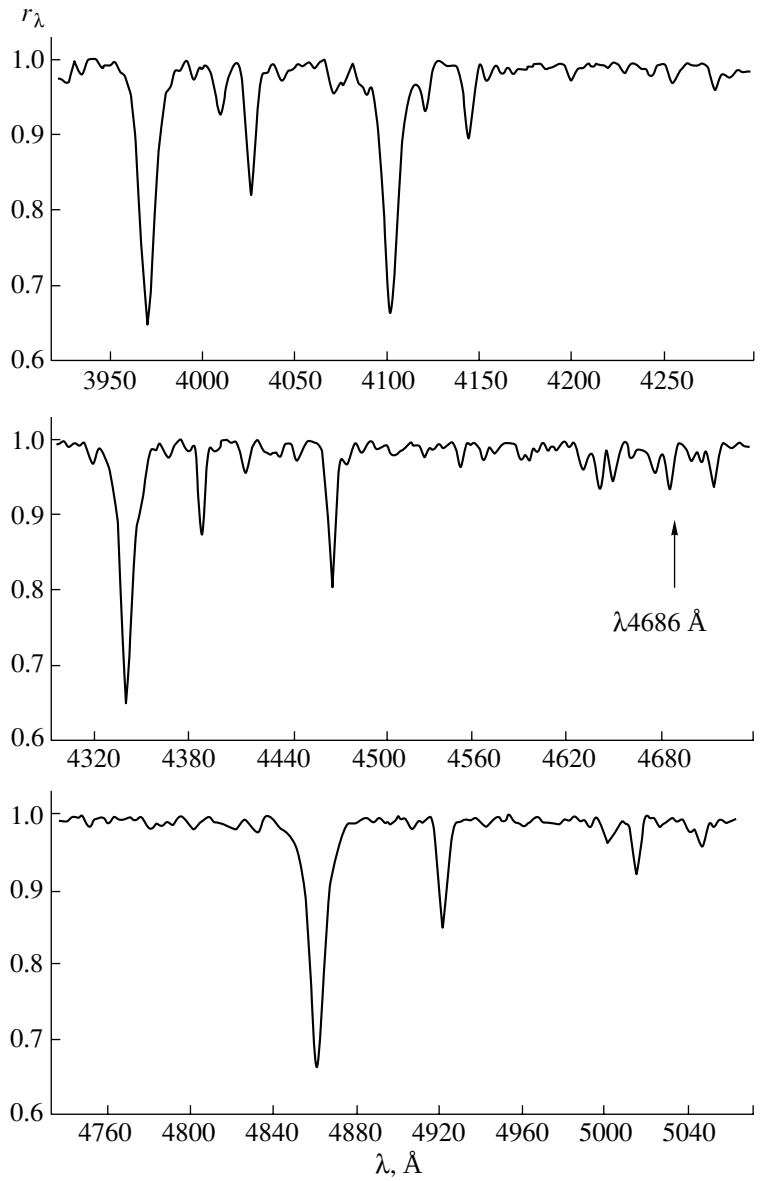

Fig. 1. Observed spectrum of UX CVn. The arrow indicates the HeII λ4686 Å line.

(3) Detailed studies of the radial-velocity curve derived from a large set of new observations, aimed at searches for effects of tidal deceleration of the stars. Only isolated studies of this type exist; however, they can provide unique information about the inner structure of the cores of hot stars, where there is residual burning of helium and hydrogen.

Some of these problems can be attacked using available observations. Here, we analyze observational data for UX CVn and redetermine some of the system's parameters, as well as its chemical composition. Section 2 presents a preliminary analysis of the spectrum of UX CVn and identification of lines. Section 3 describes the methods used in our modeling of UX CVn and the derived parameters of the system. Section 4 discusses the technique used to determine the chemical composition of the primary and the results obtained.

2. SPECTRA OF UX CVn

We analyzed spectra of UX CVn using the data acquired in [12]. The star was observed at the Nasmyth-1 focus of the 6-m telescope of the Special Astrophysical Observatory in the Northern Caucasus, with an SP-124 spectrograph [16] and a PM1024 CCD array (with pixel size 24 × 24 micron). In addition, ten individual spectrograms were acquired at three phases of the orbital period, $\varphi = 0.20, 0.42, 0.64$, in the interval $\Delta\lambda 3920$–5250 Å with

Table 1. Lines in the spectrum of UX CVn and the equivalent widths determined in the current study (W_{shi}) and in [11] (W_{hrk})

λ, Å	W_{shi}, Å	W_{hrk}, Å	Identification
3933 b	0.097		HeI(3935), CaII(3933)
3944 s	0.049		OII(3945)
3970 s	3.900		H_ϵ, He(3964)
3995 s	0.098	0.087	NII(3995)
4009 s	0.520		HeI(4009)
4026 s	1.078		HeI(4026)
4035 s	0.079		NII(4035)
4042 s	0.176	0.082	NII(4041, 4043)
4048 b	0.038		OII(4048)
4054 s	0.018		OII(4054)
4070 s	0.241	0.172	OII(4069, 4069, 4072)
4075 s	0.131		OII(4075)
4085 s	0.225		OII(4083, 4084, 4085)
4088 s	0.405		OII(4089), SiIV(4088)
4102 s	3.930		H_δ
4119 s	0.347		HeI(4120), OII(4119, 4120, 4121)
4132 b	0.030		OII(4132)
4143 s	0.687		HeI(4143), OII(4141, 4142, 4145)
4153 s	0.143	0.122	OII(4153), CIII(4152)
4169 s	0.078	0.084	HeI(4168), OII(4169)
4185 b	0.031		OII(4185)
4189 b	0.023		OII(4189)
4199 b	0.120		HeII(4199), NII(4199), NIII(4200)
4219 s	0.028		NeII(4219)
4227 b	0.063		NII(4227)
4241 s	0.071	0.081	NII(4241)
4251 s	0.134		OII(4253,4254), SII(4253)
4265 s	0.010		CII(4267), OII(4263)
4275 b	0.168		OII(4275, 4276, 4276, 4277, 4277)
4281 s	0.046		OII(4281,4282)
4284 s	0.098	0.068	OII(4283), SIII(4285)
4291 b	0.049		OII(4291)
4303 b	0.055	0.067	OII(4302, 4303,4303, 4303)
4318 b	0.164		OII(4317, 4319, 4319)
4340 s	3.910		H_γ
4349 s	0.321		OII(4345,4347, 4349, 4351)
4366 s	0.174	0.147	OII(4366, 4369), SIII(4364)
4378 s	0.092	0.080	OII(4378, 4378)
4388 s	0.668		HeI(4387)
4396 s	0.097		OII(4395)

Table 1. (Contd.)

λ, Å	W_{shi}, Å	W_{hrk}, Å	Identification
4415 s	0.269	0.180	OII(4414, 4416)
4437 s	0.118	0.047	HeI(4437)
4448 s	0.162	0.085	OII(4446, 4448, 4448), NII(4447)
4471 s	1.230		HeI(4471), OII(4465, 4467, 4469)
4480 s	0.172	0.047	MgII(4481, 4481), AlIII(4479, 4479)
4488 s	0.085	0.085	OII(4488, 4489, 4489)
4499 s	0.084		OII(4500), NeII(4499, 4499)
4529 s	0.106	0.069	NII(4530), AlIII(4528, 4529)
4541 b	0.056		HeII(4541)
4552 b	0.146	0.112	SiIII(4552)
4566 s	0.104	0.101	SiIII(4567)
4574 s	0.086		SiIII(4574)
4591 s	0.142	0.158	OII(4591)
4596 s	0.090	0.085	OII(4596)
4601 s	0.056	0.070	OII(4602), NII(4601)
4608 s	0.045	0.037	OII(4609), NII(4607)
4613 s	0.047	0.037	OII(4613, 4613)
4629 s	0.255		CII(4629), NII(4630), SiIV(4631, 4631)
4640 s	0.367		OII(4638, 4641), NIII(4640)
4649 s	0.301		OII(4649, 4650), CIII(4647, 4650, 4451)
4661 s	0.128		OII(4661)
4675 s	0.265		OII(4673, 4676)
4686 s	0.380		HeII(4685)
4698 s	0.140		OII(4699, 4699)
4704 s	0.121		OII(4705)
4712 s	0.331	0.219	HeI(4713)
4751 b	0.061		OII(4751)
4819 s	0.108		SiIII(4819, 4819)
4828 s	0.148		SiIII(4828)
4862 s	3.690		H_β
4906 s	0.072		OII(4906)
4921 s	0.954		HeI(4921)
4942 b	0.075		OII(4941, 4943)
4993 s	0.048		NII(4994)
5000 s	0.173		NII(5001, 5001)
5005 s	0.064		NII(5005)
5014 s	0.359	0.245	HeI(5015)
5046 s	0.188		HeI(5047), NII(5045)

Note: The notation “s” and “b” in the first column is explained in the text.

a two-pixel resolution of 2.6 Å. The spectrograms were processed in the MIDAS package using standard techniques [17]. Subsequently, the individual spectrograms for each phase were added, transformed to the laboratory wavelength system, and normalized using a synthetic comparison spectrum [12].

Our analysis of the spectra of UX CVn [12] indicated that variations in line profiles with orbital phase are minimal (smaller than 2–3% in equivalent width); they are determined by the asphericity of the primary, and can easily be taken into account in spectral modeling. Therefore, to increase the signal-to-noise ratio, the spectra at phases $\varphi = 0.20$, 0.42, and 0.64 were averaged and then renormalized using the procedure described in [12]. In this way, we obtained a spectrum of UX CVn with a signal-to-noise ratio of ~ 210, presented in Fig. 1.

The lines in the observed spectra were identified via comparison with a synthetic spectrum calculated using the SYNTH code and a Kurucz [18] model atmosphere with $T_{\rm eff} = 29\,250$ K, $\log g = 4.04$ [19], and solar chemical composition [20]. The equivalent widths of the observed lines were determined by direct integration and approximation with Gaussian and Lorentzian profiles or by convolution with a set of Gaussian and Lorentzian profiles approximating several close lines. Table 1 presents a complete list of the identified lines together with the equivalent widths measured both in our study and by Hambly *et al.* [11]. We estimate the errors in the equivalent widths to be from $\Delta W = \pm 15$ mÅ for unblended lines with $W_{\rm shi} <$ 120 mÅ to $\Delta W = \pm 30$ mÅ for lines with $W_{\rm shi} >$ 120 mÅ. For strong hydrogen and helium lines, the errors are about 6–8% of $W_{\rm shi}$. A substantial number of the observed lines include contributions from several components of various elements; this information is also presented in Table 1. Line profiles marked by an "s" were used to determine the parameters of the primary's atmosphere and its chemical composition (see Sections 3, 4), while lines marked by a "b" were considered unsuitable for quantitative analyses.

Based on 40 spectrograms obtained with the 5-m Mt. Palomar telescope, Greenstein [2] derived the following equivalent widths for strong lines: $W_{\rm H} = 3.82$ Å for the average width of H_β and H_γ; $W_3 = 2.33$ Å for the total width of the $\lambda\lambda$4026, 4471 Å neutral-helium triplet; $W_1 = 1.65$ Å for the single $\lambda\lambda$4009, 4144, 4387 Å lines; and $W_{\rm Mg} = 0.19$ Å for the λ4481 Å Mg line. The corresponding values obtained in our study ($W_{\rm H} = 3.80$ Å, $W_3 = 2.31$ Å, $W_1 = 1.87$ Å, $W_{\rm Mg} = 0.17$ Å) are completely consistent with the data of [2], within the probable errors in W.

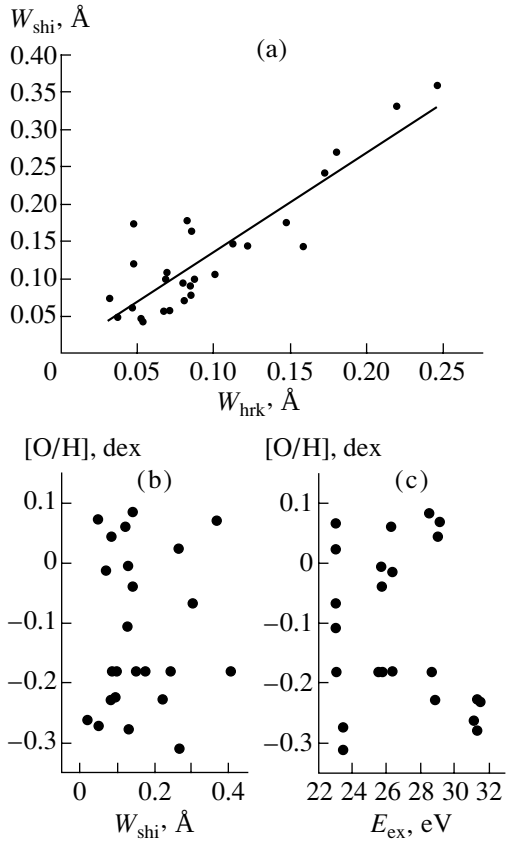

Fig. 2. Relations between (a) our equivalent widths $W_{\rm shi}$ and those obtained in [11] $W_{\rm hrk}$; (b) the abundances [O/H] and equivalent widths $W_{\rm shi}$; and (c) the abundances [O/H] and excitation potentials for the lower levels $E_{\rm ex}$ of the lines studied.

Figure 2a shows that, for many faint lines, our equivalent widths $W_{\rm shi}$ are systematically larger than the values $W_{\rm hrk}$ obtained by Hambly *et al.* [11], who analyzed echelle spectra of UX CVn with resolution $\Delta\lambda/\lambda = 22\,000$–$60\,000$. The linear approximation of the $W_{\rm hrk}$–$W_{\rm shi}$ dependence plotted in Fig. 2a yields the relation $W_{\rm shi} = 5$ mÅ $+ 1.342 W_{\rm hrk}$. These discrepancies are probably primarily due to the fact that only a Gaussian approximation is used to determine the line equivalent widths in [11]. Our analysis indicates that all lines with equivalent widths larger than 120 mÅ display substantial wings, which are not taken into account in a purely Gaussian approximation. Another factor affecting the calculated equivalent widths is the uncertainty in the continuum level. As we can see from Table 1, significant differences in W occur primarily in lines in the wavelength interval $\Delta\lambda$4410–4485 Å. However, the consistency between $W_{\rm shi}$ for the HeI λ4471 Å and MgII λ4481 Å lines and the data from [2] confirms that we have correctly determined the continuum level in this interval.

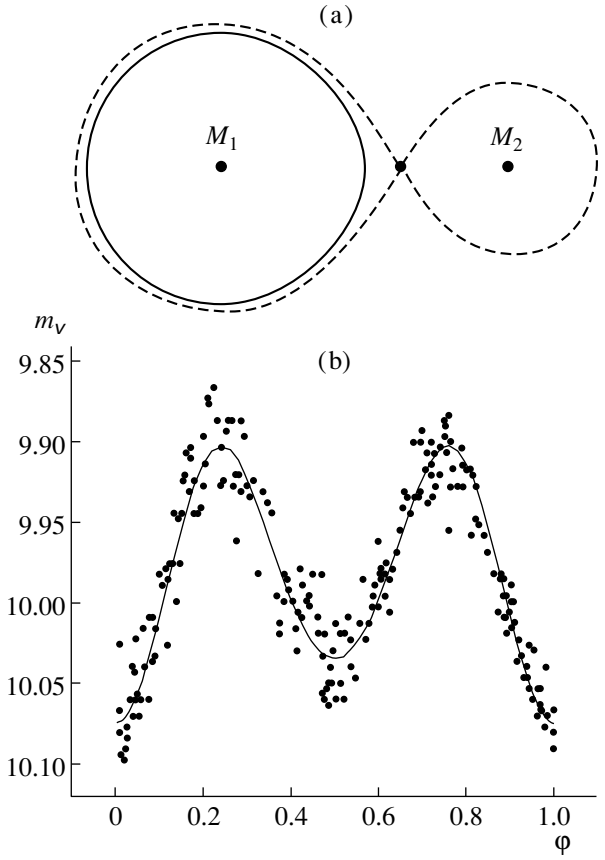

Fig. 3. (a) Model of UX CVn and (b) the observed [28] (dots) and theoretical (curve) V light curves for the system parameters in Table 2.

3. DETERMINATION OF PARAMETERS OF UX CVn

Figure 3 presents our model for UX CVn as a degenerate-object binary. The primary, a B subdwarf with a degenerate helium core and thin hydrogen envelope [9], is approaching the filling of its Roche lobe and has a distorted shape, while the secondary is a low-luminosity white dwarf. We assumed that the contribution of the secondary to the total luminosity of the system is insignificant, as is confirmed by the presence of only single lines in the spectra of UX CVn. In addition, the evolution of a star after ejection of its supergiant envelope to a white dwarf with temperature $T_{\rm eff} = 15\,000$ K lasts about 10^7 yr [9], which is several orders of magnitude shorter than the star's main-sequence lifetime. Therefore, it is very unlikely that UX CVn contains a white dwarf with an effective temperature higher than $T_{\rm eff} = 20\,000$ K.

We specified the following set of parameters affecting the system's radiation and accessible to estimation:

A—the semimajor axis (in solar radii $R_\odot$),

i—the orbital inclination to the line of sight,

M_1—the mass of the primary (in solar masses $M_\odot$),

R_1—the radius of the primary (in solar radii $R_\odot$),

$T_{\rm eff}$—the effective temperature of the primary,

$q = M_2/M_1$—the mass ratio of the components.

To calculate the orbital phases $\varphi \equiv E$, we used the refined ephemeris [12]

$$\mathrm{JD} = 2441096.177 + 0.573704E. \qquad (1)$$

The temperature $T_{\rm eff}$ can be derived from spectroscopic observations independently from the other parameters. These remaining parameters are determined from a closed system of five equations and relations, the first of which is the generalized Kepler's law

$$\frac{P^2 M_1 (1+q)}{A^3} = 0.0135, \qquad (2)$$

where P is the orbital period in days. The second equation relates some parameters with the mass function of the system

$$\frac{M_1 q^3}{(1+q)^2}\sin^3(i) = f(m), \qquad (3)$$

which is derived from the radial-velocity curve. Here, we will use the value $f(m) = 0.110$ previously obtained in [12] for models with circular and elliptical orbits, and consistent with the value $f(m) = 0.113$ obtained in [2].

Supplementary relations can be derived from the light curves via theoretical modeling of the radiation of a star close to filling its Roche lobe and alternately turning its tidal zones toward the observer. In this case, the light curve depends on all parameters of the system; for the V band, it can be expressed in the general form

$$F_V(M_1, q, A, R_1, \sin(i), T_{\rm eff}, \varphi) = m_V(\varphi). \qquad (4)$$

Constraints on the desired parameters are imposed by the requirement of maximum consistency between the theoretical and observed distributions $m(\varphi)$ in the UBV bands, based on a χ^2 criterion. In [12], we describe our model for the radiation of a star that is close to filling its Roche lobe and derive corresponding theoretical light curves using the ROSHE package [12]. The observed light curve was based on photometric observations carried out by Nelson and Mielbrecht on the 1.3-m telescope of the Kitt Peak Observatory [4]. We used only the most reliable V light curve, for which the errors of individual observations were about 0.05^m.

In a similar way, in their analysis of photometric observations for KPD 0422+5421, Koen *et al.* [15]

acquired three additional constraints for the elements of the system. As a result, all parameters were determined using only light curves and radial velocities in [15]. However, our test calculations indicate that, due to the low quality of the UX CVn photometric data, only two additional constraints can be imposed, specified by the total amplitude of the brightness variations and the difference in the depths of the minima (Fig. 3b).

A closed system of equations is formed by the addition of a fifth relation involving the gravitational force at the surface of the primary $\log g_1$:

$$\log M_1 - 2\log R_1 = \log g_1 - \log g_\odot. \qquad (5)$$

The atmospheric parameters $\log g_1$ and $T_{\rm eff}$ can be derived simultaneously from the available spectroscopic and photometric data. In the case of UX CVn, the atmospheric parameters of the primary vary over its surface and, accordingly, with the orbital period of the system. A preliminary analysis of the light curve carried out using the ROSHE package indicated that the amplitude of the temperature variations over the orbital period was $\Delta T_{\rm eff} \approx 500$ K, while the corresponding amplitude of variations in the gravitational force was $\Delta \log g_1 \approx 0.02$. These values are comparable to the probable errors in these parameters, which we derived by averaging over the orbital period. To take into account variations of the atmospheric parameters over the orbital period, we computed theoretical spectra separately for $\varphi = 0.20$, 0.42, and 0.64; the different $T_{\rm eff}$ and $\log g_1$ values at different phases were specified using estimates obtained from the light curve analysis made using the ROSHE package.

We estimated $\log g_1$ and $T_{\rm eff}$ using three methods:

(a) from the profiles of the Balmer lines;

(b) from a consideration of ionization balance for neutral and ionized helium;

(c) from various photometric data.

We modeled the profiles of hydrogen and helium lines using the SYNTH code to calculate a synthetic spectrum taking into account about 500 000 lines from the lists of Kurucz [18]. In the profile calculations, we took into account Stark broadening in accordance with the theory developed by Vidal, Cooper, and Smith [21] for the Balmer lines and with the results of [22, 23] for the helium lines. Stark broadening for the remaining lines was taken into account using the approximate formula proposed by Kurucz and Furenlid [24]. As additional broadening parameters, we considered the microturbulence velocity $\xi_{\rm turb} = 3.0$; the instrumental profile, approximated by a Gaussian with half-width 2.6 Å and the rotational velocity $V\sin(i)$, chosen individually for each line to achieve the best consistency between the observed and theoretical profiles. We took into account possible deviations from LTE for HeI lines using a 38-level atomic model and the non-LTE computation method of [25]. The non-LTE populations of HeI levels were calculated with the NONLTE3 package developed by Sakhibullin [26] and modified by Auer and Heasley [27] for total linearization. Further, these non-LTE populations were used directly in our calculations of the synthetic spectra using the SYNTH code.

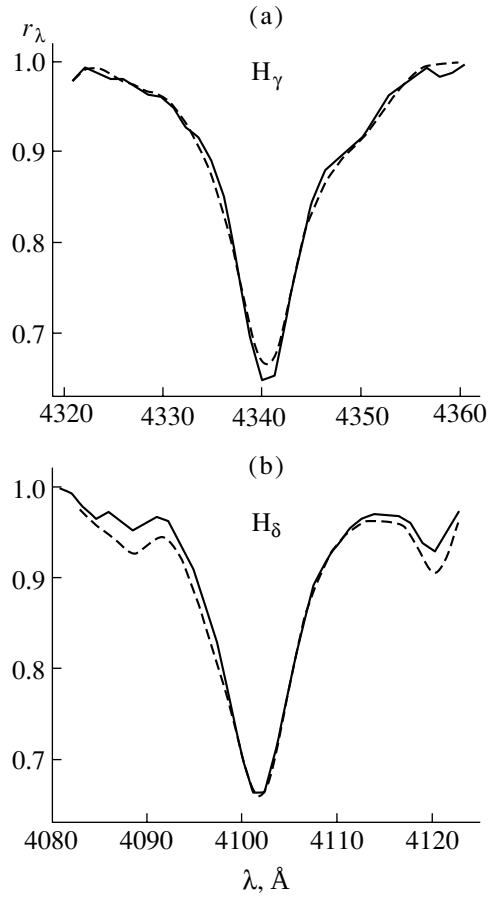

Fig. 4. Observed (solid) and theoretical (dashed) (a) H_γ and (b) H_δ profiles in the spectrum of UX CVn. Model atmospheric parameters are from Table 2.

Since our preliminary study of the spectrum indicated the need for a substantial increase in the helium abundance, we investigated the possible effect of variations in the atmospheric chemical composition on the structure of the star. Blanketed model atmospheres calculated using the BINARY2 code [28] and parameters close to those of UX CVn indicate slight variations in the atmospheric layers, with $\log \tau_R < 1$ when the He, O, and N abundances vary within 0.4 dex. Therefore, in our further studies, we used only blanketed Kurucz models [18] with solar chemical composition.

Our test calculations indicated that the effective

Table 2. Parameters of UX CVn

Component	Primary	Secondary
$P_{\rm orb}$, days	$0.573704^* \pm 0.000002$	
φ_0, JD	$2441096.177^* \pm 0.006$	
K, km/s	$-123.0^* \pm 3.4$	
γ, km/s	$-8.5^* \pm 2.8$	
e	$0.10^* \pm 0.03$	
ω	$349^{\circ *} \pm 14^\circ$	
q	1.15 ± 0.12	
$T_{\rm eff}$, K	$29\,700 \pm 300$	
$\log g$	4.13 ± 0.03	
$M/M_\odot$	0.45 ± 0.05	0.51 ± 0.01
$R/R_\odot$	0.95 ± 0.05	$\leq 0.011^{**}$
$A/R_\odot$	2.86 ± 0.09	
i	$85^\circ \pm 5^\circ$	
r, kpc	3.13 ± 0.15	

* Values from [12] are used.
** Estimate for models of [37] (see Section 4).

temperature of the star should be based primarily on the HeI/HeII ionization balance, since the HeII λ4686 Å line is sensitive to small variations in $T_{\rm eff}$. On the contrary, fitting of the observed and theoretical wing profiles for the Balmer lines was the best way to derive $\log g_1$.

It is not possible to determine the optical color indices of UX CVn based on photometric data alone, since the estimated accuracy of the color indices is about $0.^m02$ and they are insensitive to the atmospheric parameters of the primary. Therefore, we checked the atmospheric parameters using the observed color indices ($B{-}V = -0.29$, $U{-}B = -1.05$, $[Q] = -0.84$ [1], $u{-}b = -0.17$, $b{-}y = -0.12$, $m_1 = 0.08$ [30], $b{-}y = -0.11$, $m_1 = 0.08$, $c_1 = -0.09$, $[u{-}b] = -0.29$ [31]). The data were obtained at phases of maximum brightness of UX CVn, i.e., for the highest apparent surface temperature of the primary. We used the calibrations of [18] as theoretical color indices. Square brackets indicate color indices that are, to first approximation, independent of interstellar absorption, which is considered negligible for UX CVn [31].

We obtained the mean parameters for the atmosphere $T_{\rm eff} = 29\,700 \pm 300$ K, $\log g_1 = 4.13 \pm 0.03$, and $[{\rm He/H}] = 0.37 \pm 0.07$, and $V \sin i = 92 \pm 11$ km/s for the rotational velocity for the hydrogen lines. Figure 4 presents examples of the agreement between the theoretical and observed hydrogen line profiles; the helium abundances calculated from lines for different ionization stages are given in Table 3. The light curve of UX CVn calculated using the ROSHE code [4] yielded $T_{\rm eff} = 29\,900$ K and $\log g_1 = 4.13$ for the atmosphere of the primary at maximum brightness. The corrresponding theoretical color indices [18] ($B{-}V = -0.27$, $U{-}B = -1.03$, $[Q] = -0.83$, $u{-}b = -0.19$, $b{-}y = -0.12$, $m_1 = 0.07$, $c_1 = -0.10$, $[u{-}b] = -0.28$) are consistent with the observations within the probable errors $0.^m02$.

The difference between our effective temperature $T_{\rm eff} = 29\,700$ K and the values from the previous studies [19] ($T_{\rm eff} = 29\,250$ K) and [2] ($T_{\rm eff} = 28\,000$ K) is probably not due to random errors. When analyzing spectra of UX CVn acquired primarilly in 1952–1961, Greenstein [2] classified the primary as a B2 star, noting especially the absence of HeII lines. However, HeII λ4686 Å line is clearly visible in our spectra (Fig. 1b), and its equivalent width ($W_\lambda = 380$ mÅ) exceeds the detection threshold of [2] ($W_\lambda = 100$–150 mÅ) by an appreciable factor. SYNTH calculations for HeII λ4686 Å line profiles indicate that this line can decay to $W_\lambda = 150$ mÅ only if the effective temperature of the star decreases by at least 2000 K. The value $T_{\rm eff} = 29\,250 \pm 200$ K derived in [19] from observations made in the early 1990s suggests a gradual increase in the surface temperature of the UX CVn primary by 2000 K over the past 40 years, rather than short-term effective temperature fluctuations. In the stage immediately after the ejection of the comon envelope [9], the evolutionary tracks of subdwarf primaries in binary systems (with $M_1 = 0.40 M_\odot$, degenerate helium cores and thin hydrogen envelopes) display a rate of heating no higher than 400 K over 100 years. However, as is noted in [9], the duration of the high-luminosity phase of a subdwarf $t_{\rm H}$ depends strongly on the mass of the helium core $M_{\rm He}$ (as $t_{\rm H} \sim M_{\rm He}^{-11.6}$). Accordingly, the rate of heating of the UX CVn primary could reach values from 1000 K over 100 years for a mass of $M_1 = 0.43 M_\odot$ to 4000 K over 100 years for a mass of $M_1 = 0.47 M_\odot$. These estimates indicate that UX CVn may provide a unique means to test models for hot subdwarf evolution, and deserves further long-term monitoring.

Table 2 presents parameters for UX CVn derived from the iterative solution of the system of equations (2)–(5). The corrersponding theoretical light curve is plotted in Fig. 3b. These parameters differ from those collected in the reviews [29] and [7] by no more than 15–20%. An object with the characteristics of the primary ($\log L_1 - \log L_\odot = 2.82$, $\log T_{\rm eff} = 4.47$) is located in $\log L - \log T_{\rm eff}$ diagrams (see Fig. 14 in [9]) at the intersection of evolutionary tracks for subdwarfs with $M = 0.40 M_\odot$ and $M = 0.55 M_\odot$, consistent with our estimate $M_1 = 0.45 M_\odot$. The total

mass of the components is $M_1 + M_2 \approx 1.00 M_\odot$; in any case, it does not exceed the Chandrasekhar limit. Therefore, further evolution of the object cannot result in a type-I supernova. The distance to UX CVn, $r = 3.13$ Kpc, exceeds the estimate $r \approx 1.5$ Kpc suggested in [4] by only a factor of two, leaving the basic conclusion of the absence of a neutron star in the system unaffected.

4. ELEMENTAL ABUNDANCES IN THE ATMOSPHERE OF THE UX CVn PRIMARY

The high quality of the averaged spectrum of UX CVn makes it possible to determine quantitative abundances for most elements in the atmosphere of the hot subdwarf and analyze the evolution of the chemical composition in the system.

We determined the abundances of all elements by modeling theoretical line profiles using the SYNTH code and comparing these with the observed profiles. The calculation of the theoretical spectra is described in Section 3. The oscillator strengths for C, Mg, Al, and Si ions correspond to the results of [32] (the TOPBASE database); those for the other elements were taken from [18]. The microturbulence velocity $\xi_{\rm turb} = 3.0$ was determined from the requirement that the resulting nitrogen and oxygen abundances derived from the equivalent widths of the NII and OII lines be independent. For several ions, we took into account corrections for deviations from LTE in the NII and OII lines [33, 34] and the NIII lines [35]. For MgII and SiIV, we carried out independent non-LTE calculations using the NONLTE3 package [26] and 45-level and 39-level atomc models, respectively. Specific features of the non-LTE method used for these elements will be considered in a separate study.

Table 3 presents the resulting chemical composition, while Figs. 2b and 2c shows the dependences of the oxygen abundances on equivalent widths and excitation potentials for lower levels of the OII lines considered. The set of solar abundances is taken in accordance with [20].

Let us consider some particular elemental abundances in detail.

Helium. No substantial differences are observed between abundances derived from the triplet ($\log \varepsilon_{\rm He} = 11.39$) and singlet ($\log \varepsilon_{\rm He} = 11.36$) systems. The non-LTE corrections have different signs for different HeI lines; their amplitudes do not exceed $\Delta_{\text{non-LTE}} = 0.14$dex. In total, taking into account deviations from LTE increases the abundance by $\Delta_{\text{non-LTE}}({\rm He}) = 0.01$dex, with a negligible change in the dispersion.

Carbon. We derived abundances only from the strongest lines of both ionization stages. The value derived from the weakly-blended CII λ4267 Å doublet is more reliable. It was shown in [36] that the doublet lines have substantial, negative non-LTE corrections, which we did not take into account due to the small W_λ. In total, the absence of numerous CII lines in the interval $\Delta\lambda$4720–4850 Å fully confirms that $\log \varepsilon_{\rm c}$ is extremely low.

Nitrogen. We essentially derived $\log \varepsilon_{\rm N}$ from six weakly-blended NII lines. Taking into account non-LTE corrections for the NII lines [33] decreases $\log \varepsilon_{\rm N}$ by $\Delta_{\text{non-LTE}}({\rm N}) = -0.08$dex. The NIII λ4640 Å line displays substantial deviations from LTE $\Delta_{\text{non-LTE}}({\rm N}) = 0.38$dex [35], which were taken into account. We did not find any significant trends in the nitrogen abundances as a function of the equivalent widths, wavelengths, or excitation potentials of the lower levels of the lines studied.

Oxygen. The abundance of this element can be determined most reliably, due to the presence of 18 unblended OII lines. We can see from Figs. 2b, 2c that $\log \varepsilon_{\rm O}$ does not depend on the equivalent widths and excitation potentials of the lower levels of OII lines, confirming the correctness of our derived values $T_{\rm eff} = 29\,700K$ and $\xi_{\rm turb} = 3.0$. We also found systematic differences in the abundances ($\Delta \log \varepsilon_{\rm O} = 0.16$dex) calculated from lines in two spectral intervals $\Delta\lambda$3980–4500 Å and $\Delta\lambda$4500–5000 Å. This discrepancy is not eliminated when non-LTE corrections are taken into account [33], which decreases the average abundance by $\Delta_{\text{non-LTE}}({\rm O}) = -0.22$dex.

Neon. Our basic estimate $\log \varepsilon_{\rm Ne}$ was derived from the NeII λ4219 Å line. The calculated total profiles of the NeII λ4499 Å and OII λ4500 Å lines indicated good consistency between the theoretical and observed spectra for the adopted $\log \varepsilon_{\rm Ne}$ and $\log \varepsilon_{\rm O}$ values.

Magnesium. Only the common line of MgII λ4481 Å doublet is visible in the spectrum, blended with the AlIII λ4479 Å doublet. The total profile calculated for the solar abundance ratio indicates that the fraction of magnesium in the equivalent width is around 70%. Non-LTE corrections $\Delta_{\text{non-LTE}}({\rm Mg}) = -0.07$dex were applied to the magnesium abundance obtained under this assumption.

Aluminum. We determined $\log \varepsilon_{\rm Al}$ primarily using the AlIII λ4529 Å doublet, assuming that the nitrogen abundance derived from the NII λ4530 Å lines should be $\log \varepsilon_{\rm N} = 8.30$.

Silicon. For the SiIII lines, an obvious decrease in $\log \varepsilon_{\rm Si}$ can be seen when their equivalent widths decrease, probably due to neglected deviations from LTE. The most trustworthy abundance is $\log \varepsilon_{\rm Si} = 7.92$, derived from unblended lines of the SiIII λ4567, 4574 Å multiplet; this is consistent with

Table 3. Average elemental abundances $\log \varepsilon$ in the atmosphere of UX CVn and their dispersions σ (the number of lines used is given in parantheses.)

Element	$\log \varepsilon_\odot$	$\log \varepsilon_1 \pm \sigma$		$\log \varepsilon_2 \pm \sigma$	
He	11.00	HeI(12)*	11.37 ± 0.07	HeII(2)	11.36 ± 0.01
C	8.52	CII(1)	6.52	CIII(1)	6.71
N	8.01	NII(13)*	8.29 ± 0.08	NIII(2)*	8.31 ± 0.01
O	8.89	OII(24)*	8.72 ± 0.13		
Ne	8.05	NeII(2)	8.17 ± 0.02		
Mg	7.58	MgII(1)*	7.57		
Al	6.43	AlIII(2)	6.47 ± 0.04		
Si	7.51	SiIII(4)	7.86 ± 0.11	SiIV(1)*	7.91
S	7.17	SIII(2)	≈ 6.80		
Fe	7.51	FeIII(3)	< 6.20	FeIV(1)	< 6.50

* Deviations from LTE have been taken into account (see Section 4).

the results for the SiIV λ4631 Å line, for which we took into account non-LTE corrections.

Sulphur. We estimated $\log \varepsilon_S$ only from the SIII λ4365 Å line under the assumption that the oxygen abundance from OII λ4366 Å line was $\log \varepsilon_O = 8.80$.

Iron. We did not detect any FeIII or FeIV lines in the spectrum, including the FeIII λ4165 Å found in [11]. The upper limits for the Fe abundances in Table 3 were calculated for the strongest lines of both ionization stages, assuming that the detection limit for the lines in our spectra is $W_\lambda \approx 20$ mÅ.

The elemental abundances in the atmosphere of the UX CVn primary indicate that several factors affected its formation. The low iron abundance confirms that the system belongs to the old halo population [1, 4]. This is consistent with the distance to UX CVn, $r = 3.13$ kpc, which is essentially the object's height above the Galactic plane. According to evolutionary models of binary systems that undergo a common envelope stage [9], hot subdwarfs with masses $M = 0.45 M_\odot$ can be formed from stars with initial masses $M = 1.40 M_\odot$, which is also consistent with the idea that UX CVn is a Galactic halo object.

The abundances of the other elements show signs that material has been ejected into the atmosphere of the subdwarf and reprocessed in the course of two types of nuclear reactions: the carbon–nitrogen cycle (the He and N excess and strong deficit of C) and the α process and burning of light elements (the Si excess and solar abundances for Ne, Mg, and Al). The abundance ratios for CNO-group elements suggest that the influence of the carbon–nitrogen cycle reactions began after the initial enrichment of the atmosphere in all heavy elements, including Si and S. Therefore, we propose the following hypothesis for the chemical evolution of the atmosphere of the primary.

(1) The first stage of enrichment in heavy elements occurred during the transformation of the secondary into a supergiant, with filling of its Roche lobe and accretion onto the primary. The observed silicon excess and sulphur underabundance indicate that nuclear synthesis in the secondary continued up to the stage of α-process reactions, burning of light elements (^{12}C, ^{16}O), and ^{24}Mg and ^{28}Si synthesis in the core or a layer source. Material enriched with nuclear-synthesis products was ejected to the surface and accreted onto the primary, altering its initial chemical composition.

(2) Further variations of the chemical composition occurred after the evolution of the visible component on the main sequence and its transition to the region of giants and supergiants. The carbon–nitrogen cycle of hydrogen burning brought about the repeated reprocessing of CNO elements and helium synthesis, until the current abundance ratios were established.

In this picture, silicon should dominate in the core of the white dwarf. The estimate of its radius presented in Table 3 was derived from models of white dwarfs [37] with magnesium-silicon cores and an effective temperature of $T_{\rm eff} \leq 10\,000$ K.

5. CONCLUSION

A comparison between the derived parameters of the primary and evolutionary tracks from [9] indicates that the stage of UX CVn's evolution beginning from the ejection of the common envelope is one of the

shortest known among close binaries. The low gravitation and relatively large radius of the hot subdwarf result in considerable asphericity, making it easier to estimate parameters of the system. However, the review [14] and subsequent studies include at least six young systems with orbital periods shorter than one day and containing hot subdwarfs with $\log g < 5.6$, for which the effects of asphericity can be used when determining the system parameters. Numerous lines of heavy elements should be observed in the spectra of such subdwarfs, suitable for analyses of the atmospheric chemical compositions of stars that have undergone a common envelope stage twice. The fruitfulness and practical importance of our current study is illustrated by the following results we have obtained for UX CVn.

(1) The radius of the primary component of UX CVn $R_1 = 0.95R_\odot$ does not exceed its Roche-lobe radius $R_1 = 1.03R_\odot$ within the error $\Delta R_1 = 0.05R_\odot$, so the system is currently completely detached.

(2) We have detected the HeII λ4686 Å line in the spectrum of UX CVn, probably indicating an increase in the surface temperature of the primary by 2000 K over 40 years. Overall, this rate of temperature increase is consistent with theoretical predictions based on evolutionary models for hot subdwarfs in close binaries after ejection of the common envelope [9]. The corresponding variation of the radius of the hot subdwarf does not exceed 3–4%, consistent with our conclusion that the system has been completely detached over the entire period during which it has been observed.

(3) The total mass of the UX CVn components is close to that of the Sun; further evolution of the system cannot result in a type-I supernova.

(4) The absence of iron lines confirms that UX CVn is a member of Population II (a halo object).

(5) The current abundance of heavy elements in the atmosphere of the UX CVn hot subdwarf indicates that mixing and mass exchange between the components at the common envelope phase has had an appreciable influence on the chemical evolution of their atmospheres.

6. ACKNOWLEDGMENTS

The author is grateful to N.A. Sakhibullin, N.V. Borisov, and E.V. Lapina for their comprehensive help in the data reduction and modeling, and also to I.F. Bikmayev, V.F. Suleimanov, and L.I. Mashonkina for useful discussions and numerous comments. Our spectroscopic observations were made possible by support from the Large Telescopes Program Committee (LTPC) and the staff of the Special Astrophysical Observatory of the Russian Academy of Sciences. This work was supported by the Russian Foundation for Basic Research (project no. 99-02-17488).

REFERENCES

1. A. Young, B. Nelson, and R. Mielbrecht, Astrophys. J. **174**, 27 (1972).
2. J. L. Greenstein, Astron. Astrophys. **23**, 1 (1973).
3. D. Schonberner, Astron. Astrophys. **70**, 451 (1978).
4. A. Young and S. T. Wentworth, Publ. Astron. Soc. Pac. **94**, 815 (1982).
5. H. Ritter, Astron. Astrophys. **169**, 139 (1986).
6. M. de Kool and H. Ritter, Astron. Astrophys. **267**, 397 (1993).
7. A. M. Cherepashchuk, N. A. Katysheva, T. S. Khruzina, and S. Y. Shugarov, *Highly Evolved Close Binary Stars: Catalog* (Gordon and Breach, Brussels, 1996), Part 1.
8. I. J. Iben and M. Livio, Publ. Astron. Soc. Pac. **105**, 1375 (1993).
9. I. J. Iben and A. Tutukov, Astrophys. J. **418**, 343 (1993).
10. J. V. Bixler, S. Bowyer, and M. Laget, Astron. Astrophys. **250**, 370 (1991).
11. N. C. Hambly, W. R. J. Rolleston, F. P. Keenan, *et al.*, Astrophys. J., Suppl. Ser. **111**, 419 (1997).
12. V. V. Shimanskiĭ, N. V. Borisov, N. A. Sakhibullin, *et al.*, Astron. Zh. (in press)
13. R. Mochkovitch and M. Livio, Astron. Astrophys. **236**, 378 (1990).
14. R. A. Saffer, M. Livio, and L. R. Yungelson, Astrophys. J. **502**, 394 (1998).
15. C. Koen, J. A. Orosz, and R. A. Wade, Mon. Not. R. Astron. Soc. **300**, 695 (1998).
16. V. L. Afanas'ev, V. A. Lipovetskiĭ, V. P. Mikhaĭlov, *et al.*, Astrofiz. Issled. Spets. Astron. Obs. Akad. Nauk **31**, 128 (1991).
17. P. Ballester, in *4th ESO/ST-ECF Data Analysis Workshop, 1992,* p. 177.
18. R. L. Kurucz, SAO CD-Roms (Cambridge MA02138, 1994).
19. R. A. Saffer, F. P. Keenan, N. C. Hambly, *et al.*, Astrophys. J. **491**, 172 (1997).
20. E. Anders and N. Grevesse, Geochim. Cosmochim. Acta **53**, 197 (1989).
21. C. R. Vidal, J. Cooper, and E. W. Smith, Astrophys. J., Suppl. Ser. **25**, 37 (1973).
22. A. J. Barnard, J. Cooper, and L. J. Shamey, Astron. Astrophys. **1**, 28 (1969).
23. D. Mihalas, A. J. Barnard, J. Cooper, and E. W. Smith, Astrophys. J. **190**, 315 (1974).
24. R. L. Kurucz and I. Furenlid, SAO Spec. Rep. **387**, 1 (1979).
25. N. A. Sakhibullin and V. Ya. Shabert, Pis'ma Astron. Zh. **16**, 539 (1990) [Sov. Astron. Lett. **16**, 231 (1990)].
26. N. A. Sakhibullin, Tr. Kazan. Gor. Astron. Obs. **48**, 9 (1983).
27. L. H. Auer and J. Heasley, Astrophys. J. **205**, 165 (1976).

28. N. A. Sakhibullin and V. V. Shimanskiĭ, Astron. Zh. **73**, 793 (1996) [Astron. Rep. **40**, 723 (1996)].
29. H. Ritter and U. Kolb, Astron. Astrophys., Suppl. Ser. **129**, 83 (1998).
30. F. Wesemael, G. Fontaine, P. Bergeron, *et al.*, Astron. J. **104**, 203 (1992).
31. D. Kilkenny, Mon. Not. R. Astron. Soc. **181**, 611 (1977).
32. M. J. Seaton, C. J. Zeippen, J. A. Tully, *et al.*, Rev. Mex. Astron. Astrofis. **23**, 19 (1992).
33. S. M. Andrievsky, S. A. Korotin, R. E. Luck, and L. Yu. Kostynchuk, Astron. Astrophys. **350**, 598 (1999).
34. S. A. Korotin, S. M. Andrievsky, and R. E. Luck, Astron. Astrophys. **351**, 16 (1999).
35. L. I. Solov'eva, Astron. Zh. **63**, 310 (1986) [Sov. Astron. **30**, 189 (1986)].
36. N. A. Sakhibullin, Astron. Zh. **64**, 291 (1987) [Sov. Astron. **31**, 151 (1987)].
37. L. Girardi, A. Bressan, G. Bertelli, and C. Chiosi, Astron. Astrophys., Suppl. Ser. **141**, 371 (2000).

Translated by K. Maslennikov

Astronomy Reports, Vol. 46, No. 2, 2002, pp. 139–151. Translated from Astronomicheskiĭ Zhurnal, Vol. 79, No. 2, 2002, pp. 158–171.

Evolutionary Changes in the Optical Spectrum of the Peculiar Supergiant IRC+10420

V. G. Klochkova, M. V. Yushkin, E. L. Chentsov, and V. E. Panchuk

Special Astrophysical Observatory, Russian Academy of Sciences, Nizhniĭ Arkhyz, Karachai-Cherkessian Republic, 357147 Russia

Received March 19, 2001

Abstract—We present new spectroscopic observations of the peculiar supergiant IRC+10420. In 1997–2000, we obtained three high signal-to-noise ratio spectra of the object at 4300–8000 Å with a spectral resolution of 15 000 (20 km/s) using the 6-m telescope of the Special Astrophysical Observatory. From our 2000 spectrum, we estimate the spectral type of IRC+10420 to be A2, corresponding to a temperature of ~ 9200 K. Many emission lines were detected, identified with lines of Fe I; Fe II, Ti II, Cr II, and Sc II ions; and [O I], [Fe II], and [Ca II] forbidden lines. The radial velocity derived from absorption lines without obvious emission components (He I λ5876, O I, N I, Si II) and from absorption components of the Balmer lines is 93 ± 1 km/s. The redshift of photospheric lines relative to the star's center-of-mass velocity is interpreted as a consequence of scattering in the expanding, optically thick dust envelope. Both emission and absorption lines show a correlation between radial velocity and oscillator strength. We found variability in the relative intensities of the H_α and H_β emission components. We conclude that IRC+10420 is rapidly evolving towards a Wolf–Rayet stage; the current rate of the photospheric temperature increase is ~ 120 K per year. Based on the intensity of the O I (λ7773) triplet, we estimate the star's luminosity to be $M_{\rm bol} = -9.5^m$. In all 1997–2000 spectra of IRC+10420, the He I λ5876 line has a significant equivalent width of at least 200 mÅ; this may be possible in the presence of such a low temperature due to the star's high luminosity and the enhanced helium abundance in the supergiant's atmosphere.

1. INTRODUCTION

The source IRC+10420 is one of the most enigmatic stellar objects of the northern sky. In is among the brightest objects in the far infrared and was already detected in the earliest surveys. Based on a photographic spectrogram with resolution $R = 1000$ and the intensity of the IR oxygen triplet, Humphreys *et al.* [1] estimated the spectral type and luminosity class of IRC+10420 to be F8–G0 and Ia. The spectral energy distribution was very similar to that of η Carinae over a wide wavelength range (0.5–20 μm); the optical spectrum of IRC+10420 resembled that observed for η Carinae (cF5) in 1892 three years before it began to display emission lines. Assuming that the luminosities of IRC+10420 and η Carinae are the same, Humphreys *et al.* [1] estimated the distance to IRC+10420 to be 4–6 kpc. However, already in 1976, differences between IRC+10420 and η Carinae were noted in an analysis of their photometric histories and broad-band polarimetric data [2].

Interest in IRC+10420 increased when OH maser emission was discovered [3]; previously, the hottest maser sources had been classified as M3 stars. The kinematic distance was estimated to be 6.8 kpc in a classical interpretation of the two-peak OH spectrum. This led to the luminosity estimate $M_V < -9.4^m$, unusually high for an F8I star. To explain the presence of maser sources around an object that hot, it was suggested that a powerful gas and dust envelope had formed during the M-supergiant phase, with the subsequent rapid evolution of IRC+10420 to the left in the Hertzsprung–Russell (HR) diagram [4]. This proposed spectral evolution was confirmed much later in observations with high spectral resolution [5, 6].

Between 1972 and 1986, the object developed strong emission in H_α [7, 8].

In an attempt to reconcile the radial velocities obtained at moderate spectral resolution in the red with the results of radio observations in OH lines, Fix [7] suggested a model with an optically thick, expanding dust envelope; repeated scattering in the envelope increases the fraction of redshifted photons. The resulting lower limit on the envelope's angular size (0.7″ for a distance of 6 kpc) was later exceeded by the size of structures revealed in photographs in polarized light [9].

1063-7729/02/4602-0139$22.00

Table 1. Log of observations of IRC+10420

Spectrum No.	Integration time, s	Range, Å	S/N	Date
s16607	2×3200	4400–8000	≤ 300	May 19, 1997
s24212	2×1800	4550–7900	≤ 270	July 3, 1999
s27520	2×3200	4300–7900	≤ 300	April 26, 2000

We will consider two hypotheses concerning the evolutionary status of IRC+10420. In the first, IRC+10420 is in a protoplanetary nebula (PPN) phase [10, 11]. Indeed, the source possesses the main observational properties of PPN candidates [12].

(1) An IR excess produced by a circumstellar dust envelope is present.

(2) The regime for outflow from its surface has apparently changed so that the large-scale mass loss that was present in the past no longer occurs [11].

(3) The high-luminosity (Ia) object has spectral types in the range B–G. Spectral type variations can also be relatively rapid for PPNs [13, 14].

(4) The object has not displayed large-amplitude photometric variability, since its brightness increased by one magnitude between 1925 and 1975 [15].

Based on broad-band polarimetry and improved radial velocities, Jones *et al.* [9] also concluded that IRC+10420 was fairly distant. Comparing the interstellar polarization and interstellar absorption for IRC+10420 and surrounding stars, they estimated the distance to be 4–6 kpc, corresponding to $M_{\rm bol} = -9.1^m$–(-10.0^m). As noted in [16], with such a high luminosity (about $10^6 L_\odot$), the object appears on an evolutionary track for stars with masses of $20 - 40 M_\odot$. This luminosity estimate forms the basis for the second hypothesis about the nature of IRC+10420: the star is in transition between being an OH/IR supergiant and a Wolf–Rayet star. Stars evolve very rapidly in this part of the HR diagram, so IRC+10420 provides a unique chance to observe the corresponding evolutionary phase of massive stars.

The upper limit for the luminosity of a PPN is $10^4 L_\odot$. The interstellar and circumstellar absorption determined from the color excess, $E(B-V) = 2.2^m$, is $A_V \approx 6^m$–7^m. Were IRC+10420 a protoplanetary nebula, its maximum distance would be only $\sim$600 pc, in contradiction with the pattern of the interstellar polarization, the observed radial velocity, and the intensities of interstellar sodium lines [9].

Thus, the most urgent tasks for determining the evolutionary status of IRC+10420 are to monitor spectral changes, develop models for the envelope, and estimate the object's distance and luminosity.

The aim of the current study was to improve our knowledge of the spectral type and rate of evolution of the optical spectrum of IRC+10420. To accurately determine the spectral type, it is important to obtain spectra over a wide wavelength range covering wavelengths as short as possible, where the contribution of the circumstellar envelope's gas is lower and photospheric absorption lines are not distorted by the envelope emission. Our radial-velocity measurements for numerous spectral features formed in the stellar photosphere and the circumstellar envelope have made it possible to distinguish patterns in the behavior of lines formed by the dynamics of the circumstellar matter. In turn, this can provide an empirical basis for detailed modeling.

2. OBSERVATIONS AND REDUCTION

Our observations were obtained on the 6-m telescope of the Special Astrophysical Observatory (Russian Academy of Sciences). We used the PFES prime-focus echelle spectrograph [17] with a 1040×1170-pixel CCD detector. The spectra covered the range 4300–8000 Å with a resolution of $\lambda/\Delta\lambda \sim 15\,000$ (20 km/s). We selected three spectra with high signal-to-noise (S/N) ratios from the spectrograms obtained from May 1997 to April 2000. An observation log is presented in Table 1. To facilitate classification of the spectra of IRC+10420, we obtained spectra of bright A–F high-luminosity stars with the same instrument; we use the spectrum of α Cygni (A2Ia) here. When removing cosmic-ray traces, we performed a median averaging of pairs of spectra obtained at adjacent times. We used the spectrum of a hollow-cathode Th–Ar lamp for the wavelength calibration. To remove the telluric absorption spectrum, we recorded the spectrum of the hot, rapidly rotating star HR 4687, which has no intrinsic narrow lines, on each night.

We used the ECHELLE programs in the MIDAS (98NOV) system in the preliminary reduction of the CCD echelle spectra (removal of cosmic rays, background subtraction, wavelength calibration, extraction of the spectral orders). The final spectral reduction (normalization to the continuum, measurements of radial velocities and equivalent widths for the spectral lines) was done using the DECH20 package [18].

3. THE SPECTRUM OF IRC+10420

We identified spectral features using the line lists of [5, 6]. Improved line wavelengths, oscillator strengths, and excitation potentials were taken from the VALD atomic-line database [19]. An atlas of the spectrum taken in 1997 can be found in [20].

3.1. Profiles of Lines of Light Elements and Metals

Emission and absorption lines from metal ions (Fe II, Ti II, Sc II, Cr II), emission lines of Fe I, and absorption lines of N I, O I, and Si II dominate the optical spectrum of IRC+10420. Some emission features can be identified with forbidden [Fe II], [Ca II], and [O I] lines. The profiles of metal-ion lines are varied, from nearly symmetrical emission lines to inverse P Cygni profiles and absorption profiles with two emission components (Fig. 1). The N I, O I, and Si II lines show almost symmetrical absorption profiles (the centers of these line profiles are shifted by, on average, 5 km/s toward the red relative to the profile minima).

The He I λ5876 line (Fig. 2) is present in all spectra of IRC+10420 taken in 1997–2000, as well as in earlier spectra [5]. The equivalent width of this line remained virtually the same ($W_\lambda \approx 200$ mÅ) during the entire period covered by our observations.

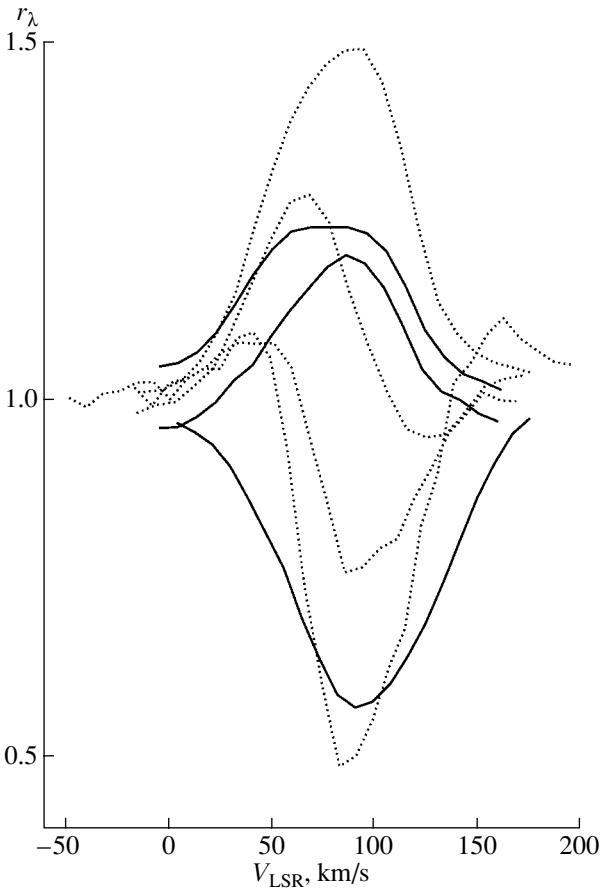

Fig. 1. Line profiles in the optical spectrum of IRC+10420. From top to bottom, the dashed curves are Fe II(46) λ5992, Fe II(74) λ6457, Ti II(70) λ5227, and Fe II(42) λ4924; the solid curves are Fe II(73) λ7516, [O I](1F) λ6300, and Si II(2) λ6347.

3.2. Spectral Type

After the first spectral-type determination for IRC+10420 in 1972 (F8–G0 [1]), there were no serious attempts to refine the object's spectral type for 20 years. Based on low-resolution 1.2–2.5 μm IR spectra, Thompson and Boroson [21] concluded that the intensities of the Brackett absorption lines in 1976 corresponded to a spectral type of F8 Ia (with uncertainty due to the lack of IR observations for a sufficient number of stars with similar subtypes). Fix [7] remarked that, in an optical spectrum of IRC+10420 taken in 1980 at 5000–8000 Å with a reciprocal linear dispersion of 60 Å/mm, nearly all the photospheric absorption lines appeared weaker than those in the comparison star, γ Cygni (F8Ib). Using quantitative criteria developed for high-resolution echelle spectra, Klochkova *et al.* [5] estimated the spectral type of IRC+10420 to be A5 based on spectra taken in 1992–1996. Taking into account the observations of Humphreys *et al.* [1], Klochkova *et al.* [5] concluded that the star's photospheric temperature increased by more than 2000 K in less than 25 years. This led us to continue our photometric monitoring of the object.

Most absorption lines in the wavelength range studied have emission components in their wings, making it difficult to determine the temperature using model atmospheres. To estimate the spectral type of IRC+10420, we used relations between the equivalent widths of selected lines and spectral type derived from the spectra of normal supergiants [22, 23], selecting lines with no obvious emission components. The results are collected in Table 2.

The scatter of these spectral-type estimates is large, from B8 to A6, but we can see that the spectral types derived from Fe II lines are typically A0–A1, while those from Ti II lines are A4–A5. To estimate the photospheric temperature of IRC+10420, we used the spectral-type–temperature relation for Ia supergiants from [24]. The spectral type derived from Fe II lines corresponds to a temperature of $\sim$ 9600 K, while that derived from Ti II lines corresponds to $\sim$ 8300 K. The latter value is even lower than the temperature derived in [5] based on model atmosphere calculations. However, we can see in Fig. 3 that the spectrum of IRC+10420 is in satisfactory agreement

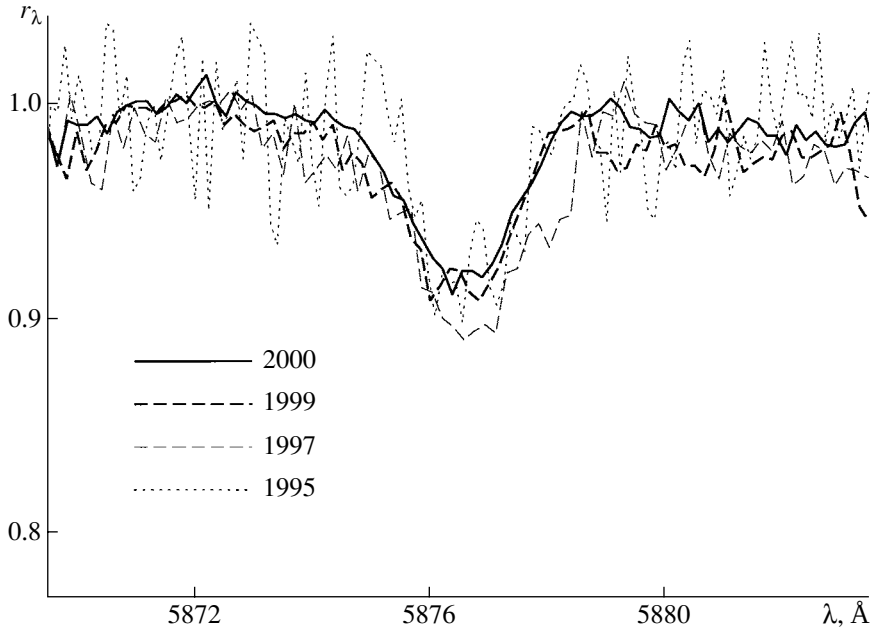

Fig. 2. He I λ5876 line profiles for IRC+10420 observed at different times.

with that of α Cygni. The Fe II, Cr II, and Si II absorption lines in the spectra of the two stars are virtually identical; one exception is the Ti II lines, which are considerably deeper in the spectrum of IRC+10420. On average, we estimate the spectral type of IRC+10420 based on our 2000 spectrum to be A2, corresponding to a temperature of $\sim$ 9200 K. Thus, the star's temperature increased by more than 3000 K within 27 years. Below, we will use 120 K/year as an estimate of the rate of change of the photospheric temperature.

3.3. Luminosity

The main source of uncertainty in stellar luminosity estimates derived from photometric observations are uncertainties in the object's distance and the interstellar absorption. Estimated distances for IRC+10420 are between 3.4 kpc [4] and 6.8 kpc [3]. The interstellar absorption derived from multicolor photometry [2] and polarimetric observations [9] is $A_V = 6^m$–7^m. Various luminosity estimates for IRC+10420 presented in the literature are in the range $M_{\rm bol} = -8^m$–(-10^m).

Table 2. Spectral type of IRC+10420 in 2000 from dependences of equivalent widths on spectral type

Line	W_λ, mÅ	Spectral type
Fe II λ4352 Å	490	A1
Fe II λ4385 Å	400	B9–A1
Fe II λ4417 Å	470	A1
Ti II λ4444 Å	590	A5
Ti II λ4469 Å	560	A3–A6
Mg II λ4481 Å	600	B8–A0
Fe II λ4584 Å	490	A0–A2

Luminosity determinations based on spectroscopic criteria are free from the drawbacks noted above. It is well known that the intensity of the O I λ7773 IR triplet is correlated with luminosity [25]. The equivalent width of the O I λ7773 triplet in the spectrum of IRC+10420 is 2.8 Å, exceeding values for all other known stars. In [25], the relation between the absolute magnitude M_v and the equivalent width of the oxygen triplet W(O I) was approximated with a second-order polynomial in W(O I), leading to unrealistic growth of the luminosity with increasing intensity of the oxygen triplet for W(O I) > 2.3 Å. Therefore, we plotted a new calibration curve (Fig. 4) using the $M_{\rm bol}$ and W(O I) values for selected stars from [25–29]. We approximated the W(OI)–$M_{\rm bol}$ relation with an exponential law (dashed curve in Fig. 4). According to this relation, an O I λ7773 triplet equivalent width of W(O I)= 2.8 Å corresponds to an absolute magnitude of $M_{\rm bol} = -9.5^m$. Note that we should also take into account the dependence of the triplet equivalent width on temperature in order to estimate the stellar luminosity more correctly. With this in mind, we plotted a second calibration curve using a sample of stars with spectral types

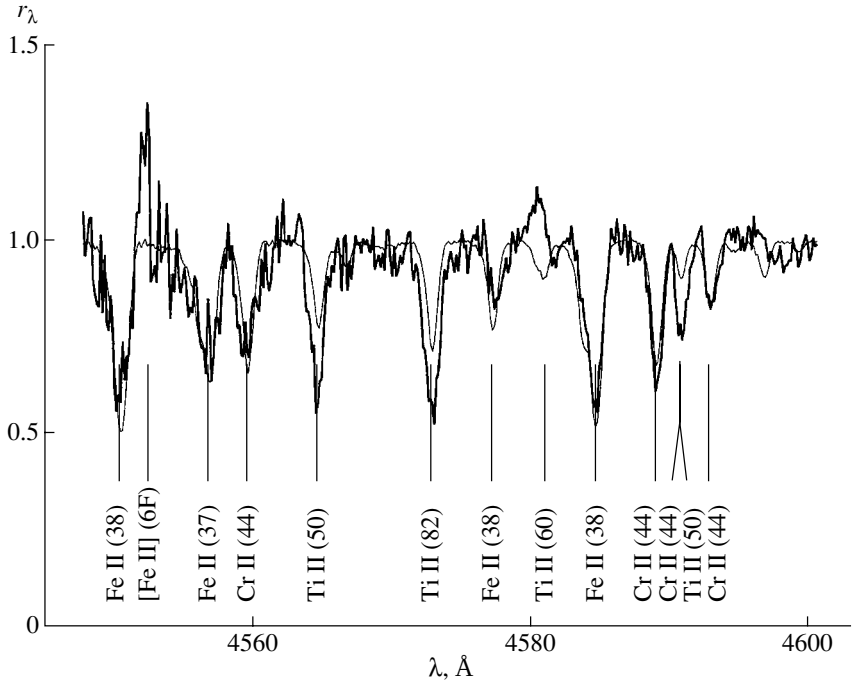

Fig. 3. Comparison of the spectra of IRC+10420 (spectrum s27520; thick curve) and α Cygni (thin curve). The agreement of the Fe II and Cr II line profiles is good, but the Ti II lines are much deeper in the spectrum of IRC+10420.

from A0 to F0 (solid curve in Fig. 4). The small number of measurements prevents us from plotting a two-dimensional dependence of W(O I) on $M_{\rm bol}$ and $T_{\rm eff}$. According to the new calibration curve, the absolute magnitude of IRC+10420 is $M_{\rm bol} = -9.1^m$. It was shown in [30] that the intensity of the O I λ7773 triplet increased steadily with decreasing effective temperature for early to late A stars, then began to decrease steadily after type F0. Our 2000 spectrum of IRC+10420 corresponded to spectral type A2, and we adopt $M_{\rm bol} = -9.1^m$ as a lower limit for the luminosity of IRC+10420. Thus, the absolute magnitude of IRC+10420 estimated using spectroscopic criteria is $M_{\rm bol} = -9.5^m \pm 0.4^m$.

3.4. Hydrogen lines

No H_α emission was noted in the 1972 low-resolution spectrum of IRC+10420 [1]. However, as early as November 1972, Herbig noted weak emission wings of H_α and the Ca II infrared triplet in a higher resolution ($R = 10\,000$) spectrogram (reported by Irvine [8]). The Brackett series was observed in absorption in 1984 [10]. By July 1986, H_α could be readily detected in low-resolution spectra, and, Herbig found inverted central peaks of the H_α and Ca II emission lines using a Coudé spectrogram in late 1986 [8]. Therefore, we suggest that the intense development of the H_α emission profile accompanied rapid evolution of the photospheric absorption spectrum (see below). Based on the two-peaked H_α emission and low-resolution spectra, Jones *et al.* [9] suggested that the star was surrounded with a rotating disk.

The wavelength interval covered using the CCD detector in an individual echelle order near H_α is ~200 Å. We selected the position of the frame so that

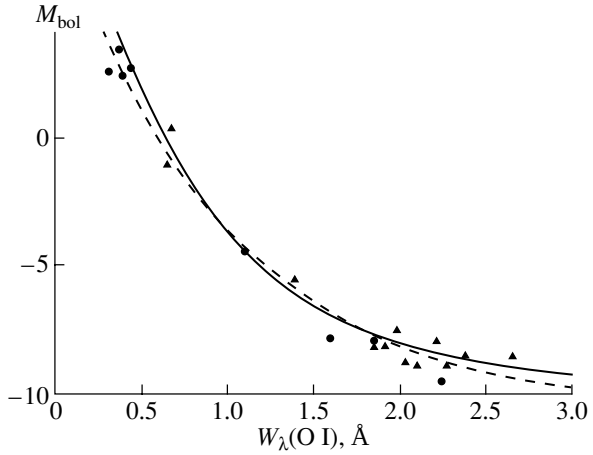

Fig. 4. Relation between the equivalent width of the λ7773 oxygen triplet W(O I) and absolute magnitude $M_{\rm bol}$. The circles are F5–G0 stars, and the triangles, A0–F0 stars. The solid curve is the W(O I)–$M_{\rm bol}$ relation for A0–F0 stars approximated with an exponential law; the dashed curve is the relation derived from all the stars.

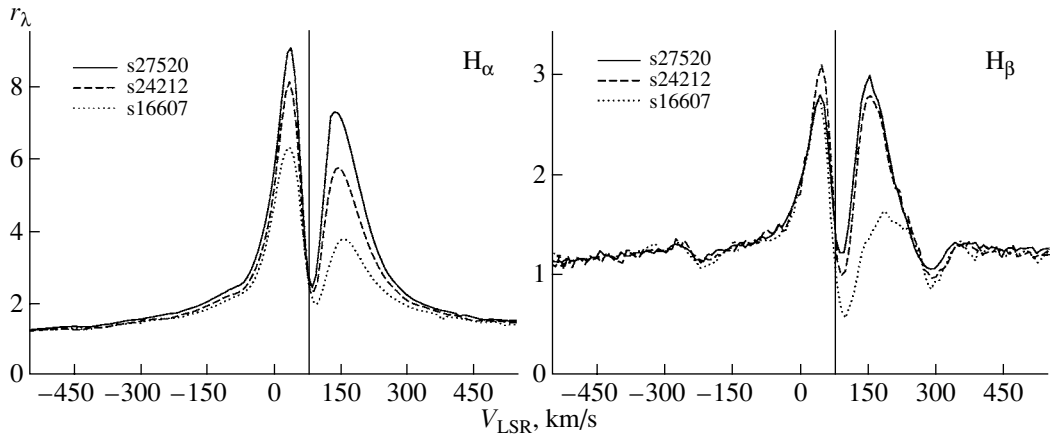

Fig. 5. Hydrogen line profiles in the optical spectrum of IRC+10420 at different epochs. The intensities of both components of H_α grow steadily with time; the intensity of the redshifted H_β component also grows steadily, whereas the intensity of the blueshifted H_β fluctuates about its mean value.

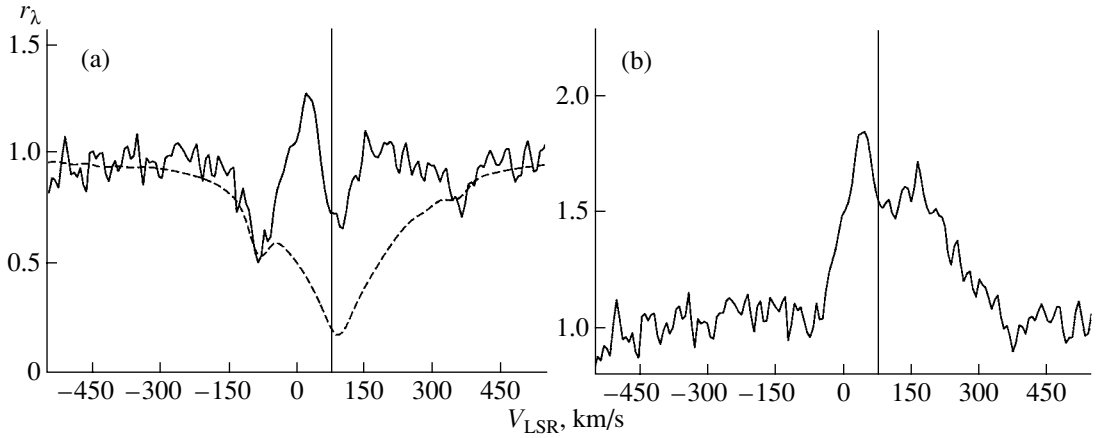

Fig. 6. (a) Profile of the H_γ line in the optical spectrum of IRC+10420. The dashed curve is the absorption profile computed using Kurucz's model grid [31]. (b) The redshifted emission component can be seen more clearly after subtracting the photospheric component from the observed H_γ profile.

the hydrogen lines were as close to the middle of the frame as possible. The broad hydrogen-line emission wings observed in our echelle spectra, which are due to scattering on free electrons, impose limitations on the accuracy with which the continuum level can be traced in the orders containing these lines. The wings of the H_α lines can be followed to velocities of $\pm$1500 km/s. When determining the continuum level, we took into account information on the adjacent echelle orders; the energy distributions in echelle spectra change gradually from one order to another.

The H_α and H_β lines show complex two-peaked profiles, with maximum intensities corresponding to radial velocities of 40 and 145 km/s and a minimum at 90 km/s (Fig. 5; here and below, we present values relative to the local standard of rest, LSR). Since the broad photospheric absorption is completely filled in by emission, the observed profiles can have such a shape in two cases: when a narrow envelope absorption line is superposed on a broad envelope emission line and when two narrower emission lines with different radial velocities are combined. In the latter case, the inner wings will have a gentler slope than the outer wings. In our case, the intensities of the emission wings facing each other fall off faster than the intensities of the outer wings so that these components are separated by an absorption component. A combination of both cases is also possible.

The redshifted H_γ emission component can be clearly distinguished after subtracting the absorption profile (Fig. 6). The velocity of the blue and red maxima are 25 and 150 km/s, and the velocity of the

Table 3. Relative intensities of hydrogen-line emission components and their ratios in the spectrum of IRC+10420*

Date	$T_{\rm eff}$, K	H^b_α	H^r_α	H^b_α/H^r_α	H^b_β	H^r_β	H^b_β/H^r_β	H^b_γ	H^r_γ	H^b_γ/H^r_γ
July 1993	8200	6.35	2.97	2.138	1.33	1.03	1.291			
Sept. 1995	8500	12.80	7.55	1.695	2.69	1.93	1.394			
March 1996	8550	7.87	5.06	1.555						
May 1996	8600	7.33	4.18	1.754						
Apr. 1997	8750	5.68	3.16	1.797	2.23	1.11	2.010			
July 1997	8800	6.31	2.98	2.161						
May 1999	9050	7.43	5.10	1.457	2.49	2.18	1.142			
March 2000	9200	8.36	6.61	1.265	2.10	2.31	0.909	0.84	0.70	1.200

* The superscripts b and r mean blueshifted and redshifted components, respectively.

minimum is 93 km/s. For the H_α and H_β lines, the effect of the photospheric absorption wing is rather small due to the large intensities of the envelope components.

To better distinguish the envelope components of the hydrogen lines, we subtracted the spectrum of α Cygni, a star with similar parameters, from the 2000 spectrum of IRC+10420. Since an emission component is present in the H_α line of α Cygni, we subtracted a synthetic spectrum for a supergiant with $T_{\rm eff} = 9200$ K and solar abundances computed using Kurucz's model grid [31]. After approximately taking into account the photospheric contribution in this way, the velocity of the H_γ envelope component in the spectrum of IRC+10420 became as high as 35 km/s. At the other epochs, the intensities of hydrogen envelope components were obtained by subtracting a photospheric absorption spectrum computed for the temperature of IRC+10420 interpolated for the epoch of the observation. The line intensities for 1993 were taken from [6], and the remaining values were derived from the results of [5, 20] and the present study. Table 3 presents the intensities of the hydrogen envelope components in units of the continuum intensity and their ratios for all our epochs. Note that using low-resolution spectra can only confuse the picture, since the intensity ratios of emission peaks depend strongly on the width of the spectrograph's instrumental profile. For example, the ratio of the blue and red H_α peaks in the spectrum of June 29, 1993, with a resolution of $R = 4000$, was 1.66 [32], whereas the echelle measurements taken one month later gave the value 1.97 (cf. Table 3).

To estimate the flux ratios in corresponding components of the H_α, H_β, and H_γ lines in units of the continuum level (Table 3), we re-normalize taking into account the reddening-corrected observed energy distributions [16]. We obtained for the emission components for our 2000 spectrum of IRC+10420 (with some uncertainty due to the evolution of the continuum since the observations of [32]) $H^b_\alpha/H^b_\beta/H^b_\gamma = 2.2/1.0/0.4$ for the blueshifted components, and $H^r_\alpha/H^r_\beta/H^r_\gamma = 1.7/1.0/0.3$ for the redshifted components. These ratios are close to those for a recombination approximation, 3.0/1.0/0.4 [33]; i.e., the emitting medium is optically thin in the corresponding transitions.

Figure 5 shows the H_α and H_β line profiles for different observation epochs. We can see that both H_α emission peaks grow steadily with time, whereas H^b_α/H^r_α decreases. H^b_β/H^r_β also decreases, but the temporal behavior of the two components is different: the red component's intensity gradually increases, while the intensity of the blue component fluctuates within ± 0.2 of the continuum intensity. There was apparently a maximum of the hydrogen-line intensity in the second half of 1995, with a subsequent abrupt decrease; there was a minimum in mid-1997, and the last spectra show a gradual increase in the H_α and H_β intensities. Overall, the pattern of the component intensity variations are not consistent with the suggestion of Jones *et al.* [9] that the Balmer lines are formed in a rotating disk.

The Brackett hydrogen lines were observed in absorption in 1976 [21] and 1984 [10]. In the 1984 observations, Br11 was a pure absorption line [10]; in observations made in 1992, the core of the Br12 line was somewhat filled with emission, and strong blueshifted emission was seen in lower members of the Brackett and Pfundt series [32]. The detection of emission in H_α by Herbig [8] and in the lower members of the Brackett series by Oudmaijer *et al.* [32] was separated by a considerable time interval. The difference in the spectral resolutions of the Coudé specrtogram used in Herbig's observations in 1972 and the IR spectra of Oudmaijer *et al.* obtained in

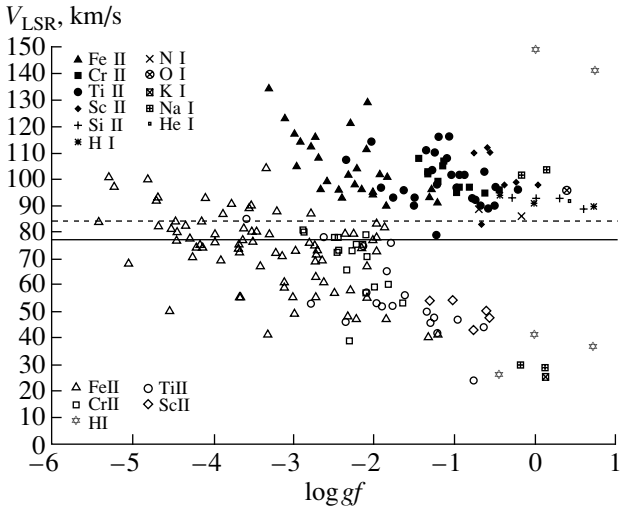

Fig. 7. Correlation between the radial velocities of lines and their oscillator strengths. Open symbols correspond to emission components, and the filled symbols, crosses, and asterisks to absorption components. The solid line shows the systemic velocity (77 km/s), and the dashed line is the mean velocity of forbidden lines (84 km/s).

1984 was insignificant and cannot provide an explanation for this large interval between the discoveries. Recombination theory (case B, medium optically depth to Lyman photons) predicts an H_α/Br_α ratio of about 30 [34], so that growing H_α emission can be observed for some time while the Br_α emission is still blocked by the dust envelope (according to the computations of Oudmaijer *et al.* [32]; photospheric radiation contributes only 6% of the total emission near Br_α).

3.5. Radial velocities

As noted above, the line profiles in the spectrum of IRC+10420 are very diverse; nearly all lines are asymmetric, and both photospheric absorption components and envelope emission lines are often present. We measured radial velocities using profile segments near the maxima of emission components and minima of absorption components. There are essentially no significant differences in the radial velocities among spectra s16607, s24212, and s27520. Since spectrum s27520 exhibits the highest signal-to-noise ratio over a wide wavelength range, we present our radial-velocity measurements for this spectrum only.

First and foremost, we are concerned with estimates of the systemic velocity. The first estimates of the center-of-mass velocity for IRC+10420 were based on observations of OH maser lines [3]; the mean position of the maser lines at 1612 MHz corresponded to a velocity of $\sim$75 km/s. Subsequent observations of OH maser emission with good spatial and spectral resolution yielded a mean velocity $V_{LSR} = 74$ km/s for maser condensations in the envelope of IRC+10420 [4]. However, Mutel *et al.* [4] suggested that the systemic velocity of IRC+10420 could be closer to that for the low-velocity maser lines ($\sim$40–50 km/s). Based on observations of the $J = 1 - 0$ transition of the CO molecule, Knapp and Morris [35] found a systemic velocity of $V_{LSR} = 80.9 \pm 5.4$ km/s and an expansion velocity for the molecular envelope of $\sim$50 km/s. In their study of CO line profiles corresponding to the $J = 1$–0, 2–1, 3–2, and 4–3 transitions using high signal-to-noise spectra, Oudmaijer *et al.* [16] derived a systemic velocity of $V_{LSR} = 77 \pm 2$ km/s and an expansion velocity for the molecular envelope of $\sim$40 km/s. Below, we adopt the value $V_{LSR} = 77$ km/s for the systemic velocity of IRC+10420.

The optical absorption and emission lines both display a large scatter in radial velocity, $V_{LSR} = 25$–150 km/s (Fig. 7). A more detailed analysis reveals several groups of lines having similar velocities or showing the same trend in their velocity differences. As a rule, lines within a group possess similar profiles, characteristic of that group.

The first group includes purely photospheric absorption lines of Si II, O I, N I, He I, and Na I (D_1, D_2), as well as the absorption components of the hydrogen lines (Table 4); their mean velocity is $V_{LSR} = 93.0 \pm 1.3$ km/s. The Na I lines have a mean velocity of 103 km/s; if we exclude these, the velocity of the group is $V_{LSR} = 91.3 \pm 0.8$ km/s. The photospheric lines are shifted by approximately 15 km/s to the red relative to the velocity of the system as a whole.

The second group consists of high-velocity hydrogen emission components, which have a mean velocity of $V_{LSR} = 145$ km/s.

The third group contains blueshifted hydrogen emission components, strong saturated blueshifted absorption components of Na I (D_1, D_2) lines, and the K I λ7665 absorption line. The mean velocity for this group is 33 km/s; the mean velocity for the hydrogen lines is 38 km/s, while that for the Na I and K I lines is 28 km/s. The presence of narrow interstellar components of Na I and K I lines with a velocity of 15 km/s in the spectrum of IRC+10420 was shown in [6]. In our spectra, these components cannot be isolated from the envelope components, so the real velocity of the Na I and K I envelope components is higher and is nearly equal to that of the blueshifted hydrogen components. It follows that the velocities of the lines in the second and third groups differ by $\pm$55 km/s from the velocities of the lines in the first group.

Table 4. Mean LSR radial velocities (km/s) for several line groups in spectra of IRC+10420 at different epochs

Group of lines	Radial velocity, km/s			
	1996	1997	1999	2000
Emission components				
[Fe II], [Ca II], [O I]	84	83	83	84
Fe II(46)	77	77	79	91
Fe II(40)	77	73	78	80
Fe II(48,49,74) ($r_{abs} > 0.8$)	58	55	60	63
Absorption components				
He I, O I, N I, Si II	87	91	90	92
$H_{\alpha,\beta,\gamma}$	89	89	89	90
Na I(red)	107	107	104	103
Fe II(42,48,49) ($r_{abs} < 0.5$)	95	96	94	95

The fourth group is formed by forbidden Fe II, Ca II, and O I lines, all of which have approximately equal radial velocities (within the errors); their mean radial velocity is $V_{LSR} = 84 \pm 1$ km/s. The envelope is optically thin to these forbidden lines, so the mean radial velocity for these lines should be approximately equal to that of the system as a whole. In reality, the velocity of the forbidden lines coincides neither with the systemic velocity nor with the velocity of the photospheric lines.

The remaining Fe II, Ti II, Cr II, and Sc II lines can be tentatively subdivided into two large groups consisting only of emission or only of absorption lines. The velocity scatter in both groups is very large. The emission lines have velocities $V_{LSR} = 40-100$ km/s, and the absorption lines have $V_{LSR} = 90-130$ km/s. Such a large scatter cannot be explained solely by the observational errors, since the uncertainty in the radial velocities derived from a single line is ± 5 km/s. However, Figure 7 shows that there are correlations between oscillator strength and velocity for both the emission and absorption lines. Oudmaijer [6] found a similar trend in the radial-velocity variations only for emission lines, whereas he ascribed an approximately constant velocity of $\sim$100 km/s to the absorption lines.

A more detailed analysis of the radial velocities for lines of different ions in the last two groups reveals the following characteristics. The minimum velocity of the Fe II absorption lines is $V^a_{LSR_{min}} = 94$ km/s, which practically coincides with the mean velocity for lines of the first group. The minimum absorption-line velocities for other ions are also close to this value: Ti II, $\sim$92 km/s; Sc II, $\sim$98 km/s; Cr II, $\sim$96 km/s. As already noted, the radial velocities of these ion absorption lines are correlated with their oscillator strengths. This correlation is quite apparent for the Fe II and Cr II lines; the tendency for Ti II lines with higher radial velocities to have lower oscillator strengths is less pronounced. Although the Sc II ion possesses a small number of lines in a narrow range of oscillator strengths, the general trend in the radial-velocity variations is still apparent. Note that the correlation between the velocities and oscillator strengths of absorption lines is the same for lines with obvious emission components and for those with no detected emission components. The correlation between radial velocity and oscillator strength is more pronounced for emission lines of the Fe II, Ti II, Cr II, and Sc II ions, independent of the ion species and the presence of obvious absorption components. Note that the presence of emission or absorption components is characteristic of lines of specific multiplets. For example, Fe II lines with multiplet numbers 25, 34, 35, 36, 40, 41, 46, 55, 57, 72, 73, and >100 have only emission components, while those with multiplet numbers 27 and 38 have only absorption components. Fe II lines with multiplet numbers 37, 42, 43, 48, 49, and 74 have both emission and absorption components, although this last group also shows isolated absorption or emission lines, probably because their second components are too weak.

The upper limits for the radial velocities of emission lines are different for different ions, due to the limited ranges of the corresponding oscillator strengths. The Fe II lines in the spectrum of IRC+10420 have the widest range of oscillator strengths. The highest Fe II emission radial velocity exceeds somewhat the lowest absorption velocity, and is equal to $V^e_{LSR_{max}} = 100$ km/s. On the side of the highest oscillator strengths, the emission radial

velocities converge to the velocity of the blueshifted hydrogen components.

4. DISCUSSION

A large amount of observational data has been accumulated during the many years in which IRC+10420 has been studied, enabling us to refine our understanding of the object's nature. There remains no doubt that it is a very luminous star, at the Humphreys–Davidson limit. The radial velocity of the system as a whole can be used to estimate the dynamical distance to the object based on the Galactic rotation curve. Many recent papers have dealt with determinations of this rotation curve and estimates of the Sun's Galactocentric distance $R_\odot$. There is now evidence that $R_\odot$ is equal to 7.7 kpc, somewhat smaller than the previously accepted distance of 8.5 kpc, and that the rotation velocity of the solar centroid is $\theta_0 = 200$ km/s. The highest velocities along lines of sight with $l < 90°$ for objects participating in the general Galactic rotation are exhibited by those situated at so-called tangential points, i.e., points at the minimum distance from the Galactic center along their lines of sight. In the direction toward IRC+10420 ($l = 47.06°, b = -2.54°$), the tangential point is at a distance of $r = 5.2$ kpc from the Sun, assuming $R_\odot = 7.7$ kpc. Using the $\theta(R)$ relation from [36–38], we obtain a velocity for this tangential point of $V_\tau = 66$ km/s, somewhat below the systemic velocity of IRC+10420. The recent radio survey of the Milky Way in CO emission [39] showed that the maximum radial velocity of molecular clouds in the direction $l = 47°$, $b = \pm 4°$ was 75 ± 2 km/s, in good agreement with the systemic velocity of IRC+10420. It is possible that IRC+10420 is near the tangential point but belongs to a molecular complex that has a projected peculiar component of its rotational velocity about the Galactic center of ~ 10 km/s. Thus, we estimate the dynamical distance to IRC+10420 to be approximately 5 kpc, in agreement with the distance estimate from [9], which took into account interstellar polarization measurements. The luminosity corresponding to this distance corrected for interstellar absorption, $A_V = 7^m$, is $L \approx 5 \times 10^5 L_\odot$ ($M_{\rm bol} = -9.5^m$). This value coincides with our luminosity estimate for IRC+10420 derived from the intensity of the O I λ7773 triplet.

Another unique feature of IRC+10420 is the rapid increase of its photospheric temperature. In 1972, its spectral type was G0–F8 [1], corresponding to a temperature of 5700–6000 K [24]. Based on spectra taken in 1995, Klochkova *et al.* [5] derived a temperature of 8500 K using model atmosphere calculations. Our estimates of the spectral type using data obtained in 2000 correspond to a temperature of 9200 K.

In their analysis of photographic-range brightness variations of IRC+10420 between 1900 and 1977, Gottlieb and Liller [15] found that, following irregular brightness variations between 14^m and 15^m, the brightness increased by 1.2^m in 1925–1977 at a rate of 0.025^m per year. No information about the V-band behavior of the object during this period is available. Broad-band photometric data provide evidence that the star's luminosity has not changed considerably since at least 1972; only small changes of the IR brightness due to the large circumstellar envelope are observed. Let us suppose that the 50-year brightness increase detected in [15] was due solely to a growth in the photospheric temperature, i.e., to variations in the normal color index. We adopt the normal color indices and effective temperatures for yellow supergiants from [40] and the effective temperatures for M supergiants from [41]. If we assume that the supergiant's normal color index in 1972 was $(B-V)_o = 0.66$ (between G0 and F8), it could have been as high as $(B-V)_o = 1.86$ in 1925, corresponding to a subtype later than M5. The difference in the effective temperatures corresponding to these subtypes is about 2600 K. Thus, the hypothesis that the photographic brightness increase was due to changes of the photospheric temperature, with no luminosity increase, implies a heating rate of 50 K/year between 1925 and 1972. Incidentally, this hypothesis is also relevant for the presence of OH maser lines (characteristic of supergiants cooler than M3) in the vicinity of IRC+10420.

Following Fix [7], we assume that the 1980 spectrum was already hotter than F8, and therefore already different than the spectral type in 1972. If we now suppose that Fix's estimate corresponds to F5, the next subtype after F8, the photospheric temperature changed by 750 K in 1972–1980, at a rate of 90 K/year, by 2000 K in 1980–1995, at a rate of 130 K/year; and by 700 K in 1995–2000, at a rate of 160 K/year. It is obvious that the spectral changes of IRC+10420 were less significant in 1972–1980 than in 1980–1995. If the temperature continues to grow, the object could reach the Wolf–Rayet phase in 100–150 years.

If the temperature increase does not affect the star's luminosity variations, the stellar radius must decrease in proportion to the square of its temperature. In the last 30 years, the temperature of IRC+10420 increased by a factor of 1.5, so its radius must have decreased by more than a factor of two. Interferometric observations of IRC+10420 in the late 1997 show that the star's radius was $R = 460 R_\odot$ [42]. We conclude that the radius of IRC+10420 was a factor of 800 larger than the solar radius in 1972 and only a factor of 400 larger in 2000. Our estimates of $M_{\rm bol}$ and $T_{\rm eff}$ can be used to estimate $\log g$. According

to Eq. (1) from [30], the values $M_{\rm bol} = -9.5^m$ and $T_{\rm eff} = 9200$ K correspond to $\log g = 0.9$. The star's mass implied by its radius and surface gravity is $\sim 45 M_\odot$.

Computations of evolution with mass loss [43] show that a $20 M_\odot$ star has a relative surface hydrogen abundance (in terms of numbers of particles) of only 20%. Consequently, during the photospheric temperature increase, helium lines should appear at lower effective temperatures than for classical A supergiants. Therefore, the presence of a strong He I λ5876 line in the 1992–1996 spectra of IRC+10420 (when the metal-line spectral type was A5; cf. Fig. 2 in [5]) is no surprise. The atmosphere of a cool star with this fraction of hydrogen replaced by helium has a somewhat different coefficient for continuum absorption by neutral atoms and negative hydrogen ions, but it has a different mean molecular weight and therefore a different scale height. This will necessarily influence the intensity ratios for lines of metallic ions and atoms. We will present an empirical and theoretical analysis of these effects in a future paper.

Let us now consider the behavior of atomic and ionic lines in the spectrum of IRC+10420. For the luminosity corresponding to a distance of 5 kpc, the mass-loss rate in earlier evolutionary phases was $\sim 10^{-3} M_\odot$/yr [16]. The dynamical lifetime of the circumstellar envelope is estimated to be 5000 years [44]. Thus, the mass of the circumstellar envelope of IRC+10420 is $\sim 5 M_\odot$. There is no doubt that a circumstellar envelope that large will significantly influence the spectrum. If the envelope temperature is $\sim$1000 K [45], a considerable amount of matter will be in dust and molecular phases. The only contribution to the optical line spectrum made by atoms of cool gas and dust in the envelope will be absorption in the Na I and K I resonance lines. The envelope's largest influence on the optical spectrum of IRC+10420 is absorption and scattering by dust. Following Fix [7], it is natural to suppose that scattering by the expanding dust envelope will lead to redshifts of the absorption lines formed in the stellar atmosphere. If we assume that scattering by dust grains is equally probable in all directions and that the distribution of matter in the circumstellar envelope is spherically symmetrical, this redshift should be $V_{\rm exp}/\sqrt{2}$, where $V_{\rm exp}$ is the expansion velocity of the envelope. The results of radio CO-line observations yield an envelope expansion velocity of $V_{\rm exp} = 40$ km/s [16]. Therefore, the redshift in question should be about 30 km/s. If the scattering by dust grains is mainly "forward," then, independent of the distribution of matter in the envelope, we should not observe any shifts in lines corresponding to envelope absorption. The redshift of absorption lines indicated by our observations is 15–20 km/s.

In his modeling of radiation transfer in the expanding envelope of IRC+10420, Fix [7] found that the redshifts for absorption lines should decrease significantly with increasing wavelength. However, we do not detect any significant change in radial velocity with wavelength in our spectra; a similar result was obtained in [6] from a 1993 spectrum. Fix admitted that the set of parameters used in his numerical modeling of the circumstellar envelope of IRC+10420 was not unique. A modern two-component model for the dust envelope around IRC+10420 assumes variations of grain sizes within two orders of magnitude and a complex law for the density variations [45]. For this reason, the absence of a dependence of radial velocity on wavelength does not necessarily rule out the possibility that the observed redshifts are a result of repeated scattering of the star's light in the dust envelope.

Oudmaijer [6] put forth a different explanation for the absorption-line redshifts, suggesting they were associated with an infall of matter onto the stellar surface. This hypothesis is consistent with the observed inverse P Cygni line profiles. If this infall of matter occurs below the dust envelope, scattering by the expanding dust envelope should lead to a redshift of emission components and a still greater redshift of absorption components, which is not observed.

The emission and absorption components of classical (or inverse) P Cygni profiles are formed in the same regions of the spherical circumstellar envelope. In the case of IRC+10420, the emission and absorption components probably originate in different regions. The absorption components are formed in the more-or-less stationary atmosphere of the star, while the emission components originate in a spatially restricted region of the expanding envelope, not in its entire volume (in the latter case, P Cygni profiles would be observed). The observed correlation between oscillator strength and radial velocity could result from the envelope's different optical depths in different lines. The envelope is optically thin to lines with low oscillator strengths, and their radial velocities are close to the systemic velocity, whereas the envelope is optically thick to lines with high oscillator strengths, so we predominately see the approaching side of the envelope's surface.

The mean velocity of the forbidden lines is between the systemic velocity and the mean velocity of atmospheric absorption lines. Let us suppose that the forbidden lines are formed in a region below the dust envelope. In this case, the forbidden lines will experience the same redshift as the absorption lines, due to scattering by grains in the dust envelope. After taking into account this redshift, the mean velocity

of the forbidden lines will be lower than the systemic velocity. To obtain a consistent picture, we must suppose that the region of formation of the forbidden lines also expands but that the receding part is screened by the star, leading to blueshifts of the line centroids relative to the systemic velocity. However, the scattering in the dust envelope reduces the effect of this screening of the receding portion of the gas envelope by the star.

The behavior of the hydrogen lines must be reconciled with this pattern. To explain the H_α profile, Jones *et al.* [9] suggested a model with a circumstellar disk rotating with a projected line-of-sight velocity of 50 km/s. This model cannot explain the Br_α, Br_γ, and Pf_γ profiles, which display only blueshifted emission components [32]. This model (cf. Fig. 12 in [9]) likewise cannot explain the pattern displayed by the metallic and hydrogen radial velocities in our spectra. Oudmaijer *et al.* [32] suggested that these line profiles could be understood if there was a collimated outflow along the line of sight. In this picture, the IR lines are formed so close to the star that emission from the outflow directed away from the observer is completely screened. The Balmer emission lines are formed further from the star, so we can observe both jets. The difference in the intensities of the redshifted and blueshifted emission components are due to screening of the receding portion of the outflow by the star. This scheme is in contradiction with the hypothesis of repeated scattering of radiation in the dust envelope, which is capable of equalizing the intensities of the blue and red emission components of H_α, H_β, and H_γ. In addition, no bipolarity in the outer structures imaged by the HST in the optical is observed [46].

5. CONSLUSIONS

We have presented the results of spectroscopic observations of the peculiar supergiant IRC+10420 obtained in 1997–2000. Using the 6-m telescope of the Special Astrophysical Observatory, we obtained three spectra at wavelengths 4300–8000 Å with high signal-to-noise ratios and a spectral resolution of 15 000 (20 km/s). The spectral type of IRC+10420 estimated from the spectrum obtained in 2000 was A2, corresponding to a temperature of ~ 9200 K. Together with data published earlier, this indicates an ongoing increase of the photospheric temperature. We conclude that IRC+10420 is continuing its rapid evolution toward the Wolf–Rayet phase; the current rate of the photospheric temperature increase is $\sim$120 K/year. The intensity of the O I λ7774 triplet yields a luminosity for the star of $M_{\rm bol} = -9.5^m$. All spectra of IRC+10420 from 1997 to 2000 possess an He I λ5876 line with significant equivalent width (at least 200 mÅ); this is apparently possible at such a low temperature due both to the star's high luminosity and the increased helium abundance in the atmosphere of the supergiant.

We found many emission lines identified with lines of Fe I; the Fe II, Ti II, Cr II, and Sc II ions; and forbidden [O I], [Fe II], and [Ca II] lines. The radial velocity derived from absorption lines with no obvious emission components (He I λ5876, O I, N I, Si II) and from the absorption components of the Balmer lines is 93 ± 1 km/s. The redshift of photospheric lines relative to the star's center-of-mass velocity is the result of scattering in the expanding, optically thick dust envelope. Our observations show a correlation between the radial velocities and oscillator strengths of both emission and absorption lines. We detected variability of the relative intensities of the H_α and H_β emission components.

Our analysis suggests two explanations for the observed properties of IRC+10420. The first is based on the hypothesis of multiple scattering of the stellar radiation in the optically thick expanding dust envelope [7, 47, 48]. In this case, it is difficult to explain the observed intensity ratios of the blueshifted and redshifted Balmer components. The second possibility is that IRC+10420 has a rotating disk, with regions outside the disk polarizing the optical and IR radiation [9]. Distinguishing between these two models will require spectropolarimetric observations with high spectral resolution.

In summary, we are not yet able to formulate a self-consistent interpretation explaining the results of both broad-band polarimetric and high-resolution spectroscopic observations of IRC+10420.

ACKNOWLEDGMENTS

This work was supported by the Russian Foundation for Basic Research (project no. 99-02-18339) and the State Science and Technology Program for Astronomy. This study was also made possible, in part, thanks to grant RP1-2264 from the American Civil Research and Development Foundation (CRDF) for independent states of the former Soviet Union.

REFERENCES

1. R. M. Humphreys, D. W. Strecker, T. L. Murdock, and F. J. Low, Astrophys. J. Lett. **179**, L49 (1973).
2. E. R. Craine, W. J. Schuster, S. Tapia, and F. J. Vrba, Astrophys. J. **205**, 802 (1976).
3. P. T. Giguere, N. J. Woolf, and J. C. Webber, Astrophys. J. Lett. **207**, L195 (1976).
4. R. L. Mutel, J. D. Fix, J. M Benson, and J. C. Webber, Astrophys. J. **228**, 771 (1979).

5. V. G. Klochkova, E. L. Chentsov, and V. E. Panchuk, Mon. Not. R. Astron. Soc. **292**, 19 (1997).
6. R. D. Oudmaijer, Astron. Astrophys., Suppl. Ser. **129**, 541 (1998).
7. J. D. Fix, Astrophys. J. **248**, 542 (1981).
8. C. E. Irvine, IAU Circ., No. 286 (1986).
9. T. J. Jones, R. M. Humphreys, R. D. Gehrz, *et al.*, Astrophys. J. **411**, 323 (1993).
10. J. D. Fix and M. L. Cobb, Astrophys. J. **312**, 290 (1987).
11. B. J. Hrivnak, S. Kwok, and K. M. Volk, Astrophys. J. **346**, 265 (1989).
12. S. Kwok, Ann. Rev. Astron. Astrophys. **31**, 63 (1993).
13. V. P. Arkhipova, N. P. Ikonnikova, V. F. Esipov, and R. I. Noskova, Pis'ma Astron. Zh. **22**, 526 (1996) [Astron. Lett. **22**, 470 (1996)].
14. V. P. Arkhipova, N. P. Ikonnikova, R. I. Noskova, *et al.*, Pis'ma Astron. Zh. **25**, 30 (1999) [Astron. Lett. **25**, 25 (1999)].
15. E. W. Gottlieb and W. Liller, Astrophys. J. **225**, 488 (1978).
16. R. D. Oudmaijer, M. A. T. Groenewegen, H. E. Matthews, *et al.*, Mon. Not. R. Astron. Soc. **280**, 1062 (1996).
17. V. E. Panchuk and S. V. Ermakov, Nauchno-Tekh. Otchet Spets. Astrofiz. Obs., No. 267 (1999).
18. G. A. Galazutdinov, Preprint No. 92, SAO (1992).
19. N. E. Piskunov, F. Kupka, and T. A. Ryabchikova, Astron. Astrophys., Suppl. Ser. **112**, 525 (1995).
20. E. L. Chentsov, V. G. Klochkova, and N. S. Tavolganskaya, Bull. Spec. Astrophys. Obs. **48**, 25 (1999).
21. R. I. Thompson and T. A. Boroson, Astrophys. J. Lett. **216**, L75 (1977).
22. I. M. Kopylov, Izv. Krym. Astrofiz. Obs. **22**, 189 (1960).
23. I. M. Kopylov, Izv. Krym. Astrofiz. Obs. **23**, 148 (1960).
24. V. Straižys and G. Kuriliene, Astrophys. Space Sci. **80**, 353 (1981).
25. A. A. Ferro and V. E. E. Mendoza, Astron. J. **106**, 2516 (1993).
26. B. H. Alfaro, A. A. Ferro, and W. J. Schuster, Publ. Astron. Soc. Pac. **109**, 958 (1997).
27. R. P. Kudritzki, J. Puls, D. J. Lennon, *et al.*, Astron. Astrophys. **350**, 970 (1999).
28. Y. Takeda and M. Takeda-Hidai, Publ. Astron. Soc. Jpn. **50**, 629 (1998).
29. E. Verdugo, A. Talavera, and A. I. Gómez de Castro, Astron. Astrophys. **346**, 819 (1999).
30. Y. Takeda, Publ. Astron. Soc. Jpn. **44**, 309 (1992).
31. R. L. Kurucz, CD-ROM (1993).
32. R. D. Oudmaijer, T. R. Geballe, L. B. F. M. Waters, and K. C. Sahu, Astron. Astrophys. **281**, L33 (1994).
33. M. Broklehurst, Mon. Not. R. Astron. Soc. **153**, 471 (1971).
34. D. G. Hummer and P. J. Storey, Mon. Not. R. Astron. Soc. **224**, 801 (1987).
35. G. R. Knapp and M. Morris, Astrophys. J. **292**, 640 (1985).
36. M. Honma and Y. Sofue, Publ. Astron. Soc. Jpn. **49**, 453 (1997).
37. M. R. Merrifield, Astron. J. **103**, 1552 (1992).
38. I. I. Nikiforov and I. V. Petrovskaya, Astron. Zh. **71**, 725 (1994) [Astron. Rep. **38**, 642 (1994)].
39. T. M. Dame, D. Hartmann, and P. Thaddeus, Astrophys. J. **547**, 792 (2001).
40. V. Straizys, *Multicolor Stellar Photometry* (Mokslas, Vil'nyus, 1977; Pachart Publ. House, Tucson, 1992).
41. V. E. Panchuk, Candidate's Dissertation in Physics and Mathematics (Nizhniĭ Arkhyz, 1978).
42. E. A. Lipman, D. D. S. Hale, J. D. Monnier, *et al.*, Astrophys. J. **532**, 467 (2000).
43. A. Maeder and G. Meynet, Astron. Astrophys., Suppl. Ser. **76**, 411 (1988).
44. J. H. Kastner and D. A. Weintraub, Astrophys. J. **452**, 833 (1995).
45. T. Blocker, Y. Balega, K.-H. Hofmann, *et al.*, Astron. Astrophys. **348**, 805 (1999).
46. R. M. Humphreys, N. Smith, K. Davidson, *et al.*, Astron. J. **114**, 2778 (1997).
47. S. Kwok, J. R. Astron. Soc. Can. **70**, 49 (1976).
48. J. Van Blerkom and D. Van Blerkom, Astrophys. J. **225**, 482 (1978).

Translated by N. Samus'

Astronomy Reports, Vol. 46, No. 2, 2002, pp. 152–160. Translated from Astronomicheskiĭ Zhurnal, Vol. 79, No. 2, 2002, pp. 172–181.

Observed and Calculated Normal Color Indices and Indices in Three Photometric Systems

L. N. Knyazeva and A. V. Kharitonov

Fesenkov Astrophysical Institute, Academy of Sciences of Kazakhstan, Kamenskoe Plato, Almaty, 480068 Kazakhstan

Received March 17, 2001

Abstract—We estimate the reliability of previously derived normal energy distributions for stars by comparing normal color indices in three photometric systems ($WBVR$, $uvby$, and Vilnius) calculated using these distributions with indices derived from photometric observations. Earlier, we used photometric data from $WBVR$ and $uvby$ catalogs to derive normal color indices for these systems not available in the literature, in the form of mean color indices and indices obtained for representative groups of normal, unreddened stars. The results can be used to estimate both the quality of our normal distributions and the reliability of the normal color indices in the three photometric systems considered. © *2002 MAIK "Nauka/Interperiodica".*

1. INTRODUCTION

The main goal of our current work was to check the consistency between the normal stellar energy distributions derived in [1–8] and the normal color indices in various photometric systems. To this end, we have compared the normal color indices calculated from our distributions in three photometric systems with those derived from photometric observations. In [9], based on a comparison of observed and calculated color indices for many stars in three photometric systems, we concluded that an accuracy for the calculated indices comparable to that of the observed indices can be achieved if (i) accurate response functions for the photometric systems are available, (ii) the accuracy in the energy distributions for the studied stars is no worse than 2%, and (iii) the integrated spectral energy distribution for the star used to specify the zero point for the calculated color indices has been reliably determined. Thus, we can check the normal energy distributions for stars by comparing normal color indices derived in the usual way from photometric observations with those calculated from the normal energy distributions.

We compared the observed and calculated normal color indices in three photometric systems for which the most observations are available: Vilnius [10], $uvby$ [11], and $WBVR$ [12]. This enabled us, first, to identify possible errors in the normal color indices derived from photometric observations. Second, the P and X bands of the Vilnius system and B band of the $WBVR$ system involve spectral intervals near the Balmer discontinuity, where there is some uncertainty in spectrophotometric data due to the difficulty in determining the continuum level in the spectra of standard stars. The u and v bands of the $uvby$ system do not include this problematic region and can be used to check the important spectral intervals before and after the Balmer discontinuity. The reliability of our spectral energy distributions at $\lambda > 6000$ Å can be estimated only using $WBVR$ photometry, since the Hα-centered narrow S band in the Vilnius system is not very appropriate for our purposes, and the $uvby$ system extends only to λ6000 Å.

2. DERIVATION OF NORMAL COLOR INDICES

Unfortunately, normal color indices derived from photometric observations of normal, unreddened stars have been acquired only in the Vilnius system [10]. Normal $WBVR$ [12] color indices for individual spectral subtypes are presented in [13]; however, a somewhat nonstandard definition of "normal" is applied in that study. Standard relationships between the MK spectral classification and the normal $uvby$ color indices were derived in [14–18] only for a few spectral subtypes. We do not risk using the data of Straizys from [19, Table 26], since he does not give references to the original studies. All these considerations demanded that we derive normal $WBVR$ and $uvby$ color indices ourselves from published photometric observations, as mean values for normal stars of a given subtype, since the normal energy distributions were determined as mean values for a sample of unreddened normal stars of a given subtype, excluding various variables, peculiar stars, binaries, etc.

1063-7729/02/4602-0152$22.00

Table 1. Normal color indices derived from $WBVR$ observations

Sp	$W-B$	$B-V$	$V-R$	n	Sp	$W-B$	$B-V$	$V-R$	n
B1V	−1.143	−0.198	−0.134	4	F0IV	0.013	0.298	0.255	9
B2V	−0.952	−0.174	−0.128	5	F2IV	−0.031	0.363	0.318	8
B3V	−0.852	−0.159	−0.119	5	F5IV	−0.119	0.431	0.371	15
B5V	−0.705	−0.134	−0.085	12	B5III	−0.646	−0.122	−0.069	8
B6V	−0.639	−0.120	−0.068	11	B6III	−0.533	−0.105	−0.060	6
B7V	−0.569	−0.107	−0.065	12	B7III	−0.566	−0.105	−0.059	16
B8V	−0.429	−0.083	−0.047	25	B8III	−0.461	−0.075	−0.032	16
B9V	−0.334	−0.075	−0.048	11	B9III	−0.282	−0.062	−0.025	16
A0V	−0.049	−0.019	−0.014	23	A0III	−0.095	−0.028	−0.009	9
A1V	0.013	0.012	−0.001	20	A3III	0.172	0.097	0.079	6
A2V	0.068	0.046	0.024	25	A5III	0.155	0.151	0.106	7
A3V	0.107	0.094	0.072	22	A7III	0.165	0.181	0.147	7
A4V	0.119	0.121	0.093	16	F0III	0.118	0.274	0.237	12
A5V	0.120	0.162	0.137	16	G7III	0.567	0.996	0.724	11
A7V	0.120	0.181	0.142	12	G8III	0.492	0.958	0.699	137
F0V	0.016	0.278	0.242	17	G9III	0.621	1.018	0.734	67
F5V	−0.143	0.437	0.379	40	K0III	0.709	1.063	0.764	177
F6V	−0.134	0.460	0.394	23	K1III	0.861	1.132	0.808	145
F7V	−0.131	0.513	0.434	17	K2III	1.024	1.200	0.854	110
F8V	−0.108	0.539	0.450	22	K3III	1.276	1.328	0.942	78
G0V	−0.101	0.596	0.492	17	K4III	1.556	1.468	1.070	61
G2V	−0.016	0.657	0.529	3	K5III	1.724	1.558	1.160	92
G8V	0.061	0.730	0.591	3	M0III	1.850	1.621	1.269	53
B2IV	−1.063	−0.204	−0.153	4	M1III	1.901	1.663	1.361	41
B3IV	−0.852	−0.144	−0.096	7	M2III	1.883	1.675	1.421	65
B5IV	−0.713	−0.128	−0.079	9	M3III	1.866	1.686	1.563	44
B9IV	−0.334	−0.076	−0.055	5	M4III	1.710	1.649	1.770	31
A3IV	0.112	0.079	0.058	7	M5III	1.615	1.623	1.936	8
A7IV	0.128	0.188	0.162	6					

Preliminary lists of stars for this study were obtained as follows. We chose stars of the required spectral subtypes having reliable MK spectral classifications and complete UBV photometry and not noted as variable, binary, peculiar, etc. from the catalog of Hoffleit [20]. These stars were primarily bright $< 6^m.5$ and close to the Sun; parallaxes are available for many, and most are located within 100–150 pc. In the course of deriving the normal distributions, we verified whether the number of chosen stars with available spectrophotometric data was sufficient to characterize the subtype as a whole by calculating mean color indices for those normal stars with complete UBV photometry. Using IUE data, parallaxes, and maps of the distribution of interstellar absorption, these stars were thoroughly analyzed to verify the absence of interstellar absorption. We left only those stars for which the scatter of the $B-V$ color indices did not exceed their natural dispersion [1–8]. The $B-V$ values for the most nearby stars in each subtype

Table 2. Normal color indices and indices in the $uvby$-β system derived from photometric observations

Sp	$b-y$	$m1$	$c1$	β	n	Sp	$b-y$	$m1$	$c1$	β	n
B5V	−0.057	0.103	0.433	2.704	33	G8V	0.448	0.260	0.289	2.577	6
B7V	−0.044	0.109	0.553	2.734	15	B2IV	−0.095	0.078	0.111	2.630	4
B8V	−0.037	0.112	0.672	2.758	39	B3IV	−0.053	0.085	0.296	2.656	15
B9V	−0.031	0.123	0.836	2.809	33	B5IV	−0.050	0.096	0.407	2.674	10
B9.5V	−0.019	0.135	0.980	2.841	30	B9IV	−0.031	0.122	0.808	2.793	12
A0V	0.007	0.152	1.005	2.875	78	A3IV	0.063	0.178	1.068	2.864	22
A1V	0.005	0.159	1.045	2.886	31	A7IV	0.117	0.191	0.943	2.821	8
A2V	0.020	0.177	1.062	2.891	28	F0IV	0.182	0.179	0.773	2.745	17
A3V	0.038	0.182	1.057	2.887	26	F2IV	0.242	0.165	0.645	2.695	11
A4V	0.062	0.184	1.039	2.871	10	F5IV	0.286	0.161	0.520	2.662	24
A5V	0.080	0.188	1.030	2.849	12	B5III	−0.039	0.097	0.443	2.687	6
A7V	0.114	0.192	0.919	2.827	13	B7III	−0.036	0.100	0.564	2.712	14
F0V	0.177	0.179	0.777	2.756	20	B8III	−0.021	0.096	0.632	2.717	13
F5V	0.292	0.158	0.470	2.662	23	B9III	−0.015	0.106	0.829	2.756	17
F6V	0.313	0.159	0.432	2.643	39	A0III	−0.002	0.125	1.016	2.815	13
F7V	0.331	0.165	0.403	2.631	19	A3III	0.064	0.172	1.152	2.856	8
F8V	0.346	0.172	0.388	2.622	23	A5III	0.081	0.199	1.024	2.857	9
G0V	0.378	0.191	0.344	2.604	21	A7III	0.102	0.191	1.034	2.831	10
G2V	0.400	0.215	0.340	2.608	7	F0III	0.187	0.187	0.774	2.750	15
G5V	0.413	0.229	0.329	2.600	10						

were used as standards to estimate the color excesses for the remaining stars. We considered acceptable color excesses to be no more than $0^m.05$, smaller than the natural dispersion of the color indices within a subtype. We derived dependences of $B-V$ on V for each subtype, which did not display any systematic increase of $B-V$ with V, testifying to an absence of appreciable absorption. Individual stars with very blue or very red colors compared to other stars in the subtype were excluded. We believe that we were able to minimize errors related to interstellar absorption in this way.

We took the observed color indices and indices for stars from our resulting lists from [12, 21]. Unfortunately, not all stars selected from the catalog of Hoffleit [20] had $uvby$ and $WBVR$ observations. The number of stars used to derive the normal color indices for each spectral subtype is different for these two systems, since southern stars (with $\delta < -14°$) have not been observed in the $WBVR$ system.

We estimated the scatter of the color indices within each spectral subtype in both photometric systems and excluded several stars that seemed anomalous compared to the majority of the sample stars. The most scatter is shown by the $c1$ indices in the $uvby$ system, probably due to the low accuracy of observations in the u band. We adopted the mean color indices calculated using the remaining stars in each photometric system as the normal color indices for these systems. They are presented in Tables 1 and 2, along with the numbers of stars used, n. The standard deviations in the $WBVR$ system are $0^m.02$–$0^m.06$ for $W-B$ and $0^m.01$–$0^m.02$ for $B-V$ and $V-R$; the standard deviations in the $uvby$ system are $0^m.005$–$0^m.01$ for $b-y$ and $m1$ and $0^m.01$–$0^m.04$ for $c1$.

Table 3 presents the differences Δ between the derived normal $W-B$ and $B-R$ color indices in the $WBVR$ system and the data from [13]. The differences between the color indices for main-sequence spectral subtypes does not exceed the above accuracy of the calculated values. Substantial discrepancies occur for spectral subtypes K3III, M0III and M5III, requiring additional verification of the reliability of our data. $B-V(UBV)$ and $B-V(WBVR)$ relations constructed for stars of these subtypes show a clear linear dependence between them. This enabled us to

Table 3. Comparison of derived normal $WBVR$ color indices and the data of [13]

Sp	$W-B$	$B-R$	$(W-B)_K$	$(B-R)_K$	$\Delta(W-B)$	$\Delta(B-R)$
B5V	−0.705	−0.219	−0.710	−0.239	0.005	0.020
A0V	−0.049	−0.033	−0.064	−0.084	0.015	0.051
A5V	0.120	0.299	0.077	0.286	0.043	0.013
F0V	0.016	0.520	−0.017	0.530	0.033	−0.010
F5V	−0.143	0.816	−0.158	0.810	0.015	0.006
G0V	−0.101	1.088	−0.096	1.090	−0.005	−0.002
G2V	−0.016	1.186	−0.053	1.150	0.037	0.036
B5III	−0.646	−0.191	−0.685	−0.230	0.039	0.039
A0III	−0.095	−0.037	−0.053	−0.050	−0.042	0.013
A5III	0.155	0.257	0.124	0.270	0.031	−0.013
F0III	0.118	0.511	0.039	0.500	0.079	0.011
K0III	0.709	1.827	0.743	1.790	−0.034	0.037
K3III	1.276	2.270	1.709	2.630	−0.433	−0.360
M0III	1.850	2.890	1.878	3.010	−0.028	−0.120
M5III	1.615	3.559	1.488	3.760	0.127	−0.201

Note. The index "K" marks the data of Kornilova and Kornilov [13].

estimate the difference between $B-V(UBV)$ and $B-V(WBVR)$ and to use this to translate our normal color indices from the $WBVR$ to the UBV system. A comparison of the resulting values with the data of Straizys [22] showed them to be in good agreement ($0^m.01-0^m.02$), which we take as confirmation of the reliability of our data.

Table 4 presents the differences Δ between our data and the results obtained by Crawford [15, 16] for main-sequence B–F0 subtypes and A3–A5 giants, and by Olsen [17] for G0V–G8V subtypes. Nearly all subtypes display good agreement; a large discrepancy is seen only for the $c1$ index for subtype A5V.

3. COMPARISON BETWEEN CALCULATED AND OBSERVATIONAL NORMAL COLOR INDICES

We derived calculated normal color indices in the three photometric systems [10–12] based on normal energy distributions taken from [1–8] and the response functions for these systems presented in [23, 24, 12]. The calculation method is described in detail in [9]. Table 5 presents the differences Δ between the observed and calculated normal color indices in these photometric systems. We analyzed these differences taking into account upper limits for possible errors introduced when deriving the normal indices from photometric observations. According to [19], the errors σ of the normal indices $X-Y$, $Y-Z$ and $Z-V$ in the Vilnius photometric system are about $\pm 0^m.02-0^m.04$ and reach $\pm 0^m.05-0^m.06$ for $U-P$ and $P-X$. These last indices are the least accurate for supergiants. Estimates of the accuracies in the derived normal $WBVR$ and $uvby$ color indices are given above. All these values were treated as limits for reasonable differences between the calculated and observed color indices in the corresponding photometric systems.

Columns 2–7 of Table 5 contain differences between observed and calculated color indices in the Vilnius system relative to the V band. The columns represent nearly all spectral subtypes for which we have derived normal distributions. A systematic difference in $V-S$ stands out. This may be due to either an error in the zero-point determination or inaccuracy in the response function adopted. We will consider this problem below.

Columns 8–9 present comparisons for the $WBVR$ system, likewise for color indices relative to V. We have considered these color indices, because the B band encompasses the region of densification of the Balmer lines, and, in the case of $W-B$, it would be difficult to tell whether the W or B band were responsible for any error.

The last three columns of Table 5 present comparisons for the $uvby$ system. Unfortunately, no reliable comparisons can be made for this system, since we

Table 4. Derived normal color indices and indices in the $uvby$-β system compared with results of other studies

Sp	$m1$	$c1$	β	$b-y$	$\Delta(b-y)$	$\Delta m1$	$\Delta c1$	$\Delta\beta$
B5V	0.106	0.420	2.701	–	- -	−0.003	0.013	0.003
B7V	0.107	0.550	2.723	–	- -	0.002	0.003	0.011
B8V	0.118	0.660	2.748	–	- -	−0.006	0.012	0.010
B9V	0.126	0.830	2.795	–	- -	−0.003	0.006	0.014
B9.5V	0.134	0.970	2.827	–	–	0.001	0.010	0.014
A0V	0.154	1.010	2.861	–	- -	−0.002	−0.005	0.014
A2V	0.169	1.080	2.885	–	–	0.008	−0.018	0.006
A3V	0.172	1.080	2.871	0.055	−0.017	0.010	−0.023	0.016
A4V	0.184	1.050	2.864	0.071	−0.009	0.000	−0.011	0.007
A5V	0.195	0.960	2.841	0.090	−0.010	−0.007	0.070	0.008
A7V	0.201	0.900	2.824	0.107	0.007	−0.009	0.019	0.003
F0V	0.191	0.790	2.768	0.158	0.019	−0.012	−0.013	−0.013
G0V	0.182	0.368	2.619	0.368	0.010	0.009	−0.024	−0.015
G2V	0.192	0.347	2.608	0.387	0.013	0.023	−0.007	0.000
G5V	0.221	0.320	2.588	0.420	−0.007	0.008	−0.009	0.012
G8V	0.265	0.293	2.567	0.456	−0.008	−0.005	−0.004	0.010
A3III	0.174	1.140	2.869	0.048	0.016	−0.002	0.012	−0.013
A5III	0.191	1.050	2.855	0.079	0.002	0.008	−0.026	0.002
A7III	0.204	1.000	2.823	0.097	0.005	−0.013	0.034	0.008

Note. Data for B, A and F subtypes are taken from [15, 16] and for G subtypes from [17].

were unable to derive observational normal color indices for main-sequence early B subtypes, late giants, and supergiants. Table 5 does not contain any comparisons in the ultraviolet for late giants for any of the photometric systems, since the normal distributions for these subtypes in [4] begin from λ3425 Å, making it impossible to calculate ultraviolet color indices.

It follows from Table 5 that the observed and calculated normal color indices are in good agreement for most spectral subtypes. However, the differences in $U-V$, $P-V$, $c1$, and $W-V$ for spectral subtypes A7V, B9IV, F0IV, B5III, B9III, A0III, A5III, and F0III appreciably exceed the estimated reasonable limits. Note that the discrepancies between the calculated and observed normal color indices could be due to the use of different stars to derive the normal distributions and normal color indices.

Table 5 not only provides a convenient characterization of our normal distributions, but also enables us to estimate the quality of normal color indices derived from observations.

The final stage of our study is to compare our data and the results obtained by Sviderskene [25] based on calculated Vilnius color indices. When calculating the color indices from Sviderskene's data, we determined the constants specifying the zero-point from the energy distribution for Vega from Table 1 in [25]. We carried out this comparison in order to elucidate the origin of the systematic differences in the calculated and observed normal $V-S$ indices in the Vilnius system. Color indices calculated from our and Sviderskene's data are presented in Table 6. This table indicates an absence of any systematic differences. When the same indices calculated using Sviderskene's data are compared with normal indices derived from the photometric observations of [21], systematic differences appear, of approximately the same magnitude and in the same direction as when our data are used (Table 5). Although the Vega-based zero-point was set using different energy distributions for the calculations of the normal color indices using our and Sviderskene's data, the absence of systematic discrepancies between these two calculated color indices suggests another reason for

Table 5. Comparisons between the observed and calculated normal color indices for three photometric systems Vilnius photometric system, $WBVR$ system, and $uvby$ system

Sp	$\Delta(U-V)$	$\Delta(P-V)$	$\Delta(X-V)$	$\Delta(Y-V)$	$\Delta(Z-V)$	$\Delta(V-S)$	$\Delta(W-V)$	$\Delta(B-V)$	$\Delta(b-y)$	$\Delta m1$	$\Delta c1$
1	2	3	4	5	6	7	8	9	10	11	12
B1V	0.015	0.047	0.045	0.026	0.013	−0.032	0.108	0.067	–	–	–
B2V	−0.068	−0.019	0.005	0.001	0.003	−0.033	0.066	0.045	–	–	–
B3V	−0.077	−0.040	−0.015	0.016	0.009	−0.025	−0.017	0.012	–	–	–
B5V	0.011	0.014	0.008	0.022	0.009	−0.047	0.026	0.016	0.004	−0.002	0.030
B7V	0.031	0.012	0.022	0.032	0.022	−0.037	−0.022	0.005	0.017	−0.002	−0.037
B8V	0.030	0.037	0.029	0.017	0.007	−0.064	−0.001	0.008	−0.002	0.011	−0.034
B9V	0.179	0.150	0.061	0.031	0.021	−0.026	0.003	−0.002	0.000	0.011	0.054
B9.5V	–	–	- -	–	–	–	–	–	−0.002	0.004	0.006
A0V	0.024	0.043	0.010	0.014	0.007	−0.019	−0.018	−0.018	−0.019	0.011	−0.037
A1V	0.033	0.056	0.040	0.025	0.014	−0.030	−0.014	−0.009	−0.008	0.012	−0.022
A2V	0.011	0.039	0.042	0.020	0.009	−0.027	−0.018	−0.013	−0.017	0.026	−0.025
A3V	0.014	0.058	0.058	0.029	0.009	−0.038	0.017	0.004	−0.009	0.011	−0.019
A4V	–	–	–	–	–	–	0.037	0.013	0.010	0.003	−0.019
A5V	0.016	0.050	0.065	0.023	0.019	−0.051	0.017	0.012	−0.003	0.012	−0.005
A7V	−0.053	0.039	0.061	0.021	0.012	−0.023	0.012	−0.013	−0.006	0.029	−0.072
F0V	−0.049	0.001	0.038	0.023	0.008	−0.036	−0.013	−0.028	−0.018	0.017	0.003
F5V	0.009	0.021	0.037	0.016	0.000	−0.014	−0.003	−0.008	−0.005	0.016	−0.012
F6V	–	–	–	–	–	–	0.014	−0.033	−0.013	0.010	0.035
F7V	–	–	–	–	–	–	0.041	−0.011	−0.013	0.009	0.053
F8V	0.023	0.022	0.013	0.006	−0.002	−0.049	0.042	−0.014	−0.013	0.013	0.000
G0V	0.069	0.065	0.027	0.015	−0.005	−0.019	0.003	−0.021	−0.013	0.010	0.041
G2V	−0.025	−0.029	−0.006	0.023	0.012	−0.029	0.003	−0.006	−0.006	−0.006	0.009
G5V	−0.028	0.002	−0.006	0.002	−0.007	−0.018	–	–	−0.025	0.012	−0.033
G8V	0.057	0.061	−0.010	0.003	0.001	−0.034	−0.079	−0.047	−0.018	−0.022	0.014
B2IV	0.039	0.042	0.012	−0.002	0.009	−0.051	0.031	0.013	0.000	0.024	−0.007
B3IV	−0.070	−0.060	−0.029	−0.018	−0.010	−0.067	−0.004	0.024	0.015	0.019	−0.049
B5IV	0.080	0.065	0.016	0.006	0.001	−0.036	0.028	0.024	0.015	0.012	−0.031
B9IV	0.224	0.133	0.048	0.021	0.012	−0.004	−0.101	−0.020	−0.011	0.012	−0.049
A3IV	0.039	0.020	0.012	0.011	0.003	−0.048	−0.015	−0.022	0.007	0.008	−0.010
A7IV	0.010	0.013	0.040	0.026	0.011	−0.010	0.002	−0.034	−0.014	0.014	−0.006
F0IV	−0.024	0.015	0.078	0.051	0.018	−0.013	−0.045	0.014	0.005	0.010	−0.098
F2IV	−0.018	0.015	0.021	0.017	0.005	−0.061	0.005	−0.009	0.000	0.014	−0.029
F5IV	0.066	0.048	0.069	0.037	0.013	−0.043	0.012	0.008	0.012	0.004	−0.002
B2III	0.041	0.040	0.053	0.020	0.025	−0.069	–	–	–	–	–
B5III	−0.107	−0.040	0.005	−0.005	0.001	−0.066	−0.065	0.002	0.002	0.041	−0.166
B6III	−0.035	−0.041	−0.025	−0.022	−0.005	−0.052	0.026	−0.013	–	–	–

Table 5. (Contd.)

1	2	3	4	5	6	7	8	9	10	11	12
B7III	0.095	0.067	0.021	0.014	0.015	−0.046	−0.002	0.015	0.016	0.001	−0.040
B8III	0.157	0.104	0.021	0.010	0.013	−0.033	−0.019	0.021	−0.003	0.048	−0.142
B9III	0.166	0.077	−0.003	0.007	0.007	−0.030	−0.038	−0.017	−0.010	0.008	−0.030
A0III	0.173	0.105	0.070	0.034	0.026	0.029	−0.016	0.003	0.002	0.016	−0.037
A3III	0.006	−0.002	−0.005	0.000	0.002	−0.029	0.011	−0.011	−0.005	0.025	−0.006
A5III	0.125	0.050	0.052	0.017	0.008	0.000	0.046	0.008	0.001	0.023	−0.021
A7III	0.064	0.044	0.072	0.036	0.021	−0.036	0.015	0.003	0.001	0.018	−0.037
F0III	−0.057	−0.010	0.067	0.027	0.015	−0.023	−0.047	0.011	0.013	0.049	−0.269
G7III	–	–	–	–	–	–	–	0.055	–	–	–
G8III	–	0.061	0.027	0.007	0.000	−0.025	–	−0.017	–	–	–
G9III	–	–	–	–	–	–	–	−0.029	–	–	–
K0III	–	0.122	0.058	0.024	0.010	−0.026	–	0.004	–	–	–
K1III	–	0.183	0.108	0.044	0.023	−0.014	–	0.002	–	–	–
K2III	–	0.100	0.049	0.026	0.009	−0.033	–	−0.017	–	–	–
K3III	–	0.014	−0.028	−0.023	−0.014	−0.057	–	−0.013	–	–	–
K4III	–	−0.075	−0.072	−0.050	−0.015	−0.055	–	−0.026	–	–	–
K5III	–	0.044	0.033	0.012	0.013	−0.063	–	−0.016	–	–	–
M0III	–	0.068	0.049	0.017	0.017	−0.035	–	−0.021	–	–	–
M1III	–	0.204	0.103	0.031	0.015	−0.023	–	0.005	–	–	–
M2III	–	0.220	0.076	0.030	0.022	−0.003	–	−0.015	–	–	–
M3III	–	0.121	0.044	0.020	0.002	−0.007	–	−0.005	–	–	–
M4III	–	0.071	−0.030	0.020	−0.015	−0.007	–	−0.001	–	–	–
M5III	–	0.108	0.025	0.092	0.042	−0.022	–	0.013	–	–	–
B1Iab	−0.123	−0.045	0.011	−0.012	0.002	−0.039	–	–	–	–	–
B2Iab	−0.003	0.006	0.017	−0.000	−0.009	−0.062	–	–	–	–	–
B5Iab	0.036	−0.004	0.022	0.008	−0.002	−0.049	–	–	–	–	–
B9Iab	0.007	−0.013	0.029	0.025	0.005	−0.082	–	–	–	–	–
G2Iab	−0.150	−0.098	−0.068	−0.049	−0.015	−0.061	–	–	–	–	–

Table 6. Comparison between normal Vilnius color indices calculated using our normal distributions and the results of [25]

Sp	$\Delta(U-V)$	$\Delta(P-V)$	$\Delta(X-V)$	$\Delta(Y-V)$	$\Delta(Z-V)$	$\Delta(V-S)$
B1V	−0.031	−0.025	−0.004	−0.035	−0.008	0.020
B3V	0.101	0.082	0.038	0.004	0.006	−0.001
B5V	−0.028	0.004	0.040	−0.025	−0.001	0.017
B7V	−0.160	−0.048	0.009	−0.026	0.000	0.004
B8V	−0.146	−0.072	−0.009	−0.015	0.007	0.022
B9V	−0.191	−0.119	−0.044	−0.018	0.001	0.019
A0V	−0.072	−0.031	0.026	−0.017	−0.002	0.000
A2V	0.026	0.016	0.032	0.000	0.016	0.027
A3V	0.018	0.001	0.008	−0.009	0.005	0.028
A5V	0.028	0.023	0.027	0.012	0.004	0.070
A7V	0.048	0.022	0.029	−0.030	0.003	−0.015
F0V	0.041	0.006	−0.023	−0.023	0.004	0.008
F5V	−0.060	−0.014	0.052	0.019	0.008	0.000
F6V	−0.083	−0.013	0.048	0.014	0.009	−0.001
F8V	−0.070	−0.002	0.042	0.021	0.021	0.012
F0IV	0.050	0.009	−0.023	−0.019	0.000	−0.003
F2IV	0.017	0.006	0.034	0.014	0.018	0.010
F5IV	−0.103	−0.070	−0.039	−0.012	0.002	−0.014
G0V	−0.113	−0.020	0.052	0.013	0.018	−0.001
G2V	−0.040	0.017	0.081	0.008	0.008	−0.002
G5V	0.031	0.046	0.101	0.025	0.021	−0.028
G8V	−0.024	0.012	0.059	0.007	0.004	−0.005
B9III	−0.147	−0.043	0.051	−0.001	0.012	0.002
A3III	−0.027	0.001	−0.001	−0.013	−0.001	0.002
A5III	−0.026	0.001	−0.005	−0.027	−0.006	−0.032
A7III	−0.027	−0.029	−0.034	−0.022	−0.007	0.009
F0III	0.062	0.029	−0.034	0.027	0.010	0.020
B5Iab	−0.001	0.014	−0.005	−0.013	0.013	−0.004
G2Iab	0.131	0.123	0.096	0.075	0.030	0.051
G8III	–	−0.011	0.059	0.007	0.007	−0.022
K0III	–	0.004	0.057	0.013	0.016	−0.007
K1III	–	−0.011	0.050	0.012	0.008	−0.027
K2III	–	−0.046	0.074	0.009	0.017	0.000
K3III	–	−0.128	−0.014	−0.002	−0.007	0.008
K4III	–	0.071	0.106	0.028	0.006	0.013
K5III	–	0.012	0.056	−0.013	0.004	−0.004
M0III	–	−0.013	0.051	0.026	0.012	0.011
M1III	–	−0.105	−0.003	0.009	0.000	−0.002
M2III	–	−0.161	0.050	0.020	0.005	−0.005
M3III	–	−0.071	0.052	−0.009	−0.015	−0.055
M4III	–	−0.188	−0.020	0.082	−0.038	−0.013
M5III	–	−0.111	−0.027	−0.059	−0.056	−0.078

the systematic differences between the calculated and observed normal $V-S$ values. These difference are most likely due to inaccuracy in the response function for the S band.

4. CONCLUSION

On the basis of observational data from catalogs [12, 21], we have derived normal color indices in the $WBVR$ and $uvby$ photometric systems and estimated their reliability by comparing these color indices with results obtained in other studies. The results can be applied in some astrophysical problems.

Our comparison of color indices calculated using our normal distributions with those derived from observations in three photometric systems (Vilnius, $WBVR$, and $uvby$) indicates that the normal energy distributions derived in [1–8] form a consistent system with the normal color indices in these three photometric systems. Table 5 serves as a convenient characterization of our normal distributions and can also be used to estimate the reliability of normal color indices in these systems.

5. ACKNOWLEDGMENTS

The authors are grateful to A.V. Kurchakov for useful discussion.

REFERENCES

1. L. N. Knyazeva and A. V. Kharitonov, Astron. Zh. **70**, 760 (1993) [Astron. Rep. **37**, 382 (1993)].
2. L. N. Knyazeva and A. V. Kharitonov, Astron. Zh. **71**, 264 (1994) [Astron. Rep. **38**, 231 (1994)].
3. L. N. Knyazeva and A. V. Kharitonov, Astron. Zh. **71**, 458 (1994) [Astron. Rep. **38**, 400 (1994)].
4. L. N. Knyazeva and A. V. Kharitonov, Astron. Zh. **73**, 67 (1996) [Astron. Rep. **40**, 57 (1996)].
5. L. N. Knyazeva and A. V. Kharitonov, Astron. Zh. **73**, 906 (1996) [Astron. Rep. **40**, 823 (1996)].
6. L. N. Knyazeva and A. V. Kharitonov, Astron. Zh. **75**, 70 (1998) [Astron. Rep. **42**, 60 (1998)].
7. L. N. Knyazeva and A. V. Kharitonov, Astron. Zh. **75**, 197 (1998) [Astron. Rep. **42**, 169 (1998)].
8. L. N. Knyazeva and A. V. Kharitonov, Astron. Zh. **77**, 619 (2000) [Astron. Rep. **44**, 548 (2000)].
9. L. N. Knyazeva and A. V. Kharitonov, Astron. Zh. **77**, 385 (2000) [Astron. Rep. **44**, 334 (2000)].
10. V. Straizys and A. Kazlauskas, Baltic Astron. **2**, 1 (1993).
11. D. L. Crawford and J. V. Barnes, Astron. J. **75**, 978 (1970).
12. V. G. Kornilov, I. M. Volkov, A. I. Zakharov, *et al.*, Tr. Gos. Astron. Inst., Mosk. Gos. Univ. **63**, 3 (1991).
13. L. N. Kornilova and V. G. Kornilov, in *Spectrophotometric and Photometric Catalogues. Standard Stars and Analogs of the Sun*, Pulkovo, 2000, p. 40.
14. D. L. Crawford, Astron. J. **80**, 955 (1975).
15. D. L. Crawford, Astron. J. **83**, 48 (1978).
16. D. L. Crawford, Astron. J. **84**, 1858 (1979).
17. E. H. Olsen, Astron. Asrtrophys., Suppl. Ser. **57**, 443 (1984).
18. D. Kilkenny and D. C. B. Whittet, Mon. Not. R. Astron. Soc. **216**, 127 (1985).
19. V. Straizys, *Multicolor Stellar Photometry* [in Russian] (Mokslas, Vil'nyus, 1977).
20. D. Hoffleit, *The Bright Star Catalogue* (Yale Univ. Observatory, New Haven, 1991, 5th ed.).
21. B. Hauck and M. Mermilliod, Astron. Astrophys., Suppl. Ser. **129**, 431 (1998).
22. V. Straizys, *Multicolor Stellar Photometry* (Pachart Publ. House, Tucson, 1992).
23. V. Straizys and K. Zdanavicius, Byull. Vil'nyussk. Astron. Obs., No. 29, 15 (1970).
24. K. Kadaira, in *Problems in Stellar Atmospheres and Envelopes,* Ed. by B. Baschek, W. H. Kegel, and G. Traving (Springer-Verlag, Berlin, 1975), p. 155.
25. Z. Sviderskiene, Byull. Vil'nyussk. Astron. Obs., No. 80, 3 (1988).

Translated by K. Maslennikov

Astronomy Reports, Vol. 46, No. 2, 2002, pp. 161–171. Translated from Astronomicheskiĭ Zhurnal, Vol. 79, No. 2, 2002, pp. 182–192.

Solar MHD Turbulence in Regions with Various Levels of Flare Activity

V. I. Abramenko

Crimean Astrophysical Observatory, p/o Nauchnyĭ, Crimea, 334413 Ukraine

Received April 22, 2001

Abstract—The paper continues investigations of MHD turbulence in active solar regions. The statistical distributions of the increments (structure functions) of the turbulent field are studied analytically in the context of a refined Kolmogorov theory of turbulence. Since photospheric transport of the B_z component of the magnetic field is quite similar to that of a scalar field in a turbulent flow, the theory of transport of a passive scalar can be applied. This approach enables us to show that the structure functions are determined by the competition between the dissipation of the magnetic and kinetic energies and to obtain a number of relations between the structure-function parameters and energy characteristics of the MHD turbulence. Taking into account general conclusions that can be drawn on the basis of the refined Kolmogorov turbulence theory, the structure functions of the B_z field are calculated for eight active regions (from measurements of SOHO/MDI and the Huairou Solar Observing Station, China). These calculations show that the behavior of the structure functions is different for the B_z field of each active region. The energy-dissipation index of the fluctuation spectrum (which is uniquely determined by the structure functions) is closely related to the level of flare activity: the more activity, the less steep the dissipation spectrum for a given active region. This provides a means to test and, consequently, forecast the flare activity of active regions. © *2002 MAIK "Nauka/Interperiodica"*.

1. INTRODUCTION

Information on the turbulence of the photospheric plasma can be very helpful in studying the generation and transport of solar magnetic fields and the storage of free magnetic energy in the solar atmosphere. The current paper continues the work of [1], in which it was shown that analyses of power spectra of the longitudinal photospheric magnetic field provide evidence for Kolmogorov turbulence in active regions and non-Kolmogorov turbulence in quiet regions. However, this is only the most general information about the type of turbulence. One relevant direction for further study of the turbulence system is the construction and analysis of structure functions of the turbulent field.

The structure functions introduced by Kolmogorov [2] are statistical moments of the increments of the turbulent field $u(\mathbf{x})$:

$$S_q(r) = \langle |u(\mathbf{x}+\mathbf{r}) - u(\mathbf{x})|^q \rangle. \quad (1)$$

(Here, q is a real number.) For large Reynolds numbers in the inertial interval of scales, they obey the power law

$$S_q(r) \sim r^{\zeta(q)}. \quad (2)$$

The function $\zeta(q)$ is among the main characteristics of the turbulent field. A deviation of $\zeta(q)$ from a straight line indicates intermittent structure, which is equivalent to the concept of a multifractal in a fractal analysis [3, 4]; i.e. a set that consists of a number of subsets, each with its own similarity law. Turbulence theory describes this intermittency in another (equivalent) formulation [5, 6]: the small-scale turbulence tends to be concentrated in individual clumps surrounded by extensive regions of flow containing much smoother large-scale disturbances.

Moreover, our present study shows that, if the random field considered is a passive scalar transported by the turbulent flow, the function $\zeta(q)$ is determined by the competition between the dissipation of the passive-scalar energy and the kinetic energy of the flow. In our case, when the role of the passive scalar is played by the longitudinal magnetic field, $\zeta(q)$ depends directly on the scale invariance of the dissipation of the magnetic energy. Since the dissipation of free magnetic energy determines the flare activity of a group, it is quite natural that the form of the $\zeta(q)$ curve is closely related to the level of flare generation of an active region (AR).

The analyses of the structure functions of the magnetic field in the solar photosphere presented here, both analytical (Sections 2, 3) and numerical, based on magnetograms (Section 4), have been performed purely in the framework of a refined Kolmogorov turbulence theory [5, 7, 8]. Recently, solar-physics studies have frequently employed another approach, based on fractal analyses [9–14] (see also the Introduction in [1]). To provide a comparison

1063-7729/02/4602-0161$22.00

of these two approaches, we shall formulate our conclusions in the contexts of both.

Russian terminology of recent years [15–17] uses the terms "scaling" for the scale invariance in the inertial scale interval and "scaling index" for the similarity power-law index. We shall follow this convention.

2. BEHAVIOR OF STRUCTURE FUNCTIONS IN THE REFINED KOLMOGOROV TURBULENCE THEORY

The Kolmogorov theory of turbulence [2] is based on the assumption that the turbulent flow is locally isotropic; namely, the probability distributions for an increment

$$\Delta\mathbf{u}(\mathbf{r}) = (\mathbf{u}(\mathbf{x}) - \mathbf{u}(\mathbf{x}+\mathbf{r})) \tag{3}$$

are assumed to be independent of the initial spatial point (uniform) and time (stationary) and to be invariant with respect to rotation and mirror reflection of the reference frame.

Consequently, to visualize the local isotropy, Kolmogorov proposed the hypothesis of a cascade redistribution of energy in turbulent flows: the energy necessary to sustain stationary turbulence is supplied from external sources via the continuous excitement of motions on a scale L for the system in question. The vortices on the scale L break up into smaller and smaller vortices, until the scale η on which the vortices decay due to viscosity is reached. This disruption is accompanied by a redistribution of the kinetic energy of large vortices to that of smaller vortices; i.e., an energy transfer from scales L to scales η.

To describe turbulence mathematically, Kolmogorov introduced two additional hypotheses, the so called similarity hypotheses. We do not present their original formulation here (see, for example, [2, 5]), designated K41 in the literature, and use the refined (refined K41) forms [5, 7, 8].

First Similarity Hypothesis. For an arbitrary turbulent flow with a given viscosity coefficient ν, the probability distributions for the increment $\Delta\mathbf{u}(r)$ restricted by the condition of fixed dissipation of energy ε_r

$$\varepsilon_r(\mathbf{x}_0,t) \equiv \frac{6}{\pi r^3}\int_{|\mathbf{r}_1|<r/2}\varepsilon(\mathbf{x}_0+\mathbf{r}_1,t)d\mathbf{r}_1 \tag{4}$$

are isotropic and depend only on ε_r and ν. There is a single combination of r and ε_r that gives the dimension of velocity

$$u_r = (r\varepsilon_r)^{1/3} \tag{5}$$

and a single dimensionless combination

$$Re_r = \frac{u_r r}{\nu} = \frac{r^{4/3}\varepsilon_r^{1/3}}{\nu} = (r/\eta_r)^{4/3}, \tag{6}$$

where

$$\eta_r = (\nu^3/\varepsilon_r)^{1/4} \tag{7}$$

is the scale length on which the effects of viscosity begin to be important.

Second Similarity Hypothesis. For $L \gg r \gg \eta_r$, i.e., within the inertial interval, distributions subject to the first hypothesis are independent of ν.

It follows from the first hypothesis that, for $r \ll L$ and fixed ε_r, the longitudinal and transverse structure functions [5] of the field $\mathbf{u}(\mathbf{x})$

$$S_q^{(L)}(r) = \langle|u_L(\mathbf{x}+\mathbf{r}) - u_L(\mathbf{x})|^q\rangle, \tag{8}$$

$$S_q^{(N)}(r) = \langle|u_N(\mathbf{x}+\mathbf{r}) - u_N(\mathbf{x})|^q\rangle, \tag{9}$$

take the forms (here, u_L and u_N are the projections of the vector $\mathbf{u}$ onto the direction of $\mathbf{r}$ and the corresponding perpendicular direction, and q is an arbitrary real number that is not necessarily an integer; see, for example, [6])

$$S_q^{(L)}(r) = C^{(L)}(u_r)^{q/3}\beta_q^{(L)}(r/\eta_r), \tag{10}$$

$$S_q^{(N)}(r) = C^{(N)}(u_r)^{q/3}\beta_q^{(N)}(r/\eta_r), \tag{11}$$

where the C are constants and the β_q are functions of (r/η_r).

According to the second similarity hypothesis, the quantity ν must be absent from (10) and (11) in the inertial interval. By virtue of relations (5)–(7), this can occur only when

$$\beta_q^{(L)}(r/\eta_r) = C_1(r/\eta_r)^{q/3}, \tag{12}$$

$$\beta_q^{(N)}(r/\eta_r) = C_2(r/\eta_r)^{q/3} \tag{13}$$

or

$$S_q^{(L)}(r) = A_1(\varepsilon_r r)^{q/3}, \tag{14}$$

$$S_q^{(N)}(r) = A_2(\varepsilon_r r)^{q/3}. \tag{15}$$

Relations (14) and (15) show that, within the inertial interval, the longitudinal and transverse structure functions of the locally isotropic turbulent vector field obey the same power law. The importance of this conclusion becomes clear if we recall that all findings of the Kolmogorov turbulence theory, and especially its experimental verification [5, 18], were obtained for longitudinal structure functions. In our case, we have a cross section of the vector field in the plane of the sky and can determine only the transverse structure function. The fact that relations (14) and (15) show the same behavior for the transverse and longitudinal structure functions in the inertial interval enables us to work with the transverse functions while applying the refined Kolmogorov theory.

Expressions (14) and (15) describe conditional statistical features of the field (under the constraint of fixed energy dissipation ε_r). To obtain unconditional

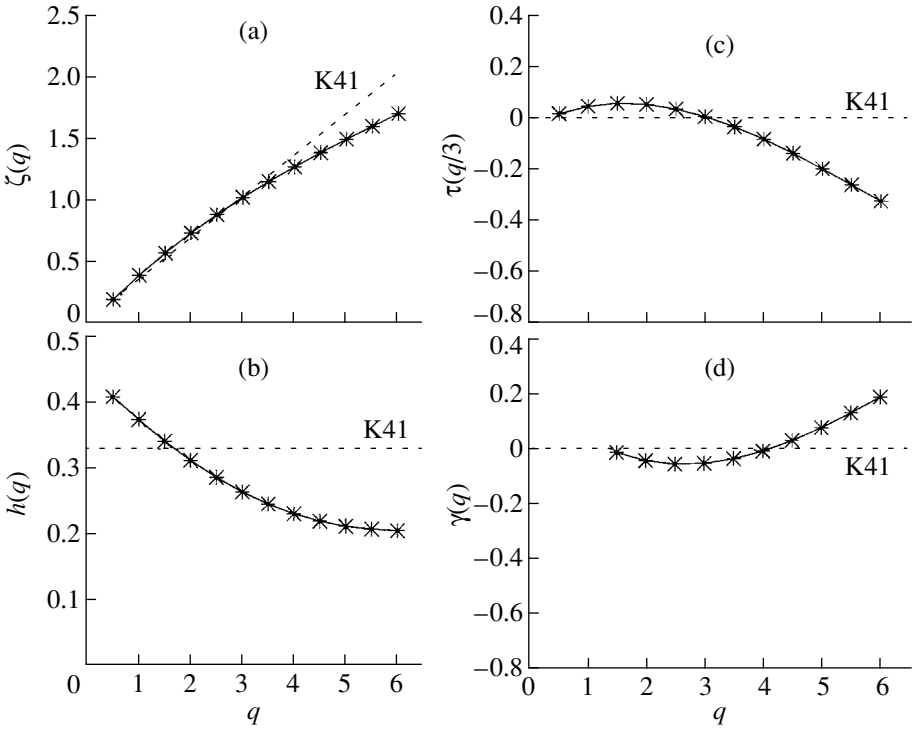

Fig. 1. Turbulence parameters calculated as functions of the moment q in terms of the longitudinal structure functions of the turbulent velocity field determined from the wind velocity measured in the Earth's atmosphere [18] (solid curves with asterisks): (a) scaling index $\zeta(q)$ for the structure functions; (b) the derivative $h(q) = d\zeta/dq$; (c) scaling index $\tau(q/3)$ for fluctuations of the energy dissipation in the turbulent flow; and (d) correction $\gamma(q)$ to $q/3$ in the function $\zeta(q)$ of the passive scalar scaling in (31) for weak intermittency of fluctuations of the scalar dissipation (see Section 3, case a). The dashed line marked K41 presents the behavior of the same parameter in the classical K41 theory.

characteristics, we must average the conditional features over all possible ε_r [5]. A probabilistic averaging of (14) and (15) for $q = 3$ yields (due to the ergodicity theorem)

$$S_3(r) = A(\bar{\varepsilon} r). \tag{16}$$

Here, $\bar{\varepsilon}$ is the ensemble-averaged value of the random variable $\varepsilon(\mathbf{x}, t)$. Since $\bar{\varepsilon}(\mathbf{x}, t)$ is virtually constant in regions small compared to L [5], $\bar{\varepsilon}_r = \bar{\varepsilon}$ when $r \ll L$. Hence, for locally isotropic turbulent fields in the inertial interval, the quantity $\zeta(3)$ in the expression

$$S_q(r) \sim (r)^{\zeta(q)} \tag{17}$$

is equal to unity.

This conclusion is rather general and does not require any additional hypotheses about the behavior of the random field $\varepsilon(\mathbf{x}, t)$, except that necessary for the application of the ergodicity theorem: the integral of the correlation function $\varepsilon(\mathbf{x}, t)$ of the field must converge [5]. However, for the structure functions, whose dependence on ε_r is nonlinear, the single average value $\bar{\varepsilon}_r = \bar{\varepsilon}$ is not longer sufficient, and information about the probability distribution of ε_r is required.

In the original turbulence theory (K41), Kolmogorov assumed that, within the inertial interval, probability distributions subject to the similarity hypotheses depend on the average energy dissipation $\bar{\varepsilon}$. Then

$$\zeta(q) = q/3, \tag{18}$$

which is a straight line with a slope of $1/3$ and derivative

$$h(q) \equiv \frac{d\zeta(q)}{dq} = 1/3 \tag{19}$$

for arbitrary q.

If we assume that the moments $\langle \varepsilon_r^q \rangle$ obey power laws in the inertial interval or, in other words, that the energy-dissipation field is a multifractal (see, for example, [3]),

$$\langle \varepsilon_r^q \rangle \sim r^{\tau(q)}, \tag{20}$$

we obtain in the framework of the refined similarity hypotheses [3]

$$\zeta(q) = q/3 + \tau(q/3). \tag{21}$$

The function $\zeta(q)$ can now differ from a straight line with slope $1/3$, though it will pass through the point $\zeta(3) = 1$, by virtue of (16). Figure 1 shows the functions $\zeta(q)$, $h(q)$, and $\tau(q/3)$ for the velocity field

of a turbulent flow (from wind-velocity measurements in the Earth's atmosphere [18]).

We have already seen that, from the point of view of the general theory of turbulence, deviations of $\zeta(q)$ from a straight line with slope 1/3 can be attributed to individual features of the energy-dissipation field of a given turbulent medium. The statistical characteristics of the dissipation field carry the imprint of large-scale motions, even in the inertial interval [5]. Thus, in general, $\zeta(q)$ can be different for different types of turbulent flows.

The assumption that the dissipation $\varepsilon_r(\mathbf{x}, t)$ has a logarithmically normal (lognormal) probability distribution [7, 8, 19] (i.e., $\ln \varepsilon_r$ is distributed normally) becomes, in fact, the Third Similarity Hypothesis. For the velocity increment, this makes it possible to express $\tau(q)$ explicitly in terms of a positive dimensionless quantity μ [5]:

$$\tau(q/3) = \frac{q(3-q)}{18}\mu, \quad 0 < \mu < 1. \qquad (22)$$

The experimental estimates [20, 21] show that μ is 0.2–0.4 for the velocity increment in a turbulent flow. The assumption that the dissipation has a lognormal distribution is equivalent to the assumption that perturbations on very different scales are independent [5]. In this case, $\zeta(q)$ must be convex for arbitrary q, and still pass through the point $\zeta(3) = 1$; $h(q)$ must decrease for arbitrary q; and $\tau(q/3)$ must be positive for $q < 3$ and negative for $q > 3$. The functions $\zeta(q)$, $h(q)$, and $\tau(q/3)$ determined experimentally (solid curves in Fig. 1) show precisely the required behavior. Consequently, the hypothesis that the dissipation of fluctuations of the kinetic energy has a lognormal distribution seems quite appropriate for turbulent flows with high Reynolds numbers (see also Fig. 8.8 and references to experiments in [3]).

Using (22) for $q = 6$, we obtain

$$\mu = -\tau(2) = 2 - \zeta(6). \qquad (23)$$

The one-dimensional spectrum of the energy-dissipation field $\varepsilon_r(\mathbf{x}, t)$ demonstrates the scaling [5]

$$E^{(\varepsilon)}(k) \sim k^{\mu-1} \equiv k^{\beta}. \qquad (24)$$

Therefore, the form of $\zeta(q)$ can be used to verify the similarity hypotheses for a given medium, investigate fractal features of the dissipation. In addition, based on the value of $\zeta(6)$, we can determine the quantity β, the index of the spectrum of fluctuations in the energy dissipation.

The physical meaning of the behavior of $\zeta(q)$, $h(q)$, and $\tau(q)$ is that mainly the effects of weak fields are manifest at small q ($q < 1$), since raising this quantity to a fractional power (followed by ensemble-averaging) strengthens the contribution of regions with weak fields and weakens that of strong fields; similarly, at high q (for instance, $q > 3$), primarily the behavior of strong fields is analyzed, since the contribution of weak fields in averaged moments of high orders is negligible. In view of this, the decrease in the function $h(q)$ for the lognormal model means that the h for weak fields exceeds that for strong fields. Since h characterizes the degree of differentiability (smoothness) of a given subset (h is the Hölder exponent [22], which is equal to unity for a function that is everywhere differentiable and zero for a nondifferentiable function), we conclude that weak fields are primarily smoother than strong fields in the lognormal model for locally isotropic turbulence.

3. SCALING FEATURES OF THE B_z COMPONENT OF THE MAGNETIC FIELD

Let us analyze the behavior of structure functions of the B_z component of the magnetic field in turbulent flows.

We can use two-dimensional maps of the longitudinal magnetic field detected in active solar regions observed near the center of the solar disk (to minimize the effect of projection) as measurements of the B_z component of the field $\mathbf{B}$ in the coordinate system (x, y, z), where the (x, y) plane is tangent to the solar surface at the center of the magnetogram. Thus, B_z is available on a grid

$$\omega : (x_i = i \cdot \Delta x, i = 1, \ldots, N_x; \qquad (25)$$
$$y_j = j \cdot \Delta y, j = 1, \ldots, N_y),$$

where Δx and Δy are the magnetogram cell sizes and N_x and N_y are the numbers of points along the width and length of the magnetograms. Using the definition (9), we can calculate the transverse structure function of $\mathbf{B}$:

$$S_q^{(N)}(r) = \langle |B_z(\mathbf{x} + \mathbf{r}) - B_z(\mathbf{x})|^q \rangle, \qquad (26)$$

where $\mathbf{x} \in \omega$, and $r \equiv |\mathbf{r}|$ takes on values from $r_{\min} = 2\sqrt{\Delta x^2 + \Delta y^2}$ to $r_{\max} < \min(N_x \Delta x, N_y \Delta y)$.

On the other hand, the right-hand side of (26) is completely consistent with the definition of the usual structure function $S_q(r)$ of a scalar field B_z. Since the B_z component of the photospheric magnetic field is transported by turbulent plasma flows quite similar to a scalar field [23], we can use the theory of transport of a passive scalar [5]. If $\varepsilon^{(B)}(\mathbf{x}, t)$ is the fluctuation field for the magnetic-energy dissipaton and $\varepsilon^{(v)}(\mathbf{x}, t)$ is the fluctuation field for the kinetic-energy dissipation (which has the same meaning as $\varepsilon(\mathbf{x}, t)$ in the previous section), the refined Kolmogorov theory gives for the second ($q = 2$) structure function

$$S_2(r) = C \left\langle \frac{\varepsilon_r^{(B)}}{(\varepsilon_r^{(v)})^{1/3}} \right\rangle r^{2/3}. \qquad (27)$$

Active regions, their flare activity, and turbulence parameters of the magnetic field

NOAA	Date	Time, UT	Coordinates	Image quality	Flare magnitude		Δh	$D(h_6)$	β
					optical	X-ray			
1	2	3	4	5	6	7	8	9	10
8375	Nov. 4, 1998	16:32	N18 W 08	10	1N	M1.0	0.063	1.82	−1.26
8323	Sept. 4, 1998	01:06	S16 W 03	6.0	1F	M1.5	0.191	1.34	−1.15
7216	July 4, 1992	00:29	N12 E12	6.0	1N	M1.5	0.073	1.76	−1.02
7590	Oct. 20, 1993	04:12	N13 E18	5.5	1B	M1.8	0.075	1.81	−0.95
6786	Aug. 20, 1991	02:19	S10 E 04	5.5	2B	M6.7	0.114	1.58	−0.85
6757	Aug. 4, 1991	06:28	N18 W 09	6.5	2B	X1.5	0.271	1.12	−0.60
6853	Oct. 3, 1991	03:21	S16 W 20	7.0	4B	M7.4	0.383	1.09	−0.45
6659	June 9, 1991	03:21	N 29 W 08	6.0	3B	X1.2	0.453	0.88	−0.27

Generalizing (27) for arbitrary real q yields

$$S_q(r) = C\left\langle \frac{(\varepsilon_r^{(B)})^{q-1}}{(\varepsilon_r^{(v)})^{(q-1)/3}} \right\rangle r^{q/3}. \qquad (28)$$

If we assume that fluctuations of the magnetic- and kinetic-energy dissipation are statistically independent, (28) takes the form

$$S_q(r) = C_1 r^{\tau^{(B)}(q-1)} r^{-\tau^{(v)}((q-1)/3)} r^{q/3}, \qquad (29)$$

where $\tau^{(B)}(q)$ and $\tau^{(v)}(q)$ are the scaling indices of the fluctuations of the magnetic- and kinetic-energy dissipation:

$$\langle(\varepsilon_r^{(B)})^q\rangle \sim r^{\tau^{(B)}(q)}, \langle(\varepsilon_r^{(v)})^q\rangle \sim r^{\tau^{(v)}(q)}. \qquad (30)$$

Then, the scaling index $\zeta(q)$ (17) for the structure functions of B_z takes the form

$$\zeta(q) = q/3 + \tau^{(B)}(q-1) - \tau^{(v)}((q-1)/3) \qquad (31)$$
$$\equiv q/3 + \gamma(q).$$

The contributions of the scaling indices for the fluctuations of the magnetic- and kinetic-energy dissipation in (31) have opposite signs. Consequently, the degrees of intermittency of the magnetic- and kinetic-energy dissipation compete in the B_z scaling. The $\zeta(q)$ plot for B_z does not necessarily pass through the point $\zeta(3) = 1$, and in general, $\zeta(q)$ can be nonconvex, even when the lognormal law is valid for both fields $\varepsilon^{(B)}(\mathbf{x}, t)$ and $\varepsilon^{(v)}(\mathbf{x}, t)$.

To elucidate the character of the competition between the magnetic and kinetic dissipation, we consider two limiting cases.

(d) *Weak intermittency of the magnetic-energy dissipation.* If the degree of intermittency of the magnetic-energy dissipation is much lower than that of the kinetic-energy dissipation:

$$|\tau^{(B)}(q-1)| \ll |\tau^{(v)}((q-1)/3)|, \qquad (32)$$

the correction $\gamma(q)$ to $q/3$ in the function (31) for the passive scalar B_z will be mainly determined by the kinetic-energy dissipation. Here, the correction $\gamma(q)$ is equal to the function $\tau^{(v)}(q/3)$ mirror reflected and shifted to the right by unity. The function $\gamma(q)$ for this case is shown in Fig. 1d.

(b) *Strong intermittency of the magnetic-energy dissipation.* If the degree of intermittency of the magnetic-energy dissipation is much higher than that of the kinetic-energy dissipation:

$$|\tau^{(B)}(q-1)| \gg |\tau^{(v)}((q-1)/3)|, \qquad (33)$$

the correction $\gamma(q)$ is mainly determined by $\tau^{(B)}(q-1)$, while the contribution of the negative term in (31) is small. Here, the behavior of $\gamma(q)$ is close to that of $\tau(q/3)$ in Fig. 1c (assuming a lognormal law for the probability distribution of the magnetic-energy dissipation).

Further, we consider calculations of structure functions for the photospheric longitudinal magnetic field taking into account the general conclusions of the refined Kolmogorov theory of turbulence presented above.

4. OBSERVATIONAL DATA AND CALCULATIONS OF SCALING INDICES FOR STRUCTURE FUNCTIONS

To calculate the turbulence parameters of the photospheric magnetic field, we selected the eight active regions listed in the table. The first (NOAA 8375) was observed by the MDI instrument of the SOHO space laboratory. The observations and magnetogram are presented in [1]. The other seven regions were observed at the Huairou Solar Observing Station (HSOS) of the Beijing Astronomy Observatory, in

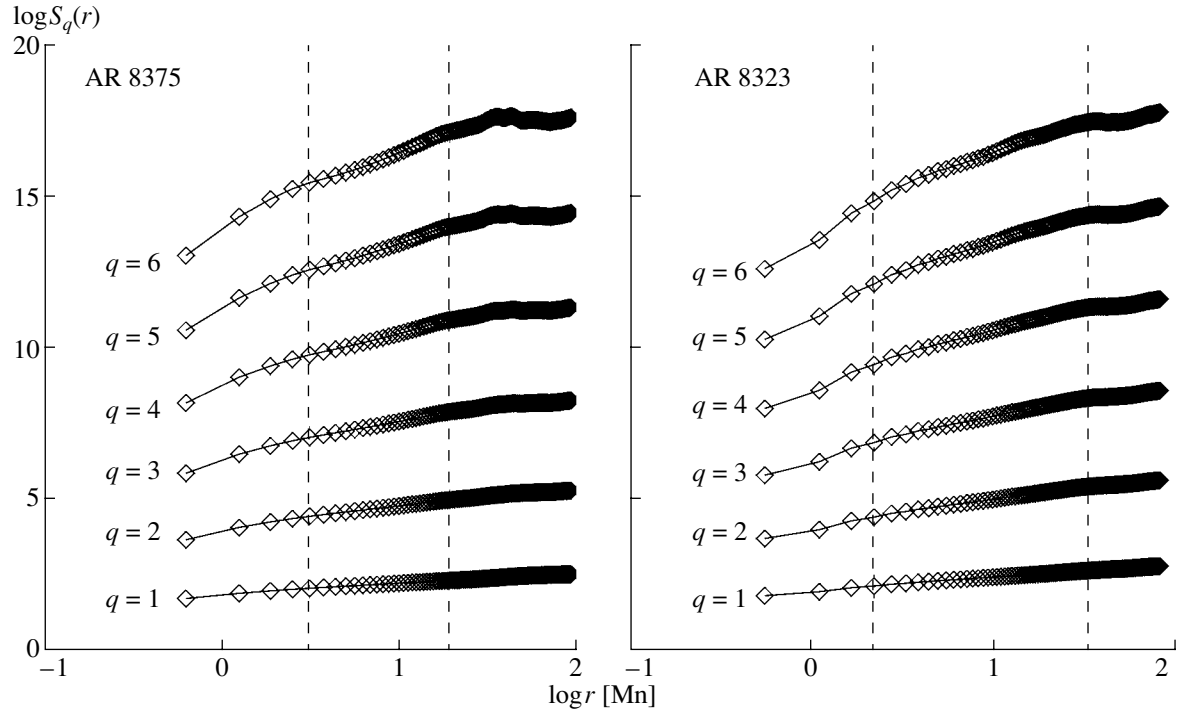

Fig. 2. Structure functions calculated from maps of the B_z component of the magnetic fields of the active regions NOAA 8375 and NOAA 8323 as a function of the logarithm of the scale length. The vertical dashed lines show the inertial interval.

the FeI 532.4 nm spectral line using a videomagnetograph [24]. The resolution of the CCD camera was $0.62'' \times 0.43''$, and the size of the field map was 512×512 cells. The processing of the HSOS data on solar magnetic fields is presented in detail in [25].

When selecting the active regions and magnetograms, we used two criteria. The first is that the active region must be as close as possible to the center of the disk so that we can neglect the effect of projection and treat the measured longitudinal field as the B_z component. The second is that the image quality must be as high as possible for the given observing station. An evaluation (by the observer) of the image quality using numbers from 0 to 10 is presented in the fifth column of the table. In this scheme, the extra-atmospheric SOHO/MDI observations have quality 10. The HSOS maps have qualities of two–four, with the maximum quality being seven.

The sixth and seventh columns of the table present the flare activity of the ARs: the magnitudes of the most powerful flares in the optical and 1–8 Å X-ray ranges (according to Solar Geophysical Data) detected in the given active region over the entire observation period preceding the field measurement. For seven active regions, these proved to be the most powerful flares during the entire period when they were visible on the disk. The flare activity of the ARs in the table grows from top to bottom.

Figure 2 presents the structure functions $S_q(r)$ calculated using (26) for two active regions (on a logarithmic scale). These were each calculated for 12 values of q from 0.5 to 6.0 separated by 0.5, though Fig. 2 shows only those values corresponding to integer q. Each structure function was calculated at 150 points along the scale length r. To obtain each point for an individual function, from 3×10^5 (small r) to 1.5×10^5 (large r) field increments were averaged. Therefore, the errors are very small and are smaller than the plotted symbols. The vertical dashed lines show the beginning and end of the inertial interval, inside which the dependence of $\log S_q(r)$ on $\log r$ can be assumed linear for all q. In choosing the inertial interval, we used the conclusions of [1]: we considered an apparent underestimation of $\log S_q(r)$ for decreasing $\log r$ (a dip in the structure functions at small scales) to be associated with insufficient telescope resolution and deviations from a linear regime at large scales to reflect the absence of turbulent structures on such scales. With the 150 points available along $S_q(r)$, we determined the boundaries corresponding to the vertical dashed lines (Fig. 2) by several methods. The changes in the slope $\zeta(q)$ of the structure functions did not exceed the errors σ corresponding to the uncertainty in the linear regression performed within the inertial interval. The larger q, the greater the deviations of $\log S_q(r)$ from the linear regime we

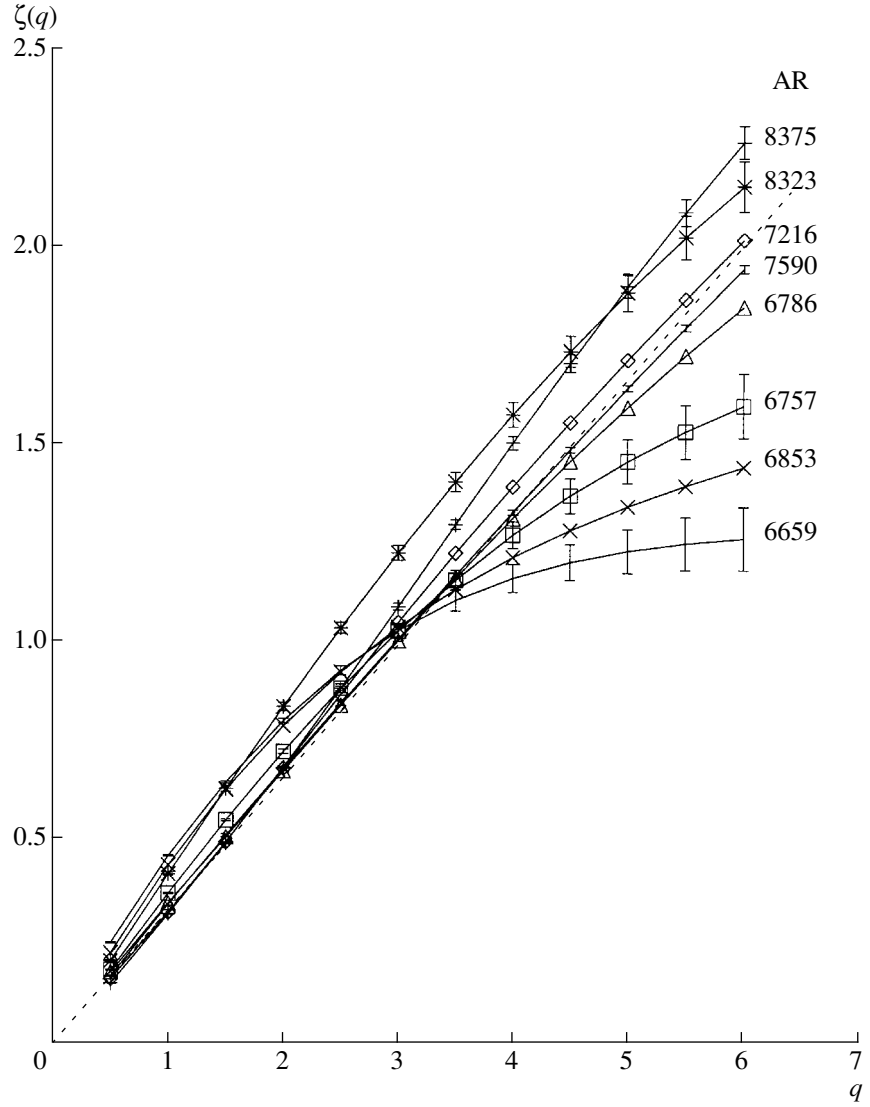

Fig. 3. The functions $\zeta(q)$ calculated as slopes (on a logarithmic scale) of the structure functions $S_q(r)$ within the inertial interval. The classical Kolmogorov K41 line with the slope of 1/3 is shown dashed. The rms deviations are shown only for five active regions and are of the same order for the others.

find in the inertial interval, and, accordingly, the larger the errors σ shown in Fig. 3.

Figure 3 shows the $\zeta(q)$ indices as functions of q for all the active regions in accordance with their definition (17). For each, we can see deviations of $\zeta(q)$ from the classical Kolmogorov K41 line with slope 1/3. $\zeta(q)$ is everywhere above the K41 line for the ARs NOAA 8375 and 8323; close to the K41 line for the ARs NOAA 7216 and 7590; and goes deeper and deeper below the K41 line at high q ($q > 3$) and becomes more convex for the remaining active regions. We especially emphasize that the active regions are arranged here from top to bottom in the same order as they are presented in the table: in order of growing flare activity.

The characteristic features of $\zeta(q)$ are clearly shown by its derivative $h(q)$, presented in Fig. 4. For each active region, $h(q)$ takes its own form. For NOAA 8375 and 7216, $h(q)$ takes its maximum at $q^* = 3$ and $q^* = 2$, respectively. This indicates an inflection point in the $\zeta(q)$ plot: for $q < q^*$ and $q > q^*$, $\zeta(q)$ is concave and convex, respectively. This form for $\zeta(q)$ is not typical of structure functions of the velocity increment in a turbulent flow (see Section 2 and Fig. 1). However, an inflection can be present for a passive scalar as well. Since h is the Hölder exponent of the process, and so describes the intensity of oscillations (see Section 2), and since small q values correspond to weaker fields, we can interpret a decrease in h with decreasing q as a strengthening

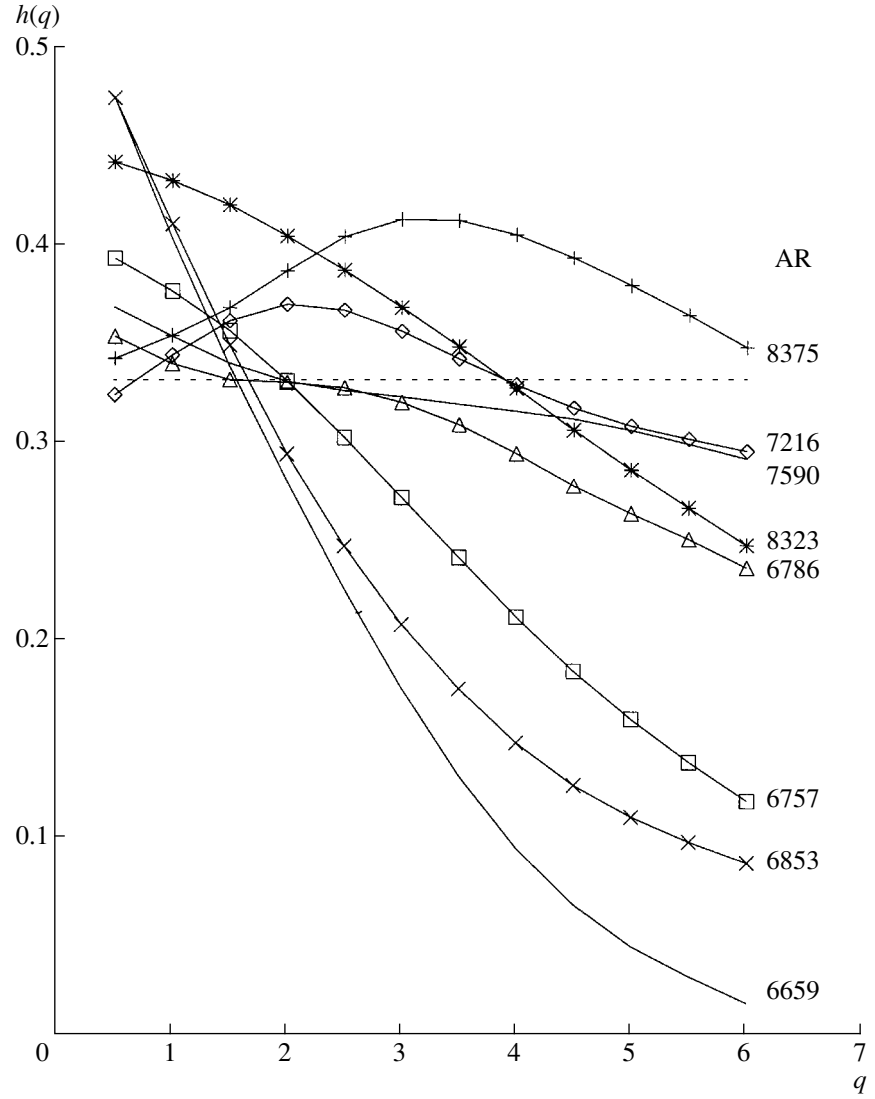

Fig. 4. The functions $h(q)$ calculated as the derivatives $d\zeta/dq$. The line $h = 1/3$ corresponding to the K41 theory is shown dashed. The active regions are marked in the same way as in Fig. 3.

of the intensity of oscillations of the weaker fields of these two active regions. For the remaining active regions, $h(q)$ everywhere monotonically decreases, although with different rates. For NOAA 7590, this function only slightly deviates from the Kolmogorov $1/3$ line, while the rate of the drop in $h(q)$ and the interval in which it occurs increase for the subsequent active regions (i.e., with increase in the flare activity).

The interval Δh of the h variations describes the multifractal complexity of the system [3]: the broader Δh, the richer the set of subsets/monofractals forming the corresponding multifractal system. Δh is presented in the eighth column of the table. We conclude that, the higher the flare activity of a group, the more rich and complex the multifractal field structure of the field, and the broader the range $[D(h(6)), 2]$ of the fractal dimensions $D(h)$ of its subsets. The quantities $D(h(6))$ calculated using the relation [3]

$$D(h(q)) = 2 + qh(q) - \zeta(q) \qquad (34)$$

are given in the ninth column of the table. The quantity $D(h(6))$ provides an estimate of the dimension of the most complex subset (maximally concentrated in rare individual peaks) in our sample. We can see from the table that, the higher the flare activity of an active region, the lower the dimension of the most complex subset, and the richer the system of subsets forming the multifractal B_z. However, NOAA 8323 shows that these phenomena do not always accompany each other: this group with extremely low flare activity has a broad range $\Delta D(h) = [1.34, 2]$ compared to that of the rather flare-productive AR NOAA 6757.

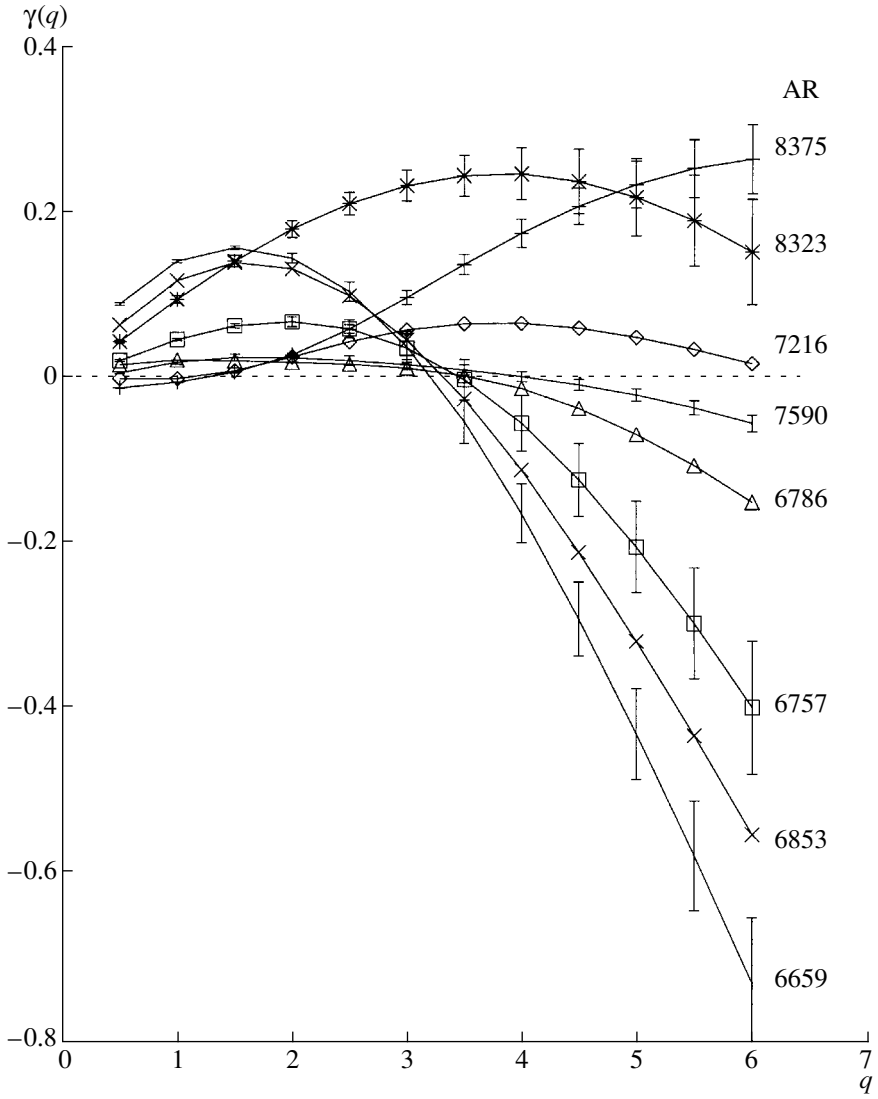

Fig. 5. The functions $\gamma(q)$ calculated as deviations of $\zeta(q)$ from 1/3. The value $\gamma(q) = 0$, corresponding to K41 theory, is shown dashed. The active regions are marked in the same way as in Fig. 3.

Let us consider the scaling of fluctuations of the kinetic- and magnetic-energy dissipation. The functions $\gamma(q)$ calculated using (31) and the known $\zeta(q)$ are shown in Fig. 5. In proportion to the increase in flare activity, $\gamma(q)$ gradually changes from being increasing, concave, and positive (NOAA 8375) to decreasing, convex, and negative at $q > 3$ (NOAA 6659). We can explain this behavior as an effect of the competition between the $\tau^{(B)}$ and $\tau^{(v)}$ terms in (31) and a gradual transition from weak intermittency of the magnetic-energy dissipation (Case a, Section 3) to strong intermittency (Case b).

In active regions with weak flare generation, B_z plays the role of a passive scalar with weak intermittency of fluctuations of the magnetic-energy dissipation. The scaling of the energy dissipation is mainly determined by the dissipation of the kinetic energy.

In ARs with high flare activity, the behavior of B_z is consistent with that of a component of a turbulent flow, and its scaling is quite similar to that of the transverse structure functions of a locally isotropic turbulent field, with all three refined Kolmogorov hypotheses being fulfilled. Here, the scaling of the energy-dissipation field is determined mainly by the magnetic energy.

Deriving $\zeta(6)$ from observations and using (23) and (24), we can calculate the index β for the energy-dissipation spectrum $E^{(\varepsilon)}(k)$: the quantity $\beta \equiv \mu - 1 = 1 - \zeta(6)$ in the expression $E^{(\varepsilon)}(k) \sim k^{\beta}$ is presented in the tenth column of the table. We note the following tendency: the higher the flare activity of

a group, the less steep the energy-dissipation spectrum; i.e., the greater the fraction of the total dissipation power that is concentrated on small scales. In other words, the more small-scale fluctuations contribute to the total dissipation spectrum, the more powerful the flares that can be generated by that active region.

Note that the assumption of a lognormal distribution for the dissipation of the total (magnetic and kinetic) energy is not fulfilled for NOAA 8375 and NOAA 7216 (ARs with low flare activity). In NOAA 6786, 6757, 6853, and 6659 (ARs with high flare activity), the fluctuations of the magnetic-energy dissipation obey a lognormal distribution.

5. CONCLUSIONS

Our analysis of the behavior of turbulence based on refined Kolmogorov similarity hypotheses has enabled us to obtain formula (31), which describes the scale invariance of the vertical component of the photospheric magnetic field, assuming that fluctuations of the kinetic- and magnetic-energy dissipation are statistically independent. This formula can explain the observed behavior of the B_z scaling during the increase in flaring: the higher the flare activity of a group, the higher the intermittency (multifractal composition) of fluctuations of the magnetic-energy dissipation, and the less steep its dissipation spectrum; i.e., the larger the contribution of small-scale fluctuations in the total of magnetic-energy dissipation spectrum.

Experimental evidence for intermittency of photospheric magnetic fields was first obtained in [11] based on a fractal analysis. However, no relations between this intermittency and flare activity have been studied until now. The relations we have discovered are quite natural from a physical viewpoint: solar flares are associated with excess magnetic energy and its dissipation. However, a direct calculation of the field $\varepsilon_r^{(B)}(\mathbf{x}, t)$ from observational data requires information on the total volume vector field and the time behavior of associated processes, which is currently virtually completely lacking. Therefore, the relation between the scaling parameters of the B_z component of the magnetic field and the dissipation of magnetic energy should help appreciably in tests of the level of flare activity of a group and flare forecasting based on magnetograms of the longitudinal magnetic field.

ACKNOWLEDGMENTS

The author is grateful to Prof. G. Zhang, Prof. Wang Jingxiu, and Prof. H.Q. Ai for their permission to use the data of the Huairou Solar Observing Station (China) and to Prof. A.G. Kosovichev for supplying the SOHO/MDI data. The author also thanks V.V. Yurchyshyn, Prof. Wang Haimin, and M.A. Livshits for helpful discussions. This work was supported by the Ukrainian Ministry of Education and Science, NSF-ATM (97-14796), and the National Aeronautics and Space Administration (NAG5-4919).

REFERENCES

1. V. I. Abramenko, V. B. Yurchishyn, H. Wang, and P. R. Goode, Astron. Zh. **78**, 942 (2001) [Astron. Rep. **45**, 824 (2001)].
2. A. N. Kolmogorov, Dokl. Akad. Nauk SSSR **30** (4), 299 (1941).
3. U. Frisch, *Turbulence. The Legacy of A. N. Kolmogorov* (Cambridge Univ. Press, Cambridge, 1995).
4. J. Feder, *Fractals* (Plenum, New York, 1988; Mir, Moscow, 1995).
5. A. S. Monin and A. M. Yaglom, *Statistical Fluid Mechanics* (Nauka, Moscow, 1967; MIT Press, Cambridge, 1975), Chap. 2.
6. Ya. B. Zel'dovich, S. A. Molchanov, A. A. Ruzmaĭkin, and D. D. Sokolov, Usp. Fiz. Nauk **152** (1), 3 (1987) [Sov. Phys. Usp. **30**, 353 (1987)].
7. A. N. Kolmogorov, *La Mechanique de la turbulence* (CNRS, Paris, 1962), p. 447.
8. A. N. Kolmogorov, J. Fluid Mech. **13** (1), 82 (1962).
9. C. J. Schrijver, C. Zwaan, A. C. Balke, *et al.*, Astron. Astrophys. **253**, L1 (1992).
10. J. K. Lawrence and C. J. Schrijver, Astrophys. J. **411**, 402 (1993).
11. J. K. Lawrence, A. A. Ruzmaikin, and A. C. Cadavid, Astrophys. J. **417**, 805 (1993).
12. E. Nesme-Ribes, N. Meunier, and B. Colin, Astron. Astrophys. **308**, 213 (1994).
13. G. Consolini, V. Carbone, F. Berrilli, *et al.*, Astron. Astrophys. **344**, L33 (1999).
14. F. Lepreti, V. Carbone, G. Consolini, *et al.*, in *Magnetic Fields and Solar Processes,* ESA SP Ser. SP-448, **1**, 327 (1999).
15. M. I. Rabinovich and M. M. Sushchik, Usp. Fiz. Nauk **160** (1), 3 (1990) [Sov. Phys. Usp. **33**, 1 (1990)].
16. V. V. Zosimov and L. M. Lyamshev, Usp. Fiz. Nauk **165** (4), 361 (1995) [Phys. Usp. **38**, 347 (1995)].
17. V. S. Dotsenko, Usp. Fiz. Nauk **165** (5), 481 (1995) [Phys. Usp. **38**, 457 (1995)].
18. F. Schmitt, D. Schertzer, S. Lovejoy, and Y. Brunet, Nonlinear Process. Geophys. **1**, 95 (1994).

19. A. M. Obukhov, J. Fluid Mech. **13** (1), 77 (1962).

20. A. S. Gurvich and S. L. Zubkovskiĭ, Izv. Akad. Nauk SSSR, Ser. Geofiz., No. 2, 1856 (1963).

21. F. Anselmet, Y. Gagne, E. J. Hopfinger, and R. A. Antonia, J. Fluid Mech. **140**, 63 (1984).

22. A. V. Bitsadze, *Foundations of the Theory of Analytic Functions of Complex Variables* [in Russian] (Nauka, Moscow, 1984).

23. E. N. Parker, *Cosmical Magnetic Fields: Their Origin and Their Activity* (Clarendon Press, Oxford, 1979; Mir, Moscow, 1982).

24. J. Wang, Z. Shi, H. Wang, and Y. Lu, Astrophys. J. **456**, 861 (1996).

25. V. I. Abramenko, T. J. Wang, and V. B. Yurchishin, Sol. Phys. **168**, 75 (1996).

Translated by V. Badin

Astronomy Reports, Vol. 46, No. 2, 2002, pp. 83–95. Translated from Astronomicheskiĭ Zhurnal, Vol. 79, No. 2, 2002, pp. 99–111.

A Model for Interpenetrating Differential Streams and the Problem of Their Stability

V. A. Antonov and A. S. Baranov

Main Astronomical Observatory, Russian Academy of Sciences, Pulkovskoe sh. 65, St. Petersburg, 196140 Russia

Received July 7, 2000

Abstract—The role of the stability of differential streams in a self-gravitating medium is studied. A simple model with two two-dimensional streams in a thin layer that interact only gravitationally is considered. Instability can develop if the stream-shear parameters have opposite signs; however this condition is not sufficient, and, for some combinations of parameters, the Jeans instability can disappear due to the drift of the perturbations when shear is introduced. The opposite situation is also possible: the system as a whole can be unstable even if both subsystems are stable. Under certain conditions, perturbations do not grow in time but waves are continuously emitted. Criteria are presented for the instability of the system as the whole, depending on the region where the parameters of the subsystem are localized. Common drawbacks of stability analyses in stellar dynamics are briefly discussed in this context. © *2002 MAIK "Nauka/Interperiodica"*.

1. INTRODUCTION

Stability criteria for rotationally symmetric perturbations in galactic disks have, by and large, been formulated fairly convincingly [1–7]. In contrast, the development of asymmetric perturbations is a much more complex problem, due to the differential rotation of the medium and analogous differential propagation of waves. A perturbation that has arisen experiences evolution similar to the case of rotational symmetry but is also progressively sheared due to the differential structure of motions. The result depends on the relative rates of development of two processes: the inherent instability mainly affects the amplitude of the perturbation, while the shear displaces the local wave vector. Therefore, the interplay of the two factors cannot be simply compared arithmetically and requires a more comprehensive study. This challenge is downplayed almost everywhere in the available literature: some terms of equations are frequently omitted without good reason, expansions in a small parameter are employed where they are unlikely to be valid, etc. The situation is more satisfactory concerning oscillation and stability calculations for a differentially rotating system as a single object.

Such analyses of stellar models are fairly numerous [8]. Expansions of perturbations of the potential in properly chosen systems of functions also yield interesting results for elliptical galaxies [9, 10]. Similar calculations of global oscillations are available for gaseous disks [11]. However, all these studies refer to global perturbations, with wavelengths comparable to the size of the system itself; strictly speaking, the notion of wavelength is irrelevant in such cases, whereas the boundary of the system plays an important role, as is the case for the classic figures of equilibrium [12].

Interfaces due to, e.g., sharp bends in angular-velocity profiles are also possible. The simplest case of tangential discontinuity was studied fairly long ago [3]. In a separate publication [13], we analyzed the stability of a discontinuity smoothed to some degree. Cases with gradients of chemical composition or temperature have their own particular features; under certain conditions, such gradients are responsible for an instability resembling the convective instability [14].

Nevertheless, the problem of local perturbations in the absence of sharp boundaries remains insufficiently studied. As will be clarified below, the shear-induced drift of a single wave mode always formally implies stability. At least two interacting material streams or wave processes carried by differential motion in opposite directions are necessary for instability.

It is still not easy to choose a realistic model suitable for a more or less accurate analysis. For this reason, we deal here with a somewhat artificial model, which is, however, subject to typical difficulties inherently related to the differential structure of the motion. In our opinion, a search for "realistic" models is premature and cannot yet deepen our insight into the problem, since other substantial difficulties that have been neglected in past studies but appreciably affect the results remain. As a result, incompletely

1063-7729/02/4602-0083$22.00

substantiated studies have accumulated, and a fallacious impression of adequate comprehension of the problem arises, while appreciable shortcomings remain hidden.

It is the essence of some of these usually overlooked difficulties that we seek to elucidate here using a very simple model.

2. THE MODEL

We abstract ourselves from the rotation itself and consider the differential structure of the translational motion. More precisely, we consider a plane layer of gas consisting of two interpenetrating components with surface densities σ and $\bar{\sigma}$. Their interaction is purely gravitational. A similar situation can arise if gas layers moving parallel to each other are separated by a tangential magnetic field, which prevents them from direct frictional interaction.

We assume that each component does not initially expand or compress, being only sheared. Next, we assume the presence of a neutral line common to the two components, where the velocities of both media vanish. Let us identify this neutral line with the x axis in the coordinate system (x, y). Finally, we assume uniform conditions and obtain the following form for the velocity field in the initial steady state: $v_{0x} = \nu y, \bar{v}_{0x} = \bar{\nu} y, v_{0y} = \bar{v}_{0y} = 0$. Thus, we introduce the quantities ν and $\bar{\nu}$ as the shear coefficients. When taken with opposite signs, they represent the densities of the vorticity. We use overbars everywhere to discriminate between the components. In addition, in the notation used below, t is time, G the gravitational constant, $p(x, y)$ the pressure, c the speed of sound, $\Phi(x, y)$ the potential, $\gamma = \bar{\nu}/\nu$, the symbol δ denotes a linearized perturbation, λ is the growth rate, and μ is the x component of the wave vector.

3. GOVERNING EQUATIONS

We use the regular equations of two-dimensional hydrodynamics:

$$\frac{\partial v_x}{\partial t} + v_x\frac{\partial v_x}{\partial x} + v_y\frac{\partial v_x}{\partial y} = -\frac{1}{\sigma}\frac{\partial p}{\partial x} - \frac{\partial \Phi}{\partial x}, \quad (1)$$

$$\frac{\partial v_y}{\partial t} + v_x\frac{\partial v_y}{\partial x} + v_y\frac{\partial v_y}{\partial y} = -\frac{1}{\sigma}\frac{\partial p}{\partial y} - \frac{\partial \Phi}{\partial y},$$

$$\frac{\partial \sigma}{\partial t} + \frac{\partial}{\partial x}(\sigma v_x) + \frac{\partial}{\partial y}(\sigma v_y) = 0.$$

We linearize equations (1) and separate the variables t and x in the usual way, using multiplication by λ and $i\mu$ instead of t and x differentiation, respectively. This yields

$$(\lambda + i\mu\nu y)\delta v_x + \nu\delta v_y = -i\mu\left(\frac{c^2}{\sigma}\delta\sigma + \delta\Phi\right), \quad (2)$$

$$(\lambda + i\mu\nu y)\delta v_y = -\frac{c^2}{\sigma}\frac{\partial \delta\sigma}{\partial y} - \frac{\partial \delta\Phi}{\partial y},$$

$$(\lambda + i\mu\nu y)\delta\sigma = -\sigma\left(i\mu\delta v_x + \frac{\partial \delta v_y}{\partial y}\right)$$

and similar equations for the second medium.

We apply a Fourier transform to system (2):

$$\int_{-\infty}^{+\infty} \delta\sigma e^{iky} dy = \hat{\sigma}(k), \quad (3)$$

and so on; then, according to the theory of gravitation [15]:

$$\hat{\Phi} = -\frac{2\pi G}{\sqrt{k^2 + \mu^2}}(\hat{\sigma} + \hat{\bar{\sigma}}). \quad (4)$$

As a result, we arrive at the system of equations

$$\left(\nu\mu\frac{d}{dk} + \lambda\right)\hat{v}_x + \nu\hat{v}_y = i\mu\left(\frac{c^2}{\sigma}\hat{\sigma} + \hat{\Phi}\right), \quad (5)$$

$$\left(\nu\mu\frac{d}{dk} + \lambda\right)\hat{v}_y = ik\left(\frac{c^2}{\sigma}\hat{\sigma} + \hat{\Phi}\right),$$

$$\left(\nu\mu\frac{d}{dk} + \lambda\right)\hat{\sigma} = -i\sigma(\mu\hat{v}_x - k\hat{v}_y)$$

and a completely analogous system for the second medium.

We are interested, however, in perturbations growing from zero. These should conserve the same specific vorticity that was present in the steady state:

$$\frac{1}{\sigma}\left(\frac{\partial v_y}{\partial x} - \frac{\partial v_x}{\partial y}\right) = \text{const}. \quad (6)$$

Variation of (6) yields

$$i\mu\delta v_y - \frac{\partial \delta v_x}{\partial y} + \frac{\nu}{\sigma}\delta\sigma = 0, \quad (7)$$

and the Fourier transform of (7) is

$$i\mu\hat{v}_y + ik\hat{v}_x + \frac{\nu}{\sigma}\hat{\sigma} = 0, \quad (8)$$

with completely analogous relations for the other medium. The consistency of (8) with system (5) can easily be checked.

In view of relationship (8), only two independent functions other than $\hat{\Phi}$ remain in system (5), and so this system should reduce to one second-order differential equation. Indeed, applying again the differential operator already present on the left-hand side to the last equation of (5) yields, after some manipulation and taking into account (8),

$$\left(\nu\mu\frac{d}{dk} + \lambda\right)^2\hat{\sigma} - \frac{2\mu\nu\hat{\sigma}}{q}\left[k\left(\nu\mu\frac{d}{dk} + \lambda\right) - \nu\mu\right] \quad (9)$$

$$+ q(c^2\hat{\sigma} + \sigma\hat{\Phi}) = 0,$$

where the notation $q = k^2 + \mu^2$ is used. A completely analogous equation can be obtained for $\hat{\bar{\sigma}}$ [the parameters λ, μ, k, and function $\hat{\Phi}$ given by (4) remain common to both equations].

An exhaustive analysis of the system consisting of (9) and its counterpart for $\hat{\bar{\sigma}}$ is fairly difficult. Here, we restrict our analysis to the case of weak shear; i.e., we consider ν and $\bar{\nu}$ to be small compared to the characteristic frequency μc. We also assume that the corresponding system with $\nu = \bar{\nu} = 0$ is Jeans unstable for the given μ, and a perturbation grows exponentially in this system but does not move. If shear is present, we do not wish to determine the growth rate in all cases but are mainly interested in the situation at the stability threshold, when the quantity λ in (9) is also small.

Under these conditions, the well-known quasi-classical approximation can provide useful guidelines. Specifically, we seek the basic functions in the form

$$\hat{\sigma} = \kappa e^{i\int \psi(k)dk}, \hat{\bar{\sigma}} = \bar{\kappa} e^{i\int \psi(k)dk}, \qquad (10)$$

where κ and $\bar{\kappa}$ are slowly varying functions of k; on the contrary, the phase $\psi(k)$ varies rapidly due to the presence of the small quantity ν or $\bar{\nu}$ in the denominator.

After neglecting small terms in (9), in particular, those containing λ, we easily find for sufficiently large k:

$$\psi = \pm \frac{kc}{\mu\nu}. \qquad (11)$$

It is known that self-gravitation decays as k becomes large [see (4)]; therefore, for ψ specified by (11), the first variable $\hat{\sigma}$ plays a leading role in the equalities (10), whereas $\hat{\bar{\sigma}}$ appears only as a result of the relatively weak gravitational response to $\hat{\sigma}$. Conversely, if we proceed from the differential equation for $\hat{\bar{\sigma}}$, then $\hat{\sigma}$ will be of only minor importance and the formula

$$\psi = \pm \frac{kc}{\mu\bar{\nu}}. \qquad (11^*)$$

will operate instead of (11).

4. DRIFT OF PERTURBATIONS IN k

To clarify the boundary conditions at large k, we return to the triplet of governing equations (5), recovering the original meaning for the factor λ: $\partial/\partial t$. If we consider the particular case where the initial perturbation is restricted to one harmonic in y, i.e., $t = 0$, we have

$$\hat{v}_x = P_1\bar{\delta}(k - k_0), \hat{v}_y = P_2\bar{\delta}(k - k_0), \qquad (12)$$
$$\hat{\sigma} = P_3\bar{\delta}(k - k_0)$$

(here, k_0, P_1, P_2, and P_3 are constants, and $\bar{\delta}$ is the Dirac delta function). We then obtain from Eqs. (5), neglecting the gravitation of the other subsystem,

$$\frac{\partial}{\partial t}\hat{v}_x = \nu\mu P_1\bar{\delta}'(k - k_0) + Q_1\bar{\delta}(k - k_0), \qquad (13)$$
$$\frac{\partial}{\partial t}\hat{v}_y = \nu\mu P_2\bar{\delta}'(k - k_0) + Q_2\bar{\delta}(k - k_0),$$
$$\frac{\partial}{\partial t}\hat{\sigma} = \nu\mu P_3\bar{\delta}'(k - k_0) + Q_3\bar{\delta}(k - k_0),$$

where Q_1, Q_2, and Q_3 depend linearly on P_1, P_2, and P_3.

According to the physical meaning of Eqs. (13), not only is the perturbation gradually deformed, but it also drifts along the k axis at the constant speed $-\nu\mu$. In particular, this is the case for any sufficiently large $|k|$.

Thus, in certain situations, harmonics with large $|k|$ in the expansion of the perturbation are generated by harmonics with moderate k. The sign of k for the admissible, continuously generated higher harmonics depends on the signs of ν and $\bar{\nu}$. In particular, if the shear is directed differently in the two media, e.g., if

$$\nu > 0, \bar{\nu} < 0, \qquad (14)$$

the "creeping" perturbations travel toward large negative k if the leading role is played by $\hat{\sigma}$ and toward large positive k if the leading role is played by $\hat{\bar{\sigma}}$. For a drift in the opposite k direction, i.e., for $k > 0$ if $\hat{\sigma}$ plays a leading role and for $k < 0$ if $\hat{\bar{\sigma}}$ does, both $\hat{\sigma}$ and $\hat{\bar{\sigma}}$ should asymptotically approach zero. This yields the four necessary boundary conditions for our fourth-order system with respect to $\hat{\sigma}$ and $\hat{\bar{\sigma}}$. In contrast, if the shear direction is the same in the two media, neither subsystem prevents the other from drifting even at finite k, and the perturbation disappears as $t \to \infty$.

5. TOPOLOGICAL PROPERTIES OF SOLUTIONS FOR $k \neq 0$

Let us now examine the quasi-classical asymptotics for the entire k axis. For convenience, we use the ansatz

$$\psi = \frac{v}{\nu}, \lambda = -i\omega. \qquad (15)$$

The second equality in (15) reflects the already noted fact that our main concern is with marginal stability. Here and below, we assume ν and $\bar{\nu}$ (proportional to ν) to be small parameters. Upon omitting terms small in this sense, we obtain for the function $v(k)$

$$\begin{vmatrix} -(\mu v-\omega)^2+q\left(c^2-\dfrac{2\pi G\sigma}{\sqrt{q}}\right) & -2\pi G\sigma\sqrt{q} \\ -2\pi G\bar{\sigma}\sqrt{q} & -(\mu v\gamma-\omega)^2+q\left(\bar{c}^2-\dfrac{2\pi G\bar{\sigma}}{\sqrt{q}}\right) \end{vmatrix}=0. \quad (16)$$

Below, we will often use (16) in the unrolled form

$$f=XY-\alpha X-\beta Y+\Delta=0, \quad (17)$$

where the notation $X=(\mu v-\omega)^2, Y=(\mu v\gamma-\omega)^2$ is used for brevity, and the coefficients on the right-hand side of (17) have the form

$$\alpha=q\left(\bar{c}^2-\frac{2\pi G\bar{\sigma}}{\sqrt{q}}\right),\ \beta=q\left(c^2-\frac{2\pi G\sigma}{\sqrt{q}}\right), \quad (18)$$
$$\Delta=c^2\bar{c}^2q^2-2\pi G(c^2\bar{\sigma}+\bar{c}^2\sigma)q^{3/2}.$$

We emphasize that the roots of (16) may coincide pairwise for some k. In this case, within some nearby interval of k, a complex k value will appear instead of coinciding real ones. As the solution for $\hat{\sigma}$ and $\hat{\bar{\sigma}}$ is extended into such an interval of imaginary v, rapid damping should occur, and the harmonics corresponding to some finite wave-number intervals will not actually appear in the solution. To elucidate the situation, we note that, at large $|k|$, the roots always remain real, in accordance with (11) and (11*).

Changes in the parameters can result in the disappearance of the interval of imaginary v. A transition between the two cases—with and without such intervals—is called a topological transformation. A quite similar notion is used in quantum mechanics [16].

The transformation takes place if the conditions

$$f=0, \frac{\partial f}{\partial k}=0, \frac{\partial f}{\partial v}=0 \quad (19)$$

are satisfied.

We write the second of these conditions in terms of X and Y

$$\frac{\partial f}{\partial k}=-\tilde{\alpha}X-\tilde{\beta}Y+\tilde{\Delta}, \quad (20)$$

where

$$\tilde{\alpha}=2\bar{c}^2k-2\pi G\bar{\sigma}\frac{k}{\sqrt{q}},\ \tilde{\beta}=2c^2k-2\pi G\sigma\frac{k}{\sqrt{q}}, \quad (21)$$
$$\tilde{\Delta}=4kc^2\bar{c}^2q-6\pi Gk(c^2\bar{\sigma}+\bar{c}^2\sigma)\sqrt{q}.$$

If $k\neq 0$, the common factor k on the left-hand sides of (21) can obviously be omitted.

In principle, the system of equations (17) and (20) can be solved for X and Y, after which these quantities can be used to determine v and ω. It is important that, in this case, we should have $X\geq 0$ and $Y\geq 0$. If we eliminate, for example, Y from these equations, we arrive at the quadratic equation

$$-\tilde{\alpha}X^2+(\tilde{\Delta}-\alpha\tilde{\beta}+\beta\tilde{\alpha})X+\Delta\tilde{\beta}-\beta\tilde{\Delta}=0. \quad (22)$$

Checking the discriminant of (22) indicates that X and Y are real provided that

$$\eta<\eta^*, \quad (23)$$

where $\eta=\sqrt{q}/\pi G, \eta^*=\sigma/c^2+\bar{\sigma}/\bar{c}^2$.

As η is varied from 0 to η^*, given the other parameters, the point (X,Y) describes a curve. We will prove that this curve does not actually go through the quadrant $X>0, Y>0$. Indeed, such a curve could leave the quadrant through infinite or zero values of X and Y. However, one of the roots (22) becomes infinite at $\tilde{\alpha}=0, \eta=\bar{\sigma}/\bar{c}^2, Y=\alpha=-\pi G\bar{\sigma}\sqrt{q}<0$. Similarly, for $Y=\infty$, we have $X<0$. On the other hand, according to (22), X vanishes at $\Delta\tilde{\beta}-\beta\tilde{\Delta}=0$, or, in unrolled form, at

$$\eta_{3,4}=\frac{4\bar{c}^2\sigma+c^2\bar{\sigma}\pm c\sqrt{\bar{\sigma}(c^2\bar{\sigma}-8\bar{c}^2\sigma)}}{2c^2\bar{c}^2}, \quad (24)$$

obviously provided that the root on the right-hand side of (24) is real. In this case, however, $Y=\Delta/\beta$, and the substitution of any root of (24) yields $\beta>0, \Delta<0$; i.e. $Y<0$. Similarly, $X<0$ at $Y=0$. The possibility remains that the curve of admitted values of X and Y forms a closed loop in the first quadrant, which either does not touch the coordinate axes or is anchored at the origin of the coordinate system (where $X=Y=0, \eta=0$). In this case, however, a maximum of η must be reached somewhere in this loop; i.e., double roots for X,Y must be present at the value $\eta=\eta^*$ already known to us. A fairly simple calculation for this point yields

$$X=-\pi G\sqrt{q}\left(\frac{c^2}{\bar{c}^2}\bar{\sigma}+\sigma\right)<0$$

and, similarly, $Y<0$. Thus, for $k\neq 0$, the combination of signs of $X\geq 0, Y\geq 0$ leads to a contradiction in any case. Therefore, a topological transformation is impossible for $k\neq 0$, which proves our statement. Moreover, since the condition $\partial f/\partial v=0$ is not used in the above proof, the combination $f=0, \partial f/\partial k=0$ without a transformation is also impossible. Thus, the branches of the curves $v(k)$ at $k\neq 0$ are never directed horizontally, and the sections of increases and decreases in these curves contact each other only at the points where a vertical component is present.

Below, we will frequently use Eq. (17) in the form

$$f = (X-\beta)(Y-\alpha) - \Delta_1 = 0, \qquad (25)$$

where $\Delta_1 = \alpha\beta - \Delta = (2\pi G)^2\sigma\bar{\sigma}q > 0$.

6. TOPOLOGICAL PROPERTIES OF SOLUTIONS FOR $k = 0$

It will be important for us to list various cases of transformations for $k = 0$. For the case of a topological transformation, we have the following expansion in the vicinity of the values $k = 0, v = v_0$, which zero the function $f(v, k)$:

$$f \approx \frac{1}{2}\left[k^2\frac{\partial^2 f}{\partial k^2} + (v-v_0)^2\frac{\partial^2 f}{\partial v^2}\right], \qquad (26)$$

since, by virtue of (20) and (21), the derivatives $\partial f/\partial k$ and $\partial^2 f/\partial v\partial k$ vanish. Furthermore, the second derivative with respect to k can be considered a limit for $(1/k)(\partial f/\partial k)$, and the above considerations for $k \neq 0$ show that this second derivative also never vanishes.

The classification of transformations for $k = 0$ is based on the conditions (19), except for the trivial one, $\partial f/\partial k = 0$.

We will frequently refer to particular values of α, β, and Δ at $k = 0$, viz.,

$$\alpha = \mu^2\left(\bar{c}^2 - \frac{2\pi G\bar{\sigma}}{\mu}\right),\ \beta = \mu^2\left(c^2 - \frac{2\pi G\sigma}{\mu}\right), \quad (27)$$
$$\Delta = c^2\bar{c}^2\mu^4 - 2\pi G(\bar{c}^2\sigma + c^2\bar{\sigma})\mu^3.$$

They also determine $\Delta_1 = \alpha\beta - \Delta = (2\pi G)^2\sigma\bar{\sigma}\mu^2 > 0$.

We can write the third of conditions (19) in unrolled form

$$\frac{\partial f}{\partial v} = 2\mu[(Y-\alpha)\sqrt{X} + \gamma(X-\beta)\sqrt{Y}] = 0. \quad (28)$$

For convenience, we introduce the auxiliary variable $\tau = \sqrt{(Y-\alpha)/(X-\beta)}$. We then obtain, combining (28) and (25),

$$Y - \alpha = \tau\sqrt{\Delta_1}, \quad X - \beta = \tau^{-1}\sqrt{\Delta_1}. \qquad (29)$$

Further, we use (28) to obtain

$$\sqrt{\frac{X}{Y}} = -\frac{\gamma}{\tau^2}, \quad \sqrt{\frac{\beta + \tau^{-1}\sqrt{\Delta_1}}{\alpha + \tau\sqrt{\Delta_1}}} = -\frac{\gamma}{\tau^2},$$

which reduces to an algebraic equation for τ, viz.,

$$\beta\tau^4 + \sqrt{\Delta_1}\tau^3 - \gamma^2\sqrt{\Delta_1}\tau - \gamma^2\alpha = 0. \qquad (30)$$

Conversely, if τ is a real root of (30), then the X and Y constructed using relations (29) have the same sign in any case. Only positive values of X and Y suit our needs. It is sufficient to impose the condition $Y > 0$, which is equivalent to

$$\tau > -\frac{\alpha}{\sqrt{\Delta_1}}, \qquad (31)$$

and the necessary conditions (25) and (28) are satisfied for this choice of τ.

A point of uncertainty is the possibility of simultaneous changes in the signs of both $\sqrt{X}$ and $\sqrt{Y}$, which is equivalent to trivial changes in the signs of v and ω. The possible appearance of multiple roots of (30) plays an important role. It is more convenient to deal with the original system of equations (25) and (28) for X and Y rather than with (30) itself. Coincident pairs (X, Y) will be present if the Jacobian of f and $\partial f/\partial v$ as functions of X and Y vanish. This yields $(Y-\alpha)(X+\beta)/\sqrt{X} - \gamma(X-\beta)(Y+\alpha)/\sqrt{Y} = 0$, or, when combined with (28), $(X+\beta)/X = -(Y+\alpha)/Y$.

We now use (25) to obtain $XY = -\Delta/3, \alpha X + \beta Y = 2\Delta/3$, whence we immediately find

$$X = \frac{\Delta \pm \sqrt{\Delta(\Delta + 3\alpha\beta)}}{3\alpha},$$
$$Y = \frac{\Delta \mp \sqrt{\Delta(\Delta + 3\alpha\beta)}}{3\beta}.$$

Since Eq. (28) can be rewritten

$$\gamma^2 = \frac{X(Y-\alpha)^2}{Y(X-\beta)^2},$$

substitution of the above critical X and Y values yields the required condition for multiple roots:

$$\gamma^2 = \frac{\alpha}{\beta}\,\frac{9\alpha\beta\Delta - \Delta^2 \pm (\Delta+3\alpha\beta)\sqrt{\Delta(\Delta+3\alpha\beta)}}{9\alpha\beta\Delta - \Delta^2 \mp (\Delta+3\alpha\beta)\sqrt{\Delta(\Delta+3\alpha\beta)}}. \quad (32)$$

Here, we can assume that $\Delta < 0$; otherwise, X and Y will have opposite signs and γ will be imaginary.

Figure 1 depicts parameter-space regions characterized by specific numbers of real roots for τ. Since the ansatz $\tau = \gamma\tau_1$ reduces (30) to

$$\gamma\sqrt{\frac{\beta}{\alpha}}{\tau_1}^4 + \sqrt{\frac{\Delta_1}{\alpha\beta}}(\tau_1^3 - \tau) - \frac{1}{\gamma}\sqrt{\frac{\alpha}{\beta}} = 0,$$

it is clear that, qualitatively, the behavior of roots is completely determined by two dimensionless parameters, and the following quantities can be used as such parameters:

$$\theta = \arctan\frac{\Delta}{\alpha\beta} = \arctan\left(1 - \frac{\Delta_1}{\alpha\beta}\right) \qquad (33)$$
$$\text{and } \tilde{\gamma} = |\gamma|\sqrt{\left|\frac{\beta}{\alpha}\right|}.$$

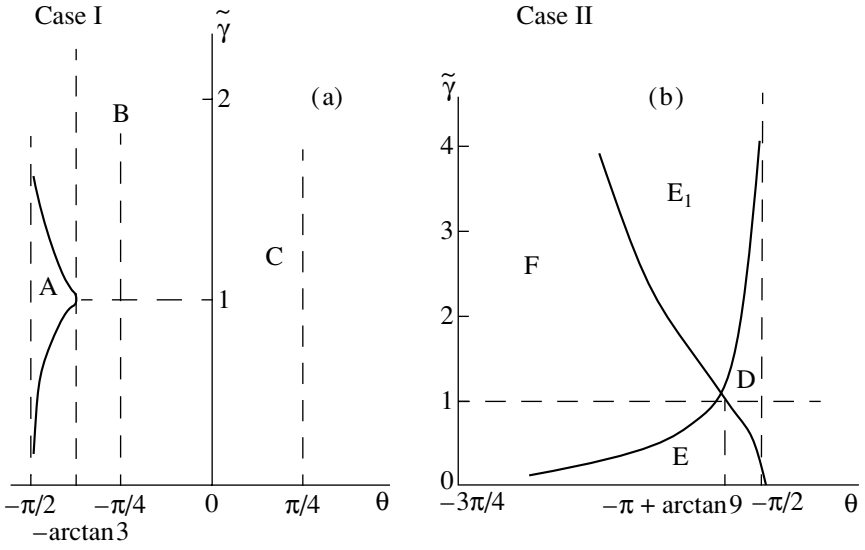

Fig. 1. Graphic representation of the parameter-space regions for various types of transformations.

The cases of $\alpha\beta > 0$ and $\alpha\beta < 0$ should be considered separately. Let us also note the formal meaning of simultaneous changes in the signs of α and β. As is evident from (30), the roots for τ also change their signs in this case; according to (29), X and Y behave similarly. Thus, for fixed γ and Δ, one of the parameter pairs (α, β) and $(-\alpha, -\beta)$ always has a physical meaning, while the other is not appropriate, since X and Y are negative.

Transformations and their qualitative properties

Case I

Regions	A	B	C
$\alpha > 0$	− −	− −	1) − −
$\beta > 0$			2) − +
$\alpha < 0$	1) + −		
$\beta < 0$	2) + −	+ −	Impossible
	3) − −		

Case II

Regions	D	E	E_1	F
$\alpha > 0$	1) + −	1) + −	−	−
$\beta < 0$	2) − −	2) − −		
$\alpha < 0$	1) + −	−	1) + −	−
$\beta > 0$	2) − −		2) − −	

Note: Case I corresponds to $\alpha\beta > 0$, and Case II, to $\alpha\beta < 0$. In each row, the first sign refers to f_{vv} and the second, to f_{kk}. The dashes indicate zero numbers of solutions for the transformations. The impossibility of solutions is noted where the presence of parameters in the given region contradicts physical conditions.

Case I. $\alpha\beta > 0$. The root of (32) can be found if $\Delta + 3\alpha\beta < 0$. Double roots of the equation exist in the region $\tan\theta < -3$, and the relationship between the dimensionless parameters is specified by the curve

$$\tilde{\gamma}^2 = R(\theta), \tag{34}$$

where

$$R(\theta) = \frac{(9 - \tan\theta)\tan\theta \pm \sqrt{\tan\theta(tan\,\theta + 3)^3}}{(9 - tan\,\theta)\tan\theta \mp \sqrt{tan\,\theta(tan\,\theta + 3)^3}}.$$

Case II. $\alpha\beta < 0$. This condition is sufficient to find the root of (32), since $\Delta < 0$ entails $\Delta + 3\alpha\beta < 0$. Thus,

$$\tilde{\gamma}^2 = -R(\theta)\ (\tan\theta > 0). \tag{35}$$

Note that, in both cases, the two branches of the curve, (34) and (35), are symmetric in the sense that they transform into each other as $\tilde{\gamma}$ is replaced with $1/\tilde{\gamma}$. Moreover, we always have $\Delta < \alpha\beta$ so that we do not need to construct full $(\theta, \tilde{\gamma})$ diagrams and can restrict our attention to the region $\tan\theta < 1$ for Case I and to the region $\tan\theta > 1$ for Case II. Let us investigate the shape of the critical curves (34) and (35). We actually have two graphs, since the definition of $\tilde{\gamma}$ contains the nonanalytic modulus operation. Each graph shows regions that are separated by the critical curve and should be considered independently.

We next determine, first, the number of real roots for τ and, second, the signs of α and β necessary for X and Y to be positive, choosing between the two possible combinations at a given $\tilde{\gamma}$ and θ. The regions that must be considered in doing so are sequentially

separated, first, by the critical curves (34) and (35) and, second, by the line at which X and Y change their signs, momentarily becoming equal to zero or infinity. This does not take place for X or Y alone; otherwise, τ would become zero or infinite, which is impossible for finite α and β within the graphs, in view of (30). There is, however, the case where X and Y vanish simultaneously. According to (29), this means that $\tau = -\alpha/\sqrt{\Delta_1}$ or $\tau = -\sqrt{\Delta_1}/\beta$, and both cases are equivalent to $\Delta = 0$. Thus, the straight line $\Delta = 0$, or $\theta = 0$, should be considered the boundary of dissimilar regions. Our considerations are based on continuity and proceed either from the cases of small and large γ or from the case of large Δ.

(a) For small γ, it follows asymptotically from (30) that

$$\tau_1 \approx -\frac{\sqrt{\Delta_1}}{\beta}, \tau_2 \approx \left(\frac{\gamma^2\alpha}{\sqrt{\Delta_1}}\right)^{1/3},$$

and two complex roots exist. At $\tau = \tau_1$, it follows from (29) that $Y \approx \alpha - \Delta_1/\beta = \Delta/\beta$, and we should assume $\beta > 0$ for $\Delta < 0$ (i.e., for region C) and $\beta < 0$ for regions B and E. At $\tau = \tau_2$, formulas (29) imply that $Y \approx \alpha$, and we have $\alpha > 0$ in all three regions B, C, and E.

(b) Similarly, for large γ, we have

$$\tau_1 \approx -\frac{\alpha}{\sqrt{\Delta_1}}, \tau_2 \approx \left(\frac{\gamma^2\sqrt{\Delta_1}}{\beta}\right)^{1/3}$$

and two complex roots. At $\tau = \tau_1$, we find from (29) that $X \approx \beta - \Delta_1/\alpha = \Delta/\alpha$, and $\alpha > 0$ should be taken for $\Delta > 0$ in region C, while $\alpha < 0$ in regions B and E_1. At $\tau = \tau_2$, it follows from (28) that $X \approx \beta$, and $\beta > 0$ in all three regions B, C, and E_1.

(c) Next, at the left edge of region A, the quantity Δ tends to $-\infty$, while Δ_1 tends to $+\infty$. Asymptotically,

$$\tau_1 \approx -\frac{\sqrt{\Delta_1}}{\beta}, \tau_{2,3} \approx \pm\gamma, \tau_4 \approx -\frac{\alpha}{\sqrt{\Delta_1}}.$$

For $\tau = \tau_1$, we have again $Y \approx \alpha - \Delta_1/\beta = \Delta/\beta$; since $\Delta < 0$ in region A, $\alpha < 0, \beta < 0$. For $\tau = \tau_4$ we have $X \approx \beta - \Delta_1/\alpha = \Delta/\alpha$ and also $\alpha < 0, \beta < 0$. Finally, for $\tau = \tau_{2,3}$ we obtain $Y \approx \pm\gamma\sqrt{\Delta_1}$.

One of these solutions is appropriate, being compatible with $\alpha > 0, \beta > 0$ as well as with $\alpha < 0, \beta < 0$. The same asymptotics $\Delta \to -\infty, \Delta_1 \to +\infty$ are valid at the vertical boundary of region D, where we have two solutions for $\alpha > 0, \beta < 0$ and two for $\alpha < 0, \beta > 0$. Finally, at the vertical boundary of region F, we deal with small Δ_1; asymptotically, $\tau \approx (\gamma^2\alpha/\beta)^{1/4}$, and no real roots exist because the signs of α and β are opposite.

We summarize the results in the table. To check these, we observe that the transitions A → B, D → E, E_1, and E, E_1 → F always result in the loss of a pair of roots of the same type, which go into the complex region. The signs of the second derivatives f_{vv} and f_{kk} are also given in our table. Moreover, we indicate the order of disposition of $|\omega|$ for various solutions, from larger to smaller $|\omega|$, which we will need below.

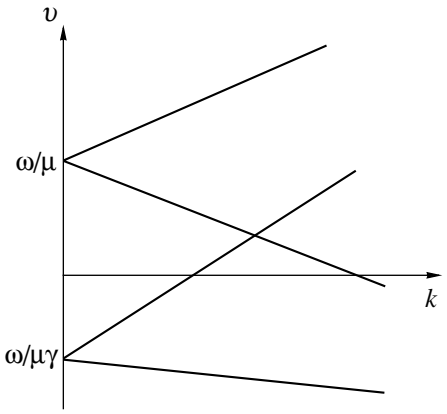

Fig. 2. Asymptotic behavior of the $v(k)$ curves.

We should, however, provide a basis for the applicability of continuity reasons in this context. First, let us check that $f_{vv} = 0$ only at the boundaries of some regions. Direct differentiation yields

$$\frac{\partial^2 f}{\partial v^2} = 2\mu^2[4\gamma\sqrt{XY} + Y - \alpha + \gamma^2(X - \beta)],$$

and, after substituting X, Y, and $\sqrt{Y/X} = -\tau^2/\gamma$, we obtain

$$\frac{\partial^2 f}{\partial v^2} = -\frac{4\beta\tau^3 + 3\sqrt{\Delta_1}\tau^2 - \gamma^2\sqrt{\Delta_1}}{\tau}; \qquad (36)$$

at the point where this quantity vanishes, either a multiple root of (30) appears or τ becomes 0 or ∞.

Thus, once the sign of $\partial^2 f/\partial v^2$ for the corresponding solutions is determined in each of the regions we have isolated, it will not change within the region. We have already proved that the f_{kk} cannot vanish.

Let us note that the sign of ω is not important: according to (17), a change in the sign of ω is simply accompanied by a change in the sign of v so that a completely symmetric transformation takes place. In the special case of $\omega = 0$, Eq. (25) becomes $\gamma^2(\mu v)^4 - (\alpha + \beta\gamma^2)(\mu v)^2 + \alpha\beta - \Delta_1 = 0$, and a double root for v is possible only at $\Delta = 0$. Another particular feature that could arise in our comparson of ω values below is the coincidence of these values for the same combination of parameters. Then, the two transformations under study should correspond to two different minima of $f(v)$ with $f(v) = 0$, and the fourth-power polynomial $f(v)$ should reduce to the square of a second-power polynomial, or, more strictly, to

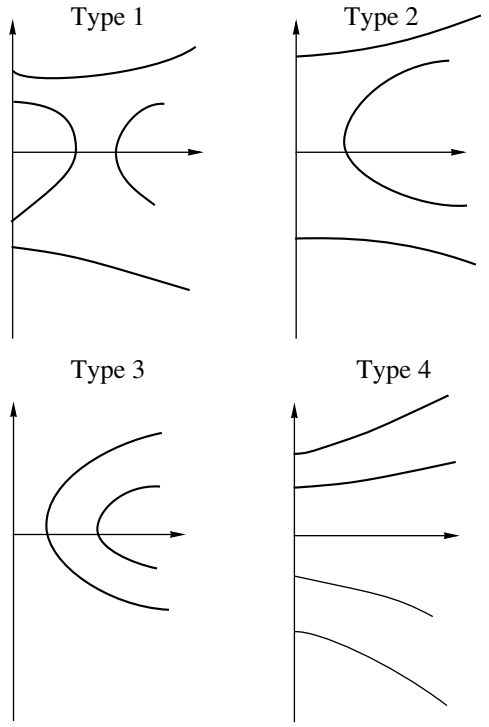

Fig. 3. Various types of behavior of the $v(k)$ curves apart from transformations. The horizontal and vertical axes plot k and v.

$f(v) = (\sqrt{XY} - u)^2$ with $u = \text{const}$. A comparison of coefficients of different powers of v in this case yields $u = \beta\gamma, \alpha = \beta\gamma^2, \tilde{\gamma} = 1$, and the values of X and Y at the points of minima satisfy the conditions $XY = \alpha\beta, \alpha X + \beta Y = 2\alpha\beta - \Delta_1$. Real X, Y satisfy these equations only for $\alpha < 0, \beta < 0$, which corresponds to region A (since ω cannot be multivalued in region B).

We now consider again the specified regions to determine the relative disposition of the values of $|\omega|$. We will simultaneously note the signs of $\partial^2 f/\partial v^2$.

(a) Limiting transition $\gamma \to 0$. As we know, at $\tau = \tau_1$, asymptotically, $\mu\gamma v - \omega = \sqrt{Y} \approx \sqrt{\Delta/\beta}$ and $\mu v - \omega = \sqrt{X} \approx -\gamma\sqrt{Y}/\tau^2 \approx (-\gamma\beta^2/\Delta_1)\sqrt{\Delta/\beta}$. Since γ is small, $\omega_1 \approx -\sqrt{\Delta/\beta}$. If, however, $\tau = \tau_2$, then $\mu v\gamma - \omega = \sqrt{Y} \approx \sqrt{\alpha}$, $\mu v - \omega \approx -\gamma\sqrt{\alpha}/\tau^2 \approx -\Delta_1/(\gamma\sqrt{\alpha})^{1/3}$, and $\omega_2 \approx -\sqrt{\alpha}$. In the cases where the two solutions coexist (regions C, E), we have $\sqrt{\alpha} > \sqrt{\Delta/\beta}, |\omega_2| < |\omega_1|$.

Further, at $\tau = \tau_1$, it follows from (36) that $\partial^2 f/\partial v^2 \approx -\Delta_1/\beta$ (< 0 in region C and > 0 in regions B and E). If, however, $\tau = \tau_2$, then

$$\frac{\partial^2 f}{\partial v^2} \approx -3\sqrt{\Delta_1}\left(\frac{\gamma^2\alpha}{\sqrt{\Delta_1}}\right)^{1/3} < 0$$

(for all three regions).

(b) The transition $\gamma \to \infty$ is needed in region E_1, but the situation is completely symmetric with respect to region E.

(c) For large $|\Delta|$, at $\tau = \tau_1$, we have $\mu\gamma v - \omega = \sqrt{Y} \approx \sqrt{\Delta/\beta}, \mu v - \omega \approx -\gamma\sqrt{\beta^3\Delta}/\Delta_1, (\gamma - 1)\omega_1 \approx \sqrt{\Delta/\beta}$. At $\tau = \tau_{2,3} \approx \pm\gamma$, we obtain $\sqrt{X} \approx -\sqrt{Y}/\gamma$, $(\gamma - 1)\omega_{2,3} \approx 2\sqrt{Y} \approx 2|\gamma|^{1/2}\Delta_1^{1/4}$. Finally, at $\tau = \tau_4$, we have $\mu v - \omega = \sqrt{X} \approx \sqrt{\Delta/\alpha}$, $\mu\gamma v - \omega = \sqrt{Y} \approx -(\tau^2/\gamma)\sqrt{X} \approx -\sqrt{\Delta\alpha^3}/(\gamma\Delta_1)$, $(\gamma - 1)\omega_4 \approx \gamma\sqrt{\Delta}/\alpha$.

Comparing the values of ω for all four roots yields $|\omega_{1,4}| > |\omega_{2,3}|$. The relative order of ω_1 and ω_4 is not specified, and these quantities may even coincide in some cases. However, since they coexist only at $\alpha < 0, \beta < 0$ (region A), no contradiction arises. Apart from the asymptotics $|\Delta| \to \infty$, there is no real need to discriminate between the corresponding ω_1 and ω_4, since the signs of the corresponding second derivatives also coincide pairwise (see below). We recall that coexistence is impossible for $\tau = \tau_2$ and $\tau = \tau_3$; only one solutions operates, depending on the sign of γ.

It follows from (36) that $\partial^2 f/\partial v^2 \approx -\Delta_1/\beta$ at $\tau = \tau_1$, $\partial^2 f/\partial v^2 \approx -2Y < 0$ at $\tau = \tau_{2,3}$, and $\partial^2 f/\partial v^2 \approx -\gamma^2\Delta_1/\alpha$ at $\tau = \tau_4$.

Let us consider the derivative with respect to k:

$$\left(\frac{\partial^2 f}{\partial k^2}\right)_{k=0} = -2\left(\bar{c}^2 - \frac{\pi G\bar{\sigma}}{\mu}\right)X \qquad (37)$$
$$-2\left(c^2 - \frac{\pi G\sigma}{\mu}\right)Y + 4c^2\bar{c}^2\mu^2 - 6\pi G(c^2\bar{\sigma} + \bar{c}^2\sigma)\mu.$$

If $\alpha < 0, \beta < 0$, we subtract the zero-valued expression (17) with coefficient $2\mu^2$ from the right-hand side of (37) to obtain

$$\left(\frac{\partial^2 f}{\partial k^2}\right)_{k=0} = -\frac{2XY}{\mu}$$
$$-\frac{2\pi G(\bar{\sigma}X + \sigma Y)}{\mu}c^2\alpha + \bar{c}^2\beta < 0.$$

If $\alpha < 0$, $\beta > 0$, then, using the representation (25), we obtain

$$X = \beta + \frac{\Delta_1}{Y - \alpha} > \beta \qquad (38)$$

and then, dividing (17) by μ^2 and subtracting the result from (37), we find that

$$\left(\frac{\partial^2 f}{\partial k^2}\right)_{k=0} = \frac{XY}{\mu} - \bar{c}^2X - c^2Y + 3c^2\bar{c}^2\mu^2$$
$$-4\pi G(c^2\bar{\sigma} + \bar{c}^2\sigma).$$

In view of (38),

$$-\frac{XY}{\mu} - c^2Y + 2c^2\alpha - 2\pi G\bar{c}^2\sigma\mu < 0,$$

so that, again, $\partial^2 f/\partial k^2 < 0$. The same result corresponds to $\alpha < 0, \beta < 0$. The question of the sign of the second derivative remains open only for $\alpha > 0, \beta > 0$.

For the solution common to regions A, B, and C (note that nothing special occurs as a boundary is intersected), it is convenient to consider the limiting case $\alpha \to 0$, $\beta \to 0$ at the left edge of region A. Then, as we saw, $Y \to |\gamma|\sqrt{\Delta_1}, X \to \sqrt{\Delta_1}/|\gamma|$. In this limit, substituting the σ and $\bar{\sigma}$ corresponding to $\alpha = \beta = 0$ into (37) yields

$$\frac{\partial^2 f}{\partial k^2} = -\bar{c}^2X - c^2Y + c^2\bar{c}^2\mu^2 \le -2c\bar{c}\sqrt{XY}$$
$$+ c^2\bar{c}^2\mu^2 = 2c\bar{c}\sqrt{\Delta_1} + c^2\bar{c}^2\mu^2 = -c^2\bar{c}^2\mu^2 < 0,$$

and the requirement of continuity implies that this last inequality is valid everywhere. There remains a smaller solution for ω in region C, which vanishes at the boundary $\Delta = 0$; there, $X = Y = 0, \partial^2 f/\partial k^2 = -c^2\bar{c}^2\mu^2 > 0$. This completes the filling of the table.

7. TOPOLOGY OF THE $v(k)$ CURVES

Let us now consider the topology of the dependences $v(k)$ as a whole. Again, we can use the property of continuity starting from large ω, with other parameters being fixed. Transformations with $k = 0$ will then be encountered at certain discrete values of ω, while the behavior of the functions $v(k)$ with $k \neq 0$ can, by and large, be logically inferred from the situation near $k = 0$. Having in mind searches for instabilities, we restrict our analysis to the case $\gamma < 0$; otherwise, as we saw, all perturbations drift away and disappear.

Thus, we consider large $\omega > 0$. If, for the moment, we consider k to be constant, then, in view of (25), we obtain the following asymptotic expansion at any point on the k axis:

$$v_{1,2} = \frac{\omega}{\mu} \pm \frac{1}{\mu}\left[\sqrt{\beta} + \frac{2\pi G^2\sigma\bar{\sigma}q}{(\gamma-1)^2\omega^2\sqrt{\beta}}\right] + o(\omega^{-2}),$$

$$v_{3,4} = \frac{\omega}{\mu\gamma} \pm \frac{1}{\mu\gamma}\left[\sqrt{alpha} + \frac{2\pi G^2\sigma\bar{\sigma}q}{(\gamma-1)^2\omega^2\sqrt{\alpha}}\right] + o(\omega^{-2}).$$

At $k = 0$, the first pair of roots is real if $\beta(0) > 0$, and the second pair is real if $\alpha(0) > 0$; otherwise, they are complex. However, the complex roots also become real as k is increased, and, quite similarly, the solutions for large k can approximately be determined from the relation $X - \beta = 0$ or $Y - \alpha = 0$, except for the case where different branches intersect. If not only ω but also k is large, then, asymptotically, we have

$$v_{1,2} \approx \frac{\omega \pm kc}{\mu}, \quad v_{3,4} \approx \frac{\omega \pm k\bar{c}}{\mu\gamma}. \qquad (39)$$

The two inner asymptotes necessarily intersect at

$$\frac{\omega - kc}{\mu} = \frac{\omega - k\bar{c}}{\mu\gamma}, \qquad k^* = \frac{\omega(1-\gamma)}{\bar{c} - \gamma c}.$$

Near this critical value $k = k^*$, the asymptotic for $v(k)$ is somewhat disrupted. At some distance from the critical point, $X - \beta$ and $Y - \alpha$ behave like $\sim k^2$, and the correction of order $\sim k^2$ in the equations can be considered relatively small. Near the asymptote intersection point, $f(v) < 0$, as in the regions above and below it; therefore, the roots for v near the above critical k temporarily disappear, going into the complex region. Thus, near $k = k^*$, the connectedness of the curves $v(k)$ is disrupted within a short interval: two inner curves merge on both sides of the gap. Generally, the outer asymptote also intersects the inner one, but considerations similar to those presented above indicate that the connectedness of the curves $v(k)$ is not disrupted near the intersection point.

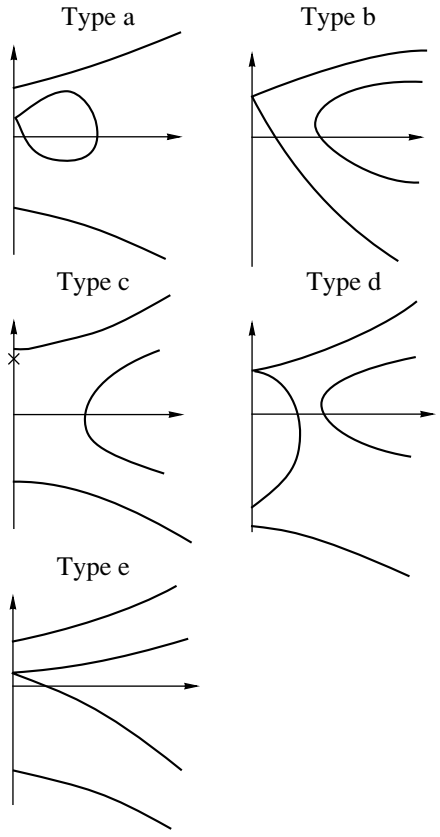

Fig. 4. Various types of transformations. The horizontal and vertical axes plot k and v. In Type b, an isolated singular point on the v axis is indicated.

Now let us move toward smaller $|\omega|$, keeping the remaining parameters fixed. As we saw above, the type of connectedness of the $v(k)$ curves changes in this case only as a result of transformations at $k = 0$, which are possible at certain discrete values of $|\omega|$. (We do not include inflections of the curves of $v(k)$, which can appear and disappear at $k \neq 0$, in the concept of connectedness type.) We can immediately list various possible types of connectedness. We also note transitional types corresponding to various transformations. In each case, we plot only half the diagram, since the region for $k < 0$ can simply be obtained by mirror reflection from the region plotted for $k > 0$. In contrast, the plots are not symmetric with respect to the horizontal axis (and are presented arbitrarily, in this sense), except for the case of $\omega = 0$, which will be discussed below.

Thus, we consider consecutively all regions of variation of α, β, and Δ.

Region A, $\alpha > 0$, $\beta > 0$. As proven above, at large ω, as generally in the case of $\alpha > 0$ and $\beta > 0$, we will have topological Type 1 (see Fig. 3), with four branches at small k and one discontinuity. The transformation (there is only one; see table) produces a momentary maximum in f simultaneously in v and k, at $k = 0$. This is possible only if the inner region $f > 0$ shrinks to a point, as with Type c in Fig. 4. Conversely, an additional maximum could not appear, since the equation $f(v) = 0$ would acquire six roots in this case. After the transformation, the singular point disappears, and we arrive at Type 2 (Fig. 3).

Region A, $\alpha < 0$, $\beta < 0$. At large ω, no solutions for v exist near $k = 0$; i.e., we are dealing with Type 3 (Fig. 3), although it exhibits waviness at finite k. The first transformation produces a zero minimum for f and should follow Type b (Fig. 4). After this, the intersecting branches will diverge, leading to Type 2 (Fig. 3). The second transformation can be related to either the same minimum again reaching the level $f = 0$ or the appearance of another, nearby, zero minimum. The first case, however, drops out, since it leads back to Type 3 (Fig. 3), and the last transformation with $f_{vv} < 0$ is impossible under these conditions. Therefore, the remaining possibility is a second transformation of Type d (Fig. 4) with a transition to Type 1 (Fig. 3). Then, the third transformation implies that the inner loop shrinks to a point as in Type c (Fig. 4); after this point disappears, we finally obtain Type 2 (Fig. 3).

Region B, $\alpha > 0$, $\beta > 0$. This case is similar in all respects to its counterpart for region A.

Region A, $\alpha < 0$, $\beta < 0$. The beginning is the same as for A: the transitions Types 3–b–2 (Figs 3, 4) occur, but the subsequent transformations do not.

Region C, $\alpha > 0$, $\beta > 0$. We start again with Type 1 (Fig. 3). The first transformation leads to the vanishing of the f maximum; for this reason, the inner loop disappears. This is a Type-c transformation (Fig. 4), which leads to topological Type 2 (Fig. 3). The next transformation is again related to the formation of a zero maximum of f; however, the branches are oriented crosswise. This is a Type-e transformation (Fig. 4). Finally, the two branches should diverge, and Type 4 (Fig. 3) is realized.

Region D, $\alpha > 0$, $\beta < 0$. We start with Type 2 (Fig. 3), with two branches of $v(k)$ at small k. The first transformation is related to the zero minimum; this, however, cannot mean the loop touches the v axis, which would simply result in the formation of four independent branches of $v(k)$, since no space for an isolated point with $f_{vv} < 0$ and $f_{kk} < 0$ would remain between these branches after the next transformation. We must assume that the first transformation produces an outer zero minimum, as in Type d (Fig. 4), after which we arrive at Type 1 (Fig. 3). The second transformation removes the inner loop, as in Type c (Fig. 4), and, finally, topological Type 2 arises (Fig. 3).

Region A, $\alpha < 0$, $\beta > 0$, region E, $\alpha > 0$, $\beta < 0$, and region E_1, $\alpha < 0$, $\beta > 0$. Topologically, they coincide with the case of $\alpha > 0$ and $\beta < 0$ for region D.

Region E, $\alpha < 0$, $\beta > 0$, region E_1, $\alpha > 0$, $\beta < 0$, and region F. Type 2 (Fig. 3) persists without any transformations.

Formally, the case of $\omega = 0$ appears as the final result of all of the transformation processes. This case, however, can be directly examined (we already dealt with the corresponding biquadratic form in v), providing a trustworthy test for all our preceding reasoning: at $\omega = 0$, we obtain Type 4 in region C and Type 2 in all other cases (Figs. 3, 4).

8. INFERENCES ON STABILITY

Knowledge of the topology of the $v(k)$ curves enables us to identify cases leading to instability in the system. First and foremost, a single $v(k)$ branch that goes to infinity but does not encounter a transformation point clearly cannot produce an instability. Indeed, due to the symmetry that is present, each half of such a branch corresponds to one of the asymptotic formulas (11) and (11*), while we have seen that the evolution of a perturbation is accompanied by motion along the k axis in a single direction. Thus, a perturbation that corresponds to such a single $v(k)$ branch should be continuously renewed if $k \to \infty$ and go to $k \to -\infty$, or vice versa. Obviously, this situation does not arise autonomously and requires an external intervention. We obtain the same result if

both halves of the $v(k)$ branch are turned in the same direction, as in Type 3 (Fig. 3). On the other hand, in topological Type 1 in the same graph, the $v(k)$ curve can be closed. The corresponding perturbation should continuously circulate from smaller to larger k and backward; however, this does not provide a basis for instability, since an instability cannot arise against the background of a single mode in a conservative system (the interaction of two or more modes is necessary).

Let us now turn to the cases with transformations. At the transformation point, the quasi-classical approximation fails, and a somewhat more accurate consideration is required. Let us take the perturbation of the potential $\hat{\Phi}$ as the dependent variable and choose the normalizing argument $w = k/\sqrt{\nu}$ instead of k, assuming $\nu > 0$ without loss in generality. In addition to the parameters already known, a new one appears, $h = \omega'/\nu$, where ω' is the excess of the actual ω over the value ω_0 corresponding to a transformation. Rearrangements that omit higher-order terms in ν lead to a Schrödinger equation, in essentially the same way as in numerous calculations for normal density waves (see, e.g., [17] and references therein):

$$\frac{d^2\varphi}{dw^2} - (H + \rho^2 w^2)\varphi = 0, \qquad (40)$$

where

$$\varphi(w) = e^{-iv_0 w/\sqrt{\nu}}\delta\hat{\Phi}, \rho^2 = \frac{\partial^2 f}{\partial k^2}\left(\frac{\partial^2 f}{\partial v^2}\right)^{-1},$$

$$H = 2h\frac{\partial f}{\partial \omega}\left(\frac{\partial^2 f}{\partial v^2}\right)^{-1} (k = 0).$$

Here, the coincidence of the signs of f_{kk} and f_{vv} is implied so that we are considering a Type-c transformation (Fig. 4). Formally, (40) is the Schrödinger equation for a linear oscillator. If the perturbation is concentrated near $k = 0$, then, as this point recedes, the amplitude φ varies as $\exp(-w^2/2\lambda)$; i.e., it decreases fairly rapidly, and a physically meaningful solution exists only for some discrete set of real values of the parameter H and, accordingly, ω'. We obtain a discrete spectrum of stable perturbations localized near $k = 0$.

It remains to consider the case of opposite signs of f_{kk} and f_{vv}. Let

$$\rho_1^2 = -\frac{\partial^2 f}{\partial k^2}\left(\frac{\partial^2 f}{\partial v^2}\right)^{-1},$$

and, therefore,

$$\frac{d^2\varphi}{dw^2} + (\rho_1^2 w^2 - H)\varphi = 0. \qquad (41)$$

A Schrödinger equation with the form (41) appears in quantum mechanics in the problem of the reflection of a particle from a potential barrier. In Type-b or Type-e transformations (Fig. 4), perturbations in either both left or both right branches will formally come from an external source and should be absent in an autonomous system. If, however, the solution of (41) vanishes on one side, it vanishes completely so that no autonomous perturbations exist.

When considering Type a (Fig. 4), we assume that the perturbation decays exponentially beyond the loop (the autonomy condition). We multiply (41) in the standard manner by the conjugate function φ^* and the conjugate equation by φ, subtract the two resulting equations termwise, and integrate over the entire interval of w corresponding to the loop. In this way, we obtain

$$(H^* - H)\int |\varphi|^2\, dw = 0,$$

which means that the actual ω is real. The perturbation spectrum consists of stable discrete modes with closely distributed frequencies ω, as is always the case in similar quasi-classical problems. It remains to consider Type d (Fig. 4). In this case, there should be no perturbation on one of the branches that go to infinity. Formally, this resembles the quantum-mechanics problem of the passage of a particle through a barrier: in that case, as well, there is no transmitted wave behind the barrier. For definiteness, we can suppose that

$$|\gamma|c > \bar{c}; \qquad (42)$$

i.e., the first medium plays the leading role; otherwise, we would simply permute the numbering of the media. If so, the outer branches correspond to the first of formulas (39). Since $\nu > 0$, the perturbation of the first medium shifts to the left along the k axis and does not reach the right infinite branch (Fig. 4). We apply cross multiplication and subtraction in the same manner as for Type a to obtain

$$(H^* - H)\int_{-\hat{w}}^{\infty} |\varphi|^2\, dw = \left(\varphi^*\frac{d\varphi}{dv} - \varphi\frac{d\varphi^*}{dv}\right)_{w=\hat{w}}, \qquad (43)$$

where the point $-\hat{w}$ is taken on the left infinite branch, within the region where the asymptotics (10) are valid, viz.,

$$\varphi \sim \exp\left(\frac{-ik^2 c}{2\mu\nu}\right) = \exp\left(-\frac{ic}{2\mu}w^2\right) (w < 0)$$

(qualitatively, the factor preceding the exponent is unimportant). Then, it follows from formula (43) that

$\mathrm{Im}\, H < 0$. In this case, $\partial^2 f/\partial v^2 > 0$. As for $\partial f/\partial\omega$, a somewhat lengthy checking procedure based on the formula

$$\frac{\partial f}{\partial \omega} = -2[(Y-\alpha)\sqrt{X} + (X-\beta)\sqrt{Y}] = \frac{(\gamma-1)\sqrt{\Delta_1 Y}}{\tau}$$

(with $\partial f/\partial\omega$ not vanishing within the regions) yields in the cases of interest: $\omega(\partial f/\partial\omega) < 0$; i.e., $\partial f/\partial\omega < 0$ for $\omega > 0, \mathrm{Im}\, h > 0, \lambda > 0$, and a Type-d transformation ensures the fulfillment of the necessary condition for stability. This is typical of region A with $\alpha < 0, \beta < 0$ and is always the case for regions D, E, and E_1.

9. CONCLUSION

We have considered a somewhat artificial model of a self-gravitating medium, which can nevertheless be used as a representative example of a system with sheared motion. The stability of such systems is a very important question in both astrophysical and geophysical contexts, as well as in the physics of laboratory plasmas. It is important that a uniform, unidirectional shear quenches all perturbations, just as a combination of two uniformly sheared subsystems does, even if they have different coefficients ν. Instability can be manifest only if the shear directions differ. (Specifically, our model implies the interpenetration of two subsystems, or, more precisely, contact between them in a third dimension; however, a similar instability mechanism can operate if the differently sheared domains are spatially separated in y, but a gravitational or some other long-range interaction is present).

In fact, by analyzing the behavior of the system at some critical, "transforming" values of the frequency ω, we can only find the stability threshold, where the instability first sets in. The development of the instability at high growth rates is a separate issue.

We conclude that knowledge of the parameters γ, α, and β in (18) is sufficient to make qualitative judgements about the stability of a system. The instability zone encompasses regions D, E, and E_1 in Fig. 1 and, partly, also region A (provided that $\alpha > 0$ and $\beta > 0$). We emphasize that this criterion does not simply coincide with the stability condition for one or both subsystems. In particular, stability is preserved in region F, although one subsystem is unstable (formally expressed by the conditions $\alpha < 0$ and $\beta < 0$). On the other hand, if $\alpha > 0$ and $\beta > 0$, region A is part of the stability region for both subsystems, provided that the shear is removed. We emphasize again that our stability criterion is complex and nonlinear. It would be impossible to obtain this criterion using expansions in ν and $\bar{\nu}$ as small parameters. The techniques developed in this study can be applied to many other related models, although various mathematical difficulties arise in this case. However, when analyzing our model, we ascertained that such difficulties reflect objective reality and must unavoidably be dealt with.

Finally, the very notion of instability is modified to some extent in sheared systems. We already touched upon "true" instabilities that can develop entirely autonomously. However, if even one subsystem were unstable on its own, then, in the presence of a weak shear, an external perturbation would move along the k axis for a long time and substantially grow. It would be carried into the zone of large k, where the Jeans instability is switched off. Such an evolutionary regime closely resembles the operation of various technical amplifiers [18–20]. However, the mathematical treatment of the action of such natural or artificial amplifiers encounters a specific difficulty, since the question of stability cannot be answered in a "yes" or "no" fashion; instead, there is a gradational transition from stability to instability.

REFERENCES

1. R. H. Miller, in *Numerical Experiments on Spiral Structure (CNRS International Colloquium No. 241)*, 1975, p. 43.
2. M. Miyamoto, Publ. Astron. Soc. Jpn. **27**, 431 (1975).
3. A. M. Fridman and V. L. Polyachenko, *Physics of Gravitating Systems* (Nauka, Moscow, 1976; Springer-Verlag, New York, 1984).
4. K. Rohlfs, *Lectures on Density Wave Theory* (Springer-Verlag, Berlin, 1977; Mir, Moscow, 1980).
5. A. G. Morozov, Astron. Zh. **58**, 34 (1981) [Sov. Astron. **25**, 19 (1981)].
6. A. G. Morozov, Astron. Zh. **58**, 734 (1981) [Sov. Astron. **25**, 421 (1981)].
7. Y. Watanabe, S. Inagaki, M. T. Nishida, *et al.*, Publ. Astron. Soc. Jpn. **33**, 541 (1981).
8. J.-L. Tassoul, *Theory of Rotating Stars* (Princeton Univ. Press, Princeton, 1979; Mir, Moscow, 1982).
9. J. Papaloizou, P. L. Palmer, and A. J. Allen, Mon. Not. R. Astron. Soc. **253**, 129 (1991).
10. A. J. Allen, J. Papaloizou, and P. L. Palmer, Mon. Not. R. Astron. Soc. **256**, 695 (1992).
11. J. M. Bardeen, in *Dynamics of Stellar Systems (IAU Symp. 69)*, (Reidel, Dordrecht, 1975), p. 297.
12. S. Chandrasekhar, *Ellipsoidal Figures of Equilibrium* (Yale University Press, New Haven, 1969; Mir, Moscow, 1973).
13. V. A. Antonov and A. S. Baranov, Astron. Zh. **75**, 467 (1998) [Astron. Rep. **42**, 411 (1998)].

14. V. A. Antonov and A. S. Baranov, Astron. Zh. **75**, 668 (1998) [Astron. Rep. **42**, 587 (1998)].
15. A. Toomre, Astrophys. J. **139**, 1217 (1964).
16. V. P. Maslov, *Perturbation Theory and Asymptotic Methods* [in Russian] (Mosk. Gos. Univ., Moscow, 1965).
17. Yu. N. Efremov, V. I. Korchagin, L. S. Marochnik, and A. A. Suchkov, Usp. Fiz. Nauk **157**, 599 (1989).
18. *Principles of Automatic Control,* Ed. by V. S. Pugachev [in Russian] (Fizmatgiz, Moscow, 1963).
19. A. M. Bonch-Bruevich, *Application of Electronic Tubes in Experimental Physics* [in Russian] (Gostekhizdat, Moscow, 1956).
20. A. A. Kharkevich, *Self-Oscillations* [in Russian] (Gostekhizdat, Moscow, 1953).

Translated by A. Getling

Astronomy Reports, Vol. 46, No. 2, 2002, pp. 96–109. Translated from Astronomicheskiĭ Zhurnal, Vol. 79, No. 2, 2002, pp. 112–126.

Thermal Emission of Methanol and Other Molecules at Millimeter Wavelengths

S. V. Kalenskiĭ, V. I. Slysh, and I. E. Val'tts

Astro Space Center, Lebedev Physical Institute, Russian Academy of Sciences, Profsoyuznaya ul. 84/32, Moscow 117810 Russia

Received January 16, 2001

Abstract—The paper reports the results of a survey of Galactic star-forming regions in the methanol lines $8_{-1}-7_0E$ at 229.8 GHz, $3_{-2}-4_{-1}E$ at 230.0 GHz, $0_0-1_{-1}E$ at 108.9 GHz, and a series of J_1-J_0E lines near 165 GHz. In addition to the methanol lines, lines of methyl cyanide (CH_3CN), cyanoacetylene (HC_3N), methyl formate ($HCOOCH_3$), and sulphur dioxide (SO_2) were detected. Analysis of the data indicates that the methanol emission arises in warm (30–50 K) gas. © *2002 MAIK "Nauka/Interperiodica".*

1. INTRODUCTION

The methanol molecule (CH_3OH) is a slightly asymmetric top with hindered internal rotation possessing a multitude of allowed microwave transitions. Radio emission from methanol in the interstellar medium has been actively studied since its detection by Ball *et al.* in 1970 [1]. Narrow, bright maser lines have been detected at many frequencies, often observed against the background of broader thermal features. Methanol masers have been found in hundreds of star-forming regions in our Galaxy and the Large Magellanic Cloud [2]. Thermal methanol sources have been investigated by Gottlieb *et al.* [3], Friberg *et al.* [4], Slysh *et al.* [5], Kalenskiĭ *et al.* [6], and Hatchell *et al.* [7]. These studies have shown that methanol is a widespread molecule and is observed in cool and warm clouds as well as in hot cores. A number of studies (see, for example, [9]) have demonstrated the presence of methanol in the solid phase in grain mantles. The methanol abundance in cool ($T_{\rm kin} \approx 10$ K) and warm ($T_{\rm kin} \approx 20$–50 K) regions is a few times 10^{-9} [4, 6]. In hot regions with temperatures of the order of 100 K and higher, the grain mantles evaporate, increasing the gas-phase methanol abundance to 10^{-7}–10^{-6} [10, 11].

In 1995, we undertook a search for maser and thermal methanol sources in the $8_{-1}-7_0E$ line at 229.75876 GHz (1 mm), $0_0-1_{-1}E$ line at 108.89420 GHz (3 mm), series of J_1-J_0E lines at 2 mm (the frequencies of the $j = 1$, 2, 3, 4, and 5 are, respectively, 165.05019, 165.06114, 165.09931, 165.19053, and 165.36944 GHz, and $3_{-2}-4_{-1}E$ line at 230.02706 GHz (1 mm) using the 30-m IRAM telescope at Pico Veleta (Spain). These observations resulted in the detection of new masers and a large number of thermal sources. The current paper is devoted to the thermal sources; results for the new masers are described by Slysh *et al.* [12].

2. OBSERVATIONS AND RESULTS

The observations were carried out on the 30-m radio telescope of Institut de radioastronomie millimétrique (IRAM), located at Pico Veleta (Spain), on August 29–31, 1995. The source list contained 36 objects in which strong class I and II masers in other methanol lines had been found earlier. The equipment and observation technique are described by Slysh *et al.* [12]. We detected emission in at least one methanol line in 30 sources.

Broad, quasi-thermal lines in the $8_{-1}-7_0E$ transition were detected toward 18 sources. We detected 28 thermal sources in the $0_0-1_{-1}E$ line, among them the galaxy IC 342, which was detected at the sensitivity limit. Only thermal lines were found in the $3_{-2}-4_{-1}E$ and J_1-J_0E transitions. The parameters of the lines detected are given in Table 1[1], and the corresponding spectra are presented in Figs. 1–4.

Table 2 lists upper limits for the line antenna temperature for sources in which emission was not detected in any line. Note that, in half the cases, when the observations were carried out in bad weather, the upper limits are high, about 1 K or greater. Higher sensitivity observations of these objects may yield positive results.

The sizes of four sources derived from observations at 5–10 points are given in Table 3.

[1] Parameters of lines for 345.01+1.79, NGC 6334I(N), M 8E, L 379 IRS3, DR 21 West, and DR 21(OH) are given in [12].

1063-7729/02/4602-0096$22.00

Table 1. Gaussian line parameters

Source	RA (1950) Dec (1950)		$\int T_A^* dV$, K km s^{-1}	$V_{\rm LSR}$, km/s	ΔV, km/s	T_A^*, K
W3(OH)	$02^h23^m16.5^s$	I	8.8(0.4)	−46.18(0.13)	5.85(0.37)	
	61°38′57″	II	3.8(0.4)	−46.12(0.25)	6.09(0.71)	
		III	13.4(0.6); 11.7(0.6); 12.5(0.6); 12.3(0.6); 6.9(0.6)	−45.70(0.01)	5.16(0.10)	
		IV	4.5(0.1)	−46.34(0.05)	4.94(0.13)	
IC 342	03 41 57.5	I	Not observed			
	67 56 40	II	Not observed			
		III	Not observed			
		IV	0.5(0.1)	45.65(4.58)	34.49(8.03)	
Orion KL	05 32 47.0	I	48.8(7.6)*	6.71 (0.41)	5.52(1.05)	
	−05 24 23	II[1]	26.9(6.7)	7.6(0.7)	5.1(1.2)	
		III	29.8(8.5); 29.1(8.6); 34.0(8.5); 40.2(9.1)*;	7.70(0.50)	6.89(0.02)	
		IV	28.2(1.0)	8.00(0.09)	5.08(0.25)	
OMC−2	05 32 59.4	I	11.1(2.3)*	11.30(0.46)	4.50(1.17)	
	−05 11 45	II				< 1.8*
		III				< 0.37
		IV				< 1.7
S231	05 35 51.3	I	2.81(0.74)*	−14.30(0.33)	2.45(0.62)	
	35 44 16	II				< 1.5*
		III				< 0.93*
		IV	2.1(0.2)	−16.54(0.16)	4.61(0.39)	
NGC 6334 F[4]	17 17 32.4	I	21.0(1.3)*	−7.70(0.17)	5.56(0.38)	
	−35 44 04	II	10.5(1.0)*	−8.71(0.27)	5.32(0.55)	
		III	59.2(3.9); 70.9(3.9); 74.2(3.9); 47.5(3.9); 46.4(3.9)*	−8.09(0.10)	5.70(0.14)	
		IV	15.0(0.2)*	−8.28(0.04)	5.01(0.09)	
Sgr B2	17 44 10.7	I	18.2(1.8)	61.17(0.85)	16.76(2.03)	
	−28 22 17	II				< 0.75
		III	20.6(2.0); 31.8(2.1); 34.0(2.1); 35.3(2.1)	62.01(0.29)	14.33(0.37	
		IV	8.4(0.3)	52.98(0.15)	8.72(0.32)	
G0.54−0.85	17 47 04.4	I				< 0.7
	−28 54 01	II				< 0.7
		III[1]	3.0(1.0); 2.5(0.9); 5.3(1.2); < 3.0	16.71(0.32)	3.50(0.54)	
		IV	4.6(0.2)	16.35(0.09)	4.15(0.23)	
G5.90−0.43	17 57 36.9	I	2.3(0.3)	6.25(0.33)	4.83(0.76)	
	−24 04 22	II				< 0.24
		III	3.9(0.6); 5.1(0.6); 4.3(0.6); 3.2(0.5)	6.89(0.25)	6.89(0.41)	
		IV	2.7(0.1)	7.07(0.10)	5.58(0.26)	

Table 1. (Contd.)

Source	RA (1950) Dec (1950)		$\int T_A^* dV$, K km s^{-1}	V_{LSR}, km/s	ΔV, km/s	T_A^*, K
G9.62+0.19	18 03 16.0	I	2.7(0.6)	4.11(0.46)	4.08(1.19)	
	−20 31 53	II				<0.5
		III	5.7(0.6); 5.0(0.6); 6.7(0.7); 5.3(0.7)	3.56(0.21)	6.53(0.32)	
		IV	4.9(0.2)	3.77(0.15)	6.86(0.38)	
W31(1)[5]	18 05 40.0	I	20.8(1.0)	65.93(0.25)	10.87(0.61)	
	−19 52 24	II	9.7(1.1)	66.22(0.47)	8.86(1.27)	
		III	26.7(1.6); 31.4(1.6); 31.6(1.6); 25.2(1.7)	66.29(0.14)	8.23(0.18)	
		IV	13.5(0.2)	66.49(0.06)	7.78(0.15)	
W31C	18 07 31.0	I	5.1(1.0)	−3.81(0.52)	6.48(1.96)	
	−19 56 19	II				<0.5
		III	9.7(0.9); 11.0(1.0); 12.5(1.0); 11.2(1.0)	−3.90(0.21)	8.62(0.32)	
		IV	9.2(0.2)	−3.94(0.09)	7.50(0.21)	
W33 Met	18 11 15.0	I				<0.5
	−17 56 43	II				<0.5
		III[1]	2.5(0.6); 1.3(0.6); 1.9(0.5); 1.3(0.5)	36.90(0.34)	4.04(0.62)	
		IV	2.3(0.2)	36.79(0.11)	3.19(0.34)	
W33 Therm	18 11 19.7	I				<0.45
	−17 56 08	II				<0.45
		III	5.8(0.6); 6.2(0.6); 4.2(0.6); 3.3(0.6)	35.30(0.15)	4.31(0.23)	
		IV[2]	7.0(0.2)	36.01(0.09)	6.61(0.20)	
GGD 27	18 16 13.8	I				<0.24
	−20 48 31	II				<0.24
		III				<0.34
		IV	0.9(0.1)	12.50(0.08)	2.20(0.23)	
G34.26+0.15	18 50 46.2	I	11.8(0.6)	57.90(0.18)	7.06(0.43)	
	01 11 06	II	5.8(0.6)	57.39(0.54)	9.64(1.14)	
		III	10.9(0.8); 13.4(0.9); 14.6(0.9); 16.4(0.9)	58.26(0.12)	6.81(0.17)	
		IV	8.4(0.2)	57.88(0.08)	6.83(0.18)	
G35.19−0.74	15 55 40.8	I	4.7(0.3)	33.82(0.07)	6.17(0.65)	
	01 36 30	II				<0.39
		III	4.3(0.7); 4.6(0.7); 5.3(0.7); 3.5(0.8)	32.65(0.32)	6.82(0.54)	
		IV	2.9(0.2)	33.47(0.17)	5.51(0.46)	
W49N	19 07 48.3	I	1.8(0.4)	8.90(1.23)	11.52(2.90)	
	09 01 18	II				<0.21
		III	1.6(0.4); 3.6(0.5); 2.9(0.5); 1.1(0.4)	6.92(0.57)	10.78(0.65)	
		IV	2.2(0.1)	6.25(0.34)	10.40(0.75)	

Table 1. (Contd.)

Source	RA (1950) Dec (1950)		$\int T_A^* dV$, K km s^{-1}	$V_{\rm LSR}$, km/s	ΔV, km/s	T_A^*, K
W51 E1/E2[6]	19 21 26.2	I	38.8(0.8)	55.69(0.07)	7.62(0.18)	
	14 24 43	II	12.9(0.7)	55.51(0.22)	7.79(0.49)	
		III	36.5(2.2); 45.9(2.2); 46.8(2.2); 47.1(2.2)	56.02(0.12)	8.32(0.17)	
		IV	25.1(0.2)	55.74(0.02)	7.98(0.05)	
W51Met2	19 21 28.5	I				<0.30
	14 23 32	II				<0.30
		III				<0.39
		IV	1.6(0.2)	54.86(0.21)	4.77(0.60)	
Onsala 1	20 08 10.0	I				<1.1*
	31 22 40	II				<1.1*
		III	Not observed			
		IV	2.3(0.3)	11.64(0.31)	5.68(0.78)	
W75N	20 36 50.4	I				<0.70*
	42 27 23	II				<0.70*
		III	Not observed			
		IV	1.5(0.1)	8.45(0.14)	3.29(0.32)	
Cep A	22 54 19.2	I	3.2(0.4)[1]	−7.10(0.56)	7.57(1.00)	
	61 45 47	II	2.3(0.5)[1]	−5.11(0.71)	6.94(1.80)	
		III				<0.37
		IV	0.7(0.1)	−10.04(0.31)	3.43(0.70)	
		IV	0.4(0.1)	−4.85(0.33)	2.61(0.70)	
NGC 7538	23 11 36.6	I	2.1(0.3)	−59.02(0.41)	5.21(0.88)	
	61 11 50	II	1.4(0.3)[1]	−59.26(0.54)	4.89(1.16)	
		III	3.3(0.4); 3.8(0.4); 3.9(0.5); 3.4(0.4)	−58.21(0.15)	4.46(0.23)	
		IV	3.0(0.1)	−57.04(0.08)	5.01(0.19)	

[1]—Detected at the sensitivity limit.

[2]—Probably a blend of several components.

[3]—Parameters of the $J = 5$ line are given for the direction $(0, 10'')$.

[4]—Detected the $19_5{-}20_4A^-$ methanol line with $\int T_A^* dV = 4.6(0.9)$ K km s^{-1}, $V_{\rm LSR} = -6.8(0.5)$ km s^{-1}, $\Delta V = 4.4(0.9)$ km s^{-1}.

[5]—Detected the $19_5{-}20_4A^-$ methanol line with $\int T_A^* dV = 5.2(0.9)$ K km s^{-1}, $V_{\rm LSR} = 65.9(1.1)$ km s^{-1}, $\Delta V = 11.8(1.9)$ km s^{-1} and a blend of the $19_5{-}20_4A^+$ and $^{34}SO_2$ methanol lines with $\int T_A^* dV = 9.3(1.2)$ K km s^{-1}, $V_{\rm LSR} = 70.1(1.1)$ km s^{-1}, $\Delta V = 15.9(2.2)$ km s^{-1}.

[6]—Detected the $19_5{-}20_4A^-$ methanol line with $\int T_A^* dV = 5.3(0.5)$ K km s^{-1}, $V_{\rm LSR} = 56.4(0.4)$ km s^{-1}, $\Delta V = 7.3(0.8)$ km s^{-1} and a blend of the $19_5{-}20_4A^+$ and $^{34}SO_2$ methanol lines $15_{3.13}{-}16_{0.16}$ with $\int T_A^* dV = 8.8(0.7)$ K km s^{-1}, $V_{\rm LSR} = 58.1(0.5)$ km s^{-1}, $\Delta V = 12.4(1.2)$ km s^{-1}.

[7]—The $1_1{-}1_0E$ methanol line is blended with the ($HCOOCH_3$ $36_{9,27}{-}36_{8,28}A$ methyl formate line.

Note: * Transition notation: I—$8_{-1}{-}7_0E$, II—$3_{-2}{-}4_{-1}E$, III—$J_1{-}J_0E$[7], IV—$0_0{-}1_{-1}E$. The last column lists 3σ upper limits for the antenna temperature. Asterisks indicate observations for which the system noise temperature exceeded 3000 K; the calibration is no longer trustworthy when the system temperature is so high.

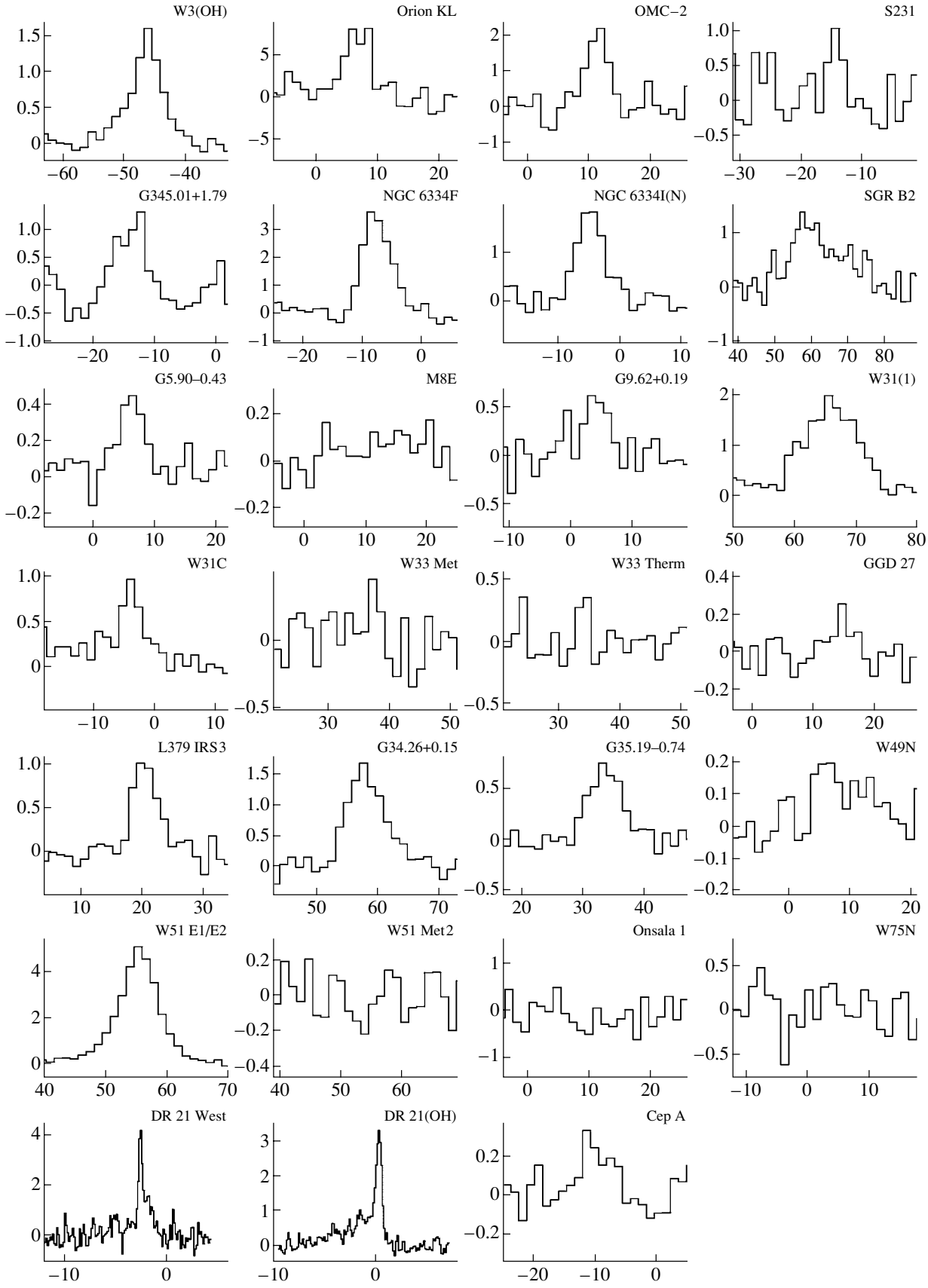

Fig. 1. Spectra of the sources at 229.8 GHz.

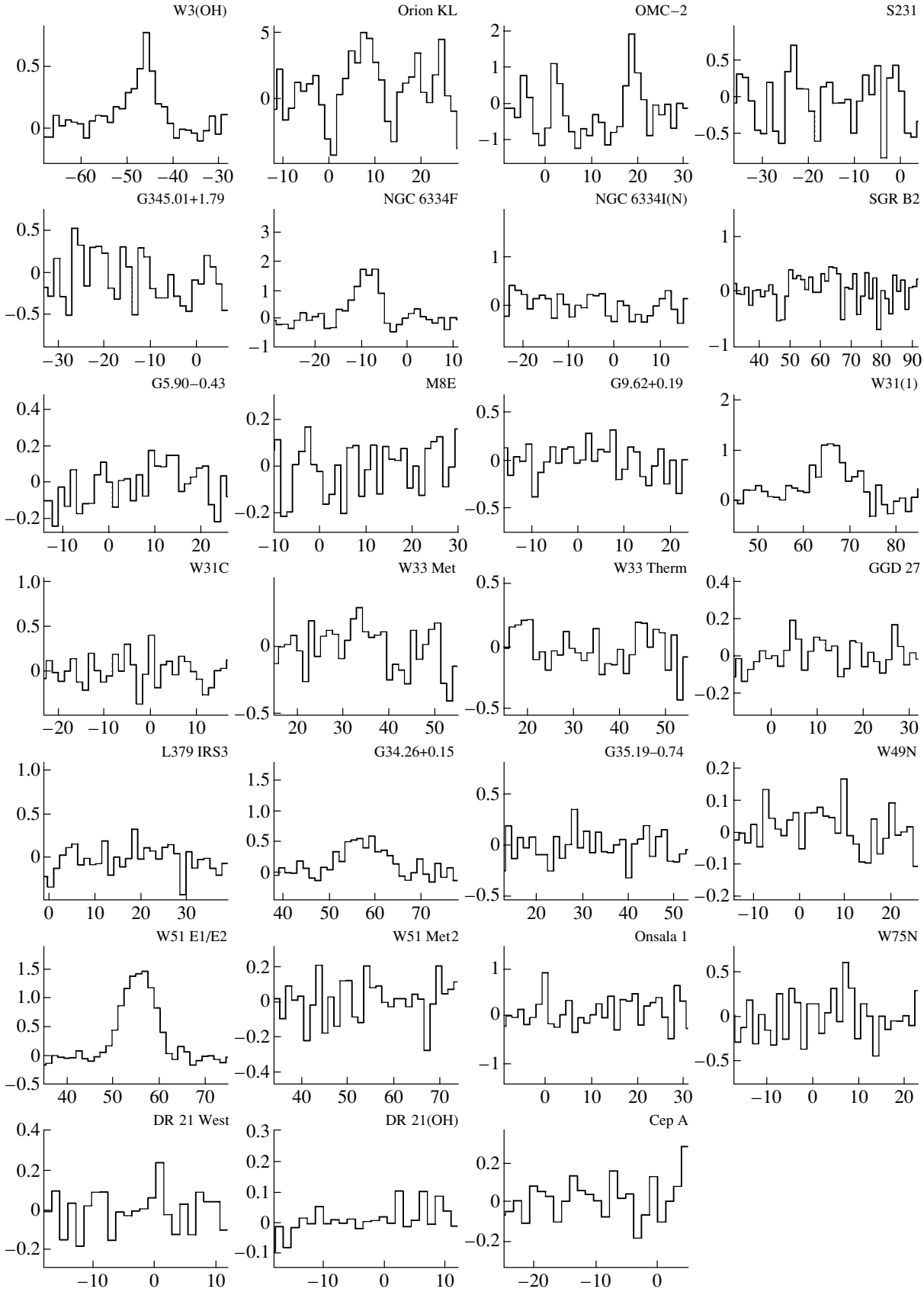

Fig. 2. Spectra of the sources at 230.0 GHz.

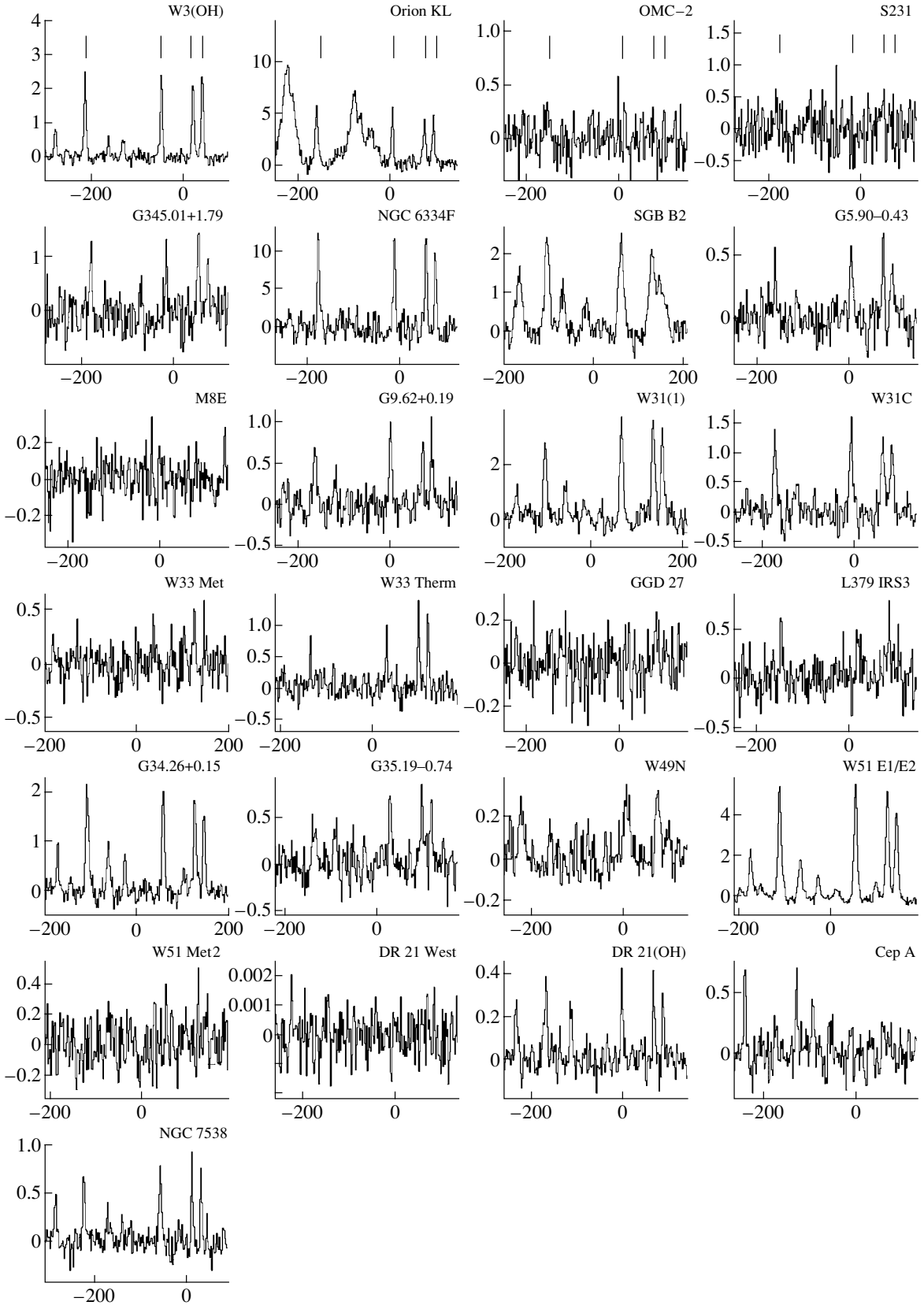

Fig. 3. Spectra of the sources at 165 GHz. The vertical lines in the uppermost row denote the J_1-J_0E, $J = 1-4$ methanol lines. The quantum number J grows from 1 to 4 from left to right. The velocity of the methanol 3_1-3_0E line relative to the local standard of rest is along the X axis.

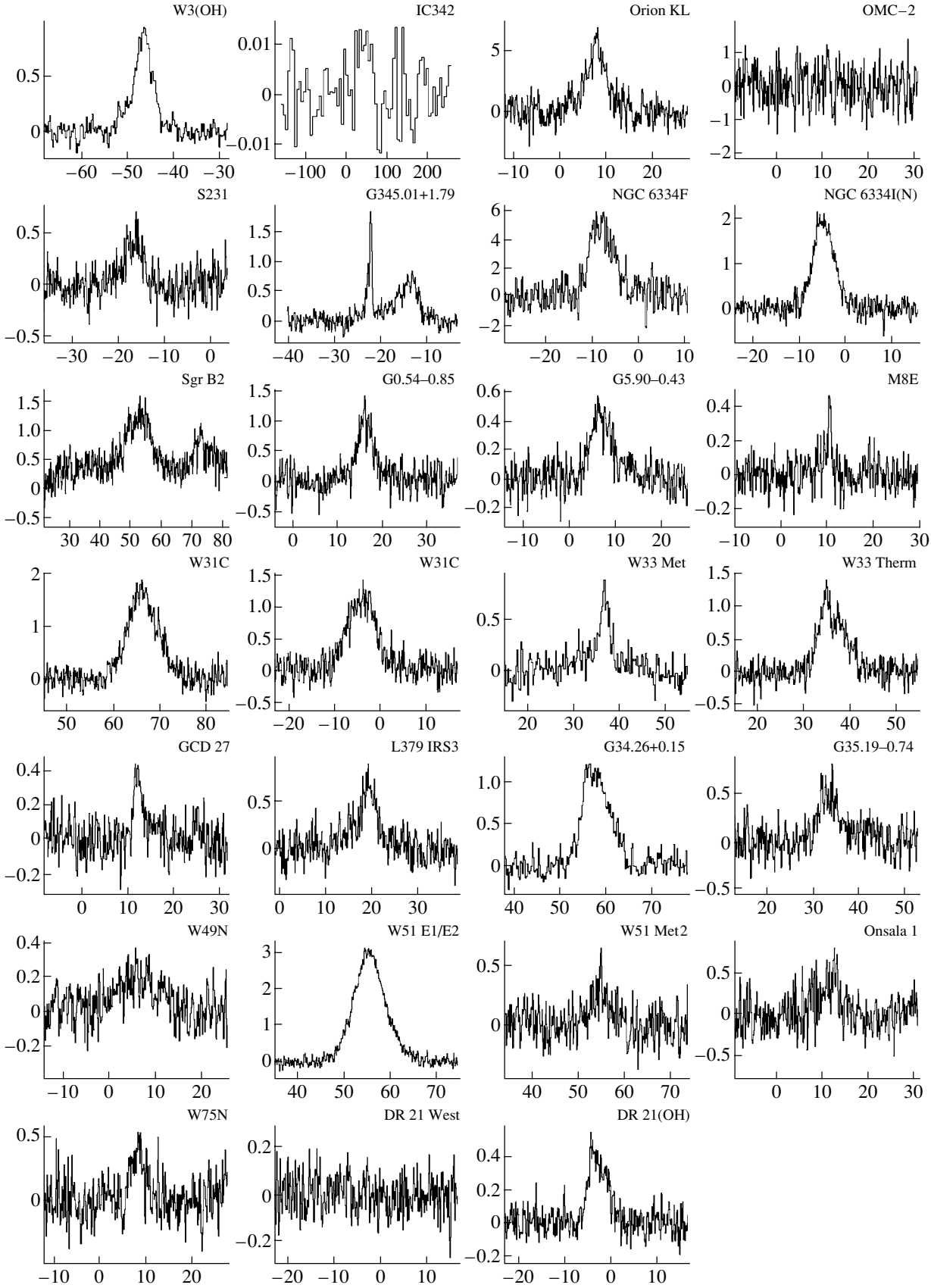

Fig. 4. Spectra of the sources at 108.9 GHz.

Table 2. 3σ upper limits for the antenna temperature for objects toward which no emission was detected.

Source	RA (1950)	Dec (1950)	229.8, 230.0 GHz	165 GHz	108.9 GHz
S235B	05 37 31.8	35 40 18	2.1*	1.8*	1.0
NGC 2071	05 44 30.0	00 20 40	3.9*	2.0*	2.5
S 252	06 05 53.5	21 39 02	2.6*	0.4	1.1
NGC 2264	06 38 24.0	09 32 00	0.5	0.4	1.1
W48	18 59 13.8	01 09 20	0.4	0.5	0.5
G59.78+0.06	19 41 05.6	23 36 51	0.9*	–	0.5
S 140	22 17 41.2	63 03 43	0.3	0.3	0.4

Note: Asterisks indicate observations during which the system noise temperature exceeded higher 3000 K.

Table 3. Source sizes in RA/Dec (arcsec)

Frequency, GHz	W3(OH)		G345.01+1.79		G34.26+0.15		W51 E1/E2	
108.9	38/–	31/–	56/<30	51/<20	40/38	33/31	26/25	15/13
165					$< 25/< 22$	$< 20/< 16$	$< 21/< 24$	$< 15/< 18$
229.8					$< 27/< 27$	$< 25/< 25$	$< 18/< 19$	$< 15/< 16$
230.0					$< 54/< 54$	$< 53/< 53$	$< 21/< 19$	$< 18/< 16$

Note: For each object, the left column gives the size of the source convolved with the beam, and the right column gives the deconvolved size. At 165 GHz, the sizes in the 4_1–4_0E line are given.

In addition to the methanol lines, we also detected and identified lines of HC_3N, SO_2, $HCOOCH_3$, and CH_3CN; some lines could not be identified (Fig. 5, Table 4). The line identification was based on the coincidence of the observed frequencies with those from the JPL catalog (http://www.jpl.nasa.gov/). We simultaneously detected seven 9_K–8_K ($K = 0$–6) CN_3CN lines; therefore, there is no doubt about the identification of lines of this molecule. We verified the identification of other lines as follows. We plotted rotational diagrams based on firmly identified lines, whose intensities were taken from spectral scans of four star-forming regions (a paper by L.E.B Johansson, S.V. Kalenskiĭ, and A.V. Alakoz containing these results is in preparation), and then plotted the points for a line to be analyzed on these diagrams (Fig. 6). The line was considered to be identified if its point appeared within the scatter due to known lines. Our identification results are given in Table 4.

3. DISCUSSION

3.1. Methanol

We detected thermal emission at 108.9 GHz in most of the sources; in many objects, we also found thermal emission at 165, 229.8, and 230.0 GHz. We have estimated the angular dimensions of four sources, which are about 20″–50″ or less (Table 3). The 108.9-GHz emission arises in a transition between levels with $E/k = 0$ and 5.23 K; it can be excited even at the lowest temperatures and densities encountered in molecular clouds (about 5 K and 10^3 cm^{-3}, respectively). Other lines require higher temperatures and densities; however, even in the 8_{-1}–7_0E line, which has an upper level at 81 K, appreciable emission can already arise at a kinetic temperature of about 25 K (see below).

We detected the 19_5–20_4A^+ and 19_5–20_4A^- methanol lines at 229.86419 and 229.93918 GHz, respectively, toward NGC 6334F, W31(1), and W51 E1/E2. These lines, with $E/k \approx 800$ K, can be excited only in very hot and dense gas, for example,

Table 4. Lines of other molecules detected during the survey

Molecule	Transition	Frequency, GHz	Source	$\int T_A^* dV$, K km s^{-1}	$V_{\rm LSR}$, km/s	ΔV, km/s	T_A^*, K
HC_3N	19–18	172849.300	W51 E1/E2	87.0(0.82)	55.89(0.20)	8.92(0.49)	9.15[1]
			Cep A	15.15(0.41)	−11.15(0.28)	4.31(0.71)	3.30[1]
			DR 21(OH)[1]	8.05(0.26)	3.16(0.49)	5.83(0.96)	1.30[1]
			G34.26+0.15	40.65(0.97)	59.91(0.44)	7.67(1.12)	5.00[1]
$HCOOCH_3$	$13_{2,11}$–$12_{2,10}E$	164955.670	W51 E1/E2				
$HCOOCH_3$	$13_{2,11}$–$12_{2,10}A$	164968.621	W51 E1/E2				
$HCOOCH_3$	$14_{7,7}$–$13_{7,6}A^2$	172693.626	W51 E1/E2	26.35(0.80)	55.93(0.87)	10.84(1.57)	2.30[1]
CH_3CN	9_0–8_0	165569.089	NGC 6334F	15.3(1.88)	−7.93(0.16)	5.71(0.22)	2.51
	9_1–8_1	165565.899	NGC 6334F	26.4(1.96)	−7.93(0.16)	5.71(0.22)	4.35
	9_2–8_2	165556.329	NGC 6334F	18.5(1.84)	−7.93(0.16)	5.71(0.22)	3.05
	9_3–8_3	165540.385	NGC 6334F	21.8(1.90)	−7.93(0.16)	5.71(0.22)	3.59
	9_4–8_4	165518.072	NGC 6334F	16.2(1.80)	−7.93(0.16)	5.71(0.22)	2.66
	9_5–8_5	165489.399	NGC 6334F	14.5(2.36)	−7.93(0.16)	10.48(1.87)	1.30
	9_6–8_6	165454.377	NGC 6334F	14.5(2.04)	−7.93(0.16)	7.87(1.20)	1.73
SO_2	$9_{4,6}$–$10_{3,7}$	165123.634	Orion KL	84(5)	8.8(0.25)	30.2(0.33)	2.6
			W51 E1/E2	4.3(0.68)	56.8(0.17)	7.21(0.24)	0.57
			Cep A	1.94(0.56)	−10.4(0.34)	6.30(0.52)	0.29
			DR 21(OH)				< 0.1
			G34.26+0.15				< 0.3
SO_2	$5_{2,4}$–$5_{1,5}$	165144.651	Orion KL	196(5)	8.8(0.25)	30.2(0.33)	6.1
			W51 E1/E2	8.9(0.71)	56.8(0.17)	7.21(0.24)	1.16
			Cep A	3.1(0.57)	−10.4(0.34)	6.30(0.52)	0.69
			DR 21(OH)				< 0.1
			G34.26+0.15	4.82(0.57)	57.6(0.21)	5.0(0.33)	0.91
SO_2	$7_{1,7}$–$6_{0,6}$	165225.452	Orion KL	288(5)	8.8(0.25)	30.2(0.33)	9.0
			W51 E1/E2	14.3(0.75)	56.8(0.17)	7.21(0.24)	1.86
			Cep A	4.64(0.58)	−10.4(0.34)	6.30(0.52)	0.69
			DR 21(OH)	1.81(0.28)	−3.6(0.50)	6.48(0.74)	0.26
			G34.26+0.15	5.07(0.55)	57.6(0.21)	5.0(0.33)	0.96

[1]—Assuming a mirror suppression of 7 dB.

[2]—Blended with the $HCOOCH_3$ $14_{7,8}$–$13_{7,7}$ A and E lines.

in hot cores or under the action of radiation. Like Hatchell *et al.* [7], we assumed that lines with such high level energies are excited in gas that is distinct from the bulk of the gas contributing to the emission in the other lines observed, and we did not take these lines into account in our subsequent analysis.

We detected seven sources in the 3_{-2}–$4_{-1}E$ line at 230.0 GHz. The lifetime of a molecule in the

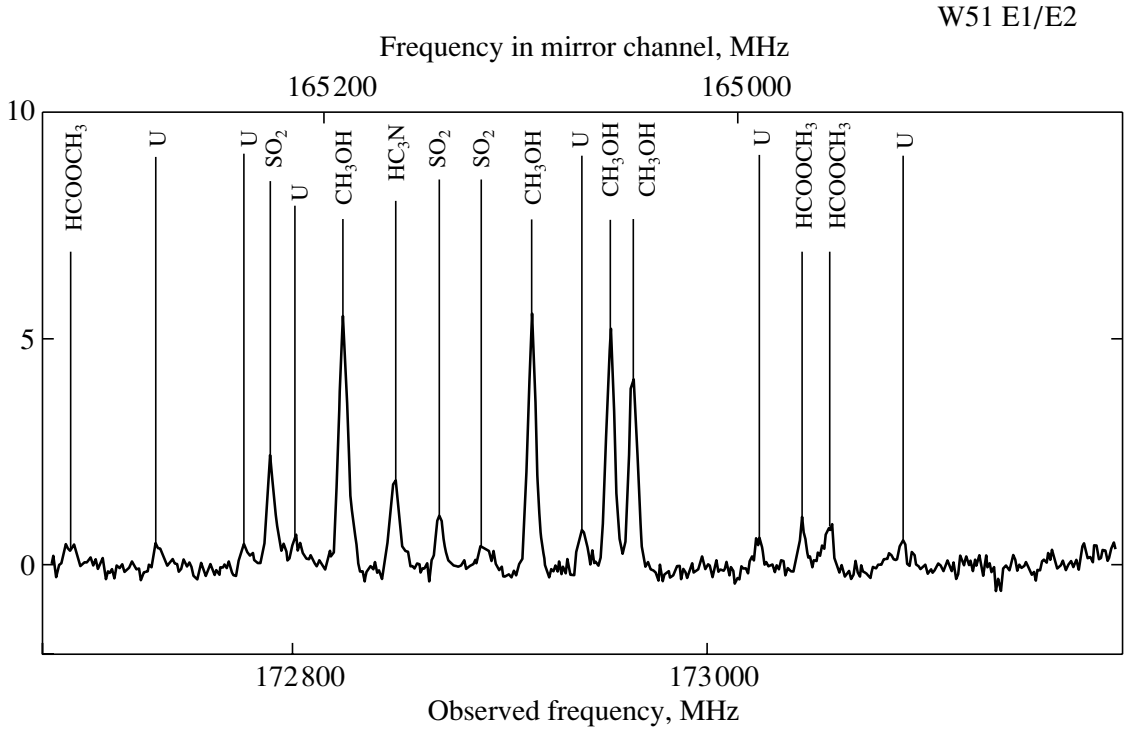

Fig. 5. The 165-GHz spectrum of W51 E1/E2.

upper level $3_{-2}E$ to radiative deactivation is short (about 100 s). Therefore, high densities, of the order 10^7 cm^{-3} and greater, are required for purely collisional excitation of this level. However, the density requirements are considerably eased if the source size and/or methanol abundance are sufficiently great for the methanol rotational lines to be optically thick. Modeling by the method of a large velocity gradient shows that if the optical depth in the 4_1–4_0E line is about unity, the brightness temperature in the 3_{-2}–$4_{-1}E$ line can already be about 1 K at a density of about 3×10^5 cm^{-3}. Thus, the detection of emission in the 3_{-2}–$4_{-1}E$ line testifies to a high gas density and/or large optical depth in the rotational methanol lines.

An important method for the analysis of molecular radio lines is the use of rotational diagrams [13]. Assuming that all level populations for a given molecule are thermalized (the lines used for the analysis are optically thin, with $J(\nu_0, T_{\rm ex}) \gg J(\nu_0, T_{BG})$, where $J(\nu, T)$ is the Rayleigh–Jeans brightness temperature for the specified intensity and frequency), we can obtain the relationship

$$\ln \frac{3kW}{8\pi^3 \nu_0 S\mu^2} = \ln \frac{N}{Q_{\rm rot}} - \frac{E_u}{kT_{\rm rot}}, \qquad (1)$$

where $W = \int T_R\, dV$ is the integrated intensity and $Q_{\rm rot}$ is the rotational statistical sum. The dependence of $3kW/8\pi^3\nu_0 S\mu^2$ on $E_u/kT_{\rm rot}$ is called the rotational diagram. Formula (1) shows that the slope of the approximating straight line is proportional to the temperature, and the point of intersection with the vertical axis depends on the molecular column density.

The ratios of various level populations for methanol in interstellar gas are far from equilibrium [8]. Nevertheless, at gas densities of the order of 10^5 cm^{-3} or higher, the ratios of the populations of levels within the same ladder can be described using a single temperature, which is close to the kinetic temperature [6, 8]. Thus, the kinetic temperature can be derived from rotational diagrams based on the J_1–J_0E lines. We have plotted rotational diagrams for 17 sources using our 165-GHz data (Fig. 6). The points satisfactorily fit the approximating straight lines for only nine sources—NGC 6334I(N), Sgr B2, G5.90–0.43, W31(1), W31C, W33Therm, G35.19–0.74, DR 21 (OH), and NGC 7538. The implied rotational temperatures for these objects are in the range 12–35 K (Table 5). Such temperatures are characteristic of the extended (with sizes of the order of a parsec) warm regions of dense gas detected in the lines of CS, NH_3, CH_3CCH, and other molecules. The scatter of the points on the diagrams for W3(OH), G345.01+1.79, G9.62+0.19, and W49N is large, suggesting that these sources have complex structures. This is confirmed by the different line intensity ratios observed in different directions. The points in the diagrams

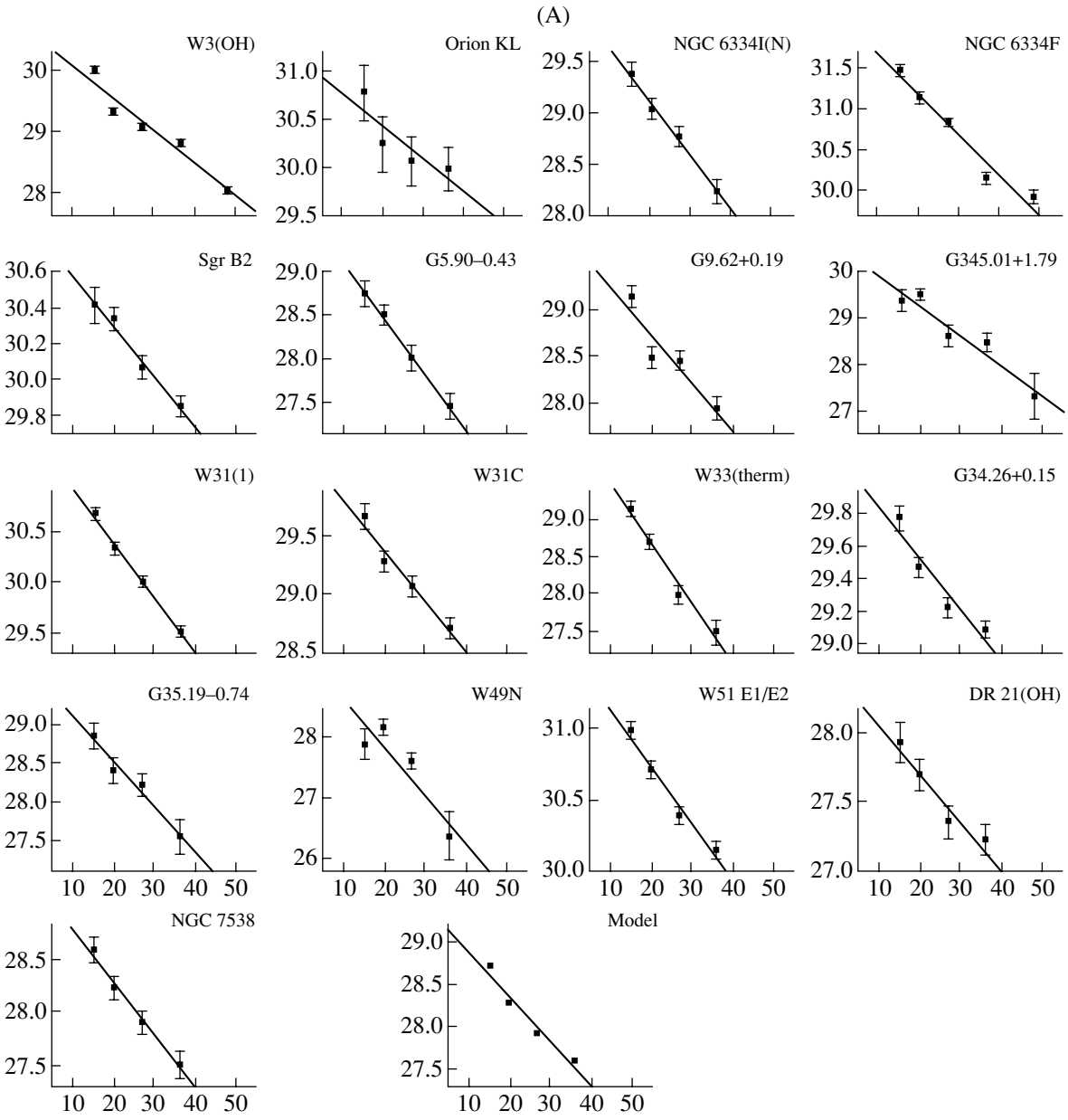

Fig. 6. Rotational diagrams derived from the 166-GHz observations. The horizontal axis plots E/k and the vertical axis $\ln(3kW)/(8\pi^3\nu_0 S\mu^2)$.

for Ori KL, G34.26+0.15, and W51 E1/E2 lie along arches, also possibly indicating the presence of complex structures. In particular, such rotational diagrams should be displayed by objects consisting of hot cores and cooler and/or less dense halos. In such sources, the contribution of the core grows with growing excitation energy of the transitions, resulting in an arch-like arrangement of the points in rotational diagrams. This is quite plausible, since all the three sources contain hot cores [14]. Another possibility is that the $J_1{-}J_0E$ lines are not optically thin. This is illustrated by the model rotational diagram of Fig. 6, which was plotted as follows. Using the large velocity gradient (LVG) method, we calculated the brightness temperature in the $J_1{-}J_0E$ lines for a source with a kinetic temperature of 25 K, density of 10^6 cm^{-3}, and methanol density divided by the velocity gradient of 6.7×10^{-3} cm^{-3}/(km/s pc^{-1}). The $J_1{-}J_0E$ lines are optically thick in this model; the optical depth in the $1_1{-}1_0E$ line is 2.6. The resulting rotational diagram is arch-shaped, like the rotational diagrams for Ori KL, G34.26+0.15, and W51 E1/E2.

We also modeled the methanol source in W51 E1/E2 using the LVG method. We calculated

Table 5. Parameters of the sources determined using rotational diagrams

Source	CH_3OH		CH_3CN		$HCOOCH_3$		SO_2	
	T_{rot}, K	N, 10^{16} cm^{-2}	T_{rot}, K	N, 10^{17} cm^{-2}	T_{rot}, K	N, 10^{15} cm^{-2}	T_{rot}, K	N, 20^{15} cm^{-2}
Orion KL					65	1.3	137	3.0
NGC 6334I(N)	18.8(1.0)	5.4						
NGC 6334F			1110	1.1				
Sgr B2	35.7(2.6)	74						
G5.90-0.43	16.0(0.5)	2.1						
W31(1)	18.5(0.9)	19						
W31C	23.2(2.7)	11						
W33 Therm	12.4(1.1)	1.8						
G35.19-0.74	17.2(1.8)	2.5						
W51 E1/E2					189	2.4	254	2.4
DR 21(OH)	28.8(4.8)	3.3						
NGC 7538	20.1(1.5)	2.7						

the brightness temperature T_{obs} of the lines observed using the data of Table 1, assuming that the source size is the same in all the lines, and is equal to 15″ (Table 3). Further, we calculated a set of models and identified the model minimizing the sum of squared deviations

$$\sum (T_{obs} - T_{mod})^2. \quad (2)$$

This best-fit model has a gas temperature of 25 K, density of 10^7 cm^{-3}, and E-methanol density divided by the velocity gradient of 2×10^{-3} cm^{-3} (km/s pc^{-1}). The relative E-methanol abundance is about 3×10^{-9} cm^{-3}. This simple model does not describe the methanol emission region in W51 with sufficient accuracy, possibly because the region is nonuniform. Nevertheless, the model provides rough estimates of the temperature, density, and methanol abundance, and also demonstrates that warm (30–50 K) regions can yield appreciable emission in the 8_{-1}–7_0E line. The values of the methanol density and abundance we have obtained are consistent with previous estimates (see, for example, [6]) and are probably typical of warm clouds.

3.2. Other Molecules

A number of molecules, including cyanoacetylene (HC_3N), methyl formate ($HCOOCH_3$), methyl cyanide (CH_3CN), and sulphur dioxide (SO_2), were detected toward W51 E1/E2. Some were also detected toward Ori KL, DR 21(OH), Cep A, NGC 6334F, and G43.26+0.15 (Table 4). The rotational diagrams for these molecules are presented in Fig. 6.

We found a very high rotational temperature, $T_{rot} = 1110$ K, for the methyl cyanide detected toward NGC 6334F in the 9_K–8_K line series. This is not surprising, since it is known that strong methyl-cyanide emission arises in hot cores, where the abundance of these molecules is strongly enhanced due to evaporation from grain mantles. However, the points corresponding to $K = 3$ and $K = 6$ in the rotational diagram lie far below the approximating line, indicating high optical depth [15]. This high optical depth in the methyl-cyanide lines leads to overestimation of the rotational temperatures, so that the value 1110 K should be considered an upper limit.

It is known that the methyl-formate emission in Orion arises in the so-called Compact Ridge. Emission of CH_3OH, CH_3OCH_3, and some other molecules is observed in the same area. Various authors (see e.g. [13]) have obtained rotational temperatures for $HCOOCH_3$ in the range 25–90 K. The points corresponding to our detected lines fit the rotational diagram well for $T_{rot} = 65$ K, in agreement with previous results. The points corresponding to the lines detected toward W51 E1/E2 fit the rotational diagram for $T_{rot} = 189$ K, which considerably exceeds the temperature derived from methanol lines. This discrepancy may indicate either that the methanol and methyl-formate emission arises in different regions, or that our analysis methods are not suitable for the emission region in W51 E1/E2. For example, this area may be nonuniform, the $HCOOCH_3$ lines may be optically thick, etc. Since, in Orion, CH_3OH and $HCOOCH_3$ are observed in the same region, the latter hypothesis seems more probable.

The SO_2 lines detected toward Orion KL are broad ($\approx$30 km/s), corresponding to a plateau region. The points for our detected lines fit the rotational diagram well for $T_{\rm rot} = 137$ K, in agreement with previous results (119–138.5 K [13, 16]). In W51 E1/E2, we detected much narrower lines with a rotational temperature of 254 K. Such a high temperature suggests that the emission arises in a hot core.

3.3. IC 342

We detected 108.9-GHz emission from this nearby ($\approx$2 Mpc) Scd galaxy at the sensitivity limit. Earlier, 2_K–1_K methanol lines at 96 GHz [17] and 3_K–2_K lines at 145 GHz [18] were detected in IC 342. The antenna temperature integrated over the 108.9-GHz line profile (0.5 K km s^{-1}) is a factor of four lower than that of the 3_K–2_K lines. The lower intensity at 108.9 GHz is due to the lower strength of this line compared to the 3_K–2_K lines, and also to the fact that a blend of several components is observed at 145 GHz.

4. CONCLUSIONS

Our observations at 1, 2, and 3 mm have yielded detections of both maser and thermal methanol sources. The thermal emission in the 0_0–$1_{-1}E$, J_1–J_0E, 8_{-1}–7_0E, and 3_{-2}–$4_{-1}E$ lines arises in warm (12–35 K) gas; however, a contribution by hot cores cannot be excluded.

In addition to the methanol lines, we have detected lines of methyl cyanide (CH_3CN), cyanoacetylene (HC_3N), methyl formate ($HCOOCH_3$), and sulphur dioxide (SO_2). We derived a very high rotational temperature, $T_{\rm rot} = 1110$ K, for the methyl-cyanide 9_K–8_K line series detected toward NGC 6334F; this may be a consequence of a high optical depth in these lines. The points for the lines detected toward W51 E1/E2 fit their rotational diagram well for $T_{\rm rot} = 189$ K, which considerably exceeds the temperature derived from the methanol lines. This discrepancy may indicate that the analysis methods used are not appropriate for the emission region in W51 E1/E2.

ACKNOWLEDGMENTS

The authors are grateful to Dr. Gabriel Paubert and other colleagues from the Pico Veleta Observatory for their help with the observations. This work was partially supported by the Soros Foundation (grant MND300) and the Russian Foundation for Basic Research (project codes 95-02-05826 and 98-02-16916).

REFERENCES

1. J. A. Ball, C. A. Gottlieb, A. E. Lilley, and H. E. Radford, Astrophys. J. Lett. **162**, L203 (1970).
2. A. J. Beasley, S. P. Ellingsen, M. J. Claussen, and E. Wilcots, Astrophys. J. **459**, 600 (1996).
3. C. A. Gottlieb, J. A. Ball, E. W. Gottlieb, and D. F. Dickinson, Astrophys. J. **227**, 422 (1979).
4. P. Friberg, Å. Hjalmarson, S. C. Madden, and W. M. Irvine, Astron. Astrophys. **195**, 281 (1988).
5. V. I. Slysh, R. Bachiller, I. I. Berulis, *et al.*, Astron. Zh. **71**, 37 (1994) [Astron. Rep. **38**, 29 (1994)].
6. S. V. Kalenskii, A. M. Dzura, R. S. Booth, *et al.*, Astron. Astrophys. **321**, 311 (1997).
7. J. Hatchell, M. A. Thompson, T. J. Millar, and G. H. MacDonald, Astron. Astrophys., Suppl. Ser. **133**, 29 (1988).
8. V. I. Slysh, S. V. Kalenskii, I. E. Val'tts, *et al.*, Astrophys. J., Suppl. Ser. **123**, 515 (1999).
9. L. J. Allamandola, S. A. Sandford, A. G. G. M. Tielens, and T. M. Herbst, Astrophys. J. **399**, 134 (1992).
10. R. Bachiller, S. Liechti, C. M. Walmsley, and F. Colomer, Astron. Astrophys. **295**, P51 (1995).
11. K. M. Menten, C. M. Walmsley, C. Henkel, and T. L. Wilson, Astron. Astrophys. **198**, 267 (1988).
12. V. I. Slysh, S. V. Kalenskiĭ, and I. E. Val'tts, Astron. Zh. **79**, 54 (2002).
13. B. E. Turner, Astrophys. J., Suppl. Ser. **76**, 617 (1991).
14. M. Ohishi, in *Abstract Book for IAU Symposium No. 178 "Molecules in Astrophysics: Probes and Processes," Leiden, 1996,* Ed. E. F. van Dishoeck (Kluwer, Dordrecht, 1996), p. 64.
15. S. V. Kalenskiĭ, V. G. Promislov, A. V. Alakoz, *et al.*, Astron. Zh. **76**, 819 (2000) [Astron. Rep. **44**, 725 (2000)].
16. F. P. Schloerb, P. Friberg, A. Hjalmarson, *et al.*, Astrophys. J. **264**, 161 (1983).
17. C. Henkel, T. Jacq, R. Mauersberger, *et al.*, Astron. Astrophys. **188**, L1 (1987).
18. S. Hüttemeister, R. Mauersberger, and C. Henkel, Astron. Astrophys. **326**, 59 (1997).

Translated by Rudnitskiĭ